THE UNIVERSITY OF CALGARY

Asymmetric Emission Model of the Be/X-Ray Binary EXO 2030+375

by

Nathaniel K. Newlands

A THESIS

SUBMITTED TO THE FACULTY OF GRADUATE STUDIES

IN PARTIAL FULFILLMENT OF THE REQUIREMENTS FOR THE

DEGREE OF MASTER OF SCIENCE

DEPARTMENT OF PHYSICS AND ASTRONOMY

CALGARY, ALBERTA

AUGUST, 1997

Abstract

An asymmetric model of x-ray emission from accreting neutron stars is presented. The theoretical model comprises 16 fitting-parameters specifying the geometry of emission from two regions extending above the neutron star surface. This surface is oriented according to the magnetic field geometry. Emission originates from partial, angular sections of this surface. Results from magnetic radiative transfer calculations are incorporated in the model in order to specify the angle and frequency dependence of the local emission intensity.

Recent pulse profile observations of the x-ray binary EXO 2030+375, obtained with the BATSE and EXOSAT satellites, are highly asymmetric. The asymmetry observed in the profiles varies with the rate at which matter is accreted by the neutron star from the Be companion. The asymmetry in the pulse profiles is explained with the model by partial-filling of matter within the polar emission regions.

Acknowledgements

Through all the stages of my degree; course work, undergraduate teaching and thesis research, there are many people who I wish to thank for their individual contributions.

I would firstly like to thank Dr. Robert Brooks (University of Guelph, Ontario) for introducing me to the field of astrophysics, during an upper- year undergraduate research project on white-dwarf stars. This provided the initial encouragement for me to pursue my interests in modelling systems containing compact stellar matter.

I was very fortunate over the past two years to be able to work with my supervisor, Dr. Denis Leahy, in the area of x-ray binary research. From all our discussions, I have learned a great deal from the sense of conciseness and clarity he shows towards understanding physics, whether in expressing theoretical concepts into mathematics or interpreting the results of observations. I am very grateful for his continuous help in my research and for pointing me many a time in the right directions. It was also very rewarding to have taken several courses in astrophysics under his instruction, in which I was introduced to many of the key concepts in astrophysics. I am also grateful for his financial support throughout the summer months, which has enabled me to dedicate my time continually to completing my research. Thank you also for financing my attendance at the 7th. Canadian Conference on General Relativity and Relativistic Astrophysics, June 5-7th., 1997, Calgary. At this conference, I enjoyed discussing my research with other scientists, and in gaining both new insights and new questions concerning present-day issues in theoretical physics.

Many thanks to Mark Stollberg and Bill Paciesas for providing explanation of their

observations of EXO 2030+375, and for providing their pulse profile data from the BATSE satellite. Thanks also to Andy Norton for suggesting to look for analogies between the physics within magnetic cataclysmic variables and x-ray binaries in modelling observed pulse profiles.

Special thanks to Doug Phillips for providing the VRML (virtual reality modelling) visualization of my model, and for teaching me about the use, and implementation of the VRML programming language.

I am grateful to Dr. Kevin Volk for all his helpful suggestions throughout the computational side of my research; ideas for the selection of numerical routines, numerical error analysis and for his guidance on debugging. I also must thank Dr. R. Sreenivasan, who in the early stages of my work, met with me to discuss the physical aspects of neutron star environments, and who continued to encourage my work.

Many thanks to the other members of my committee, Dr. A.R. Taylor and Dr. J. Gleeson for their encouragement and interest in the progress of my work. Our meetings provided the necessary answers and questions in the development of the theoretical model.

I would also like to acknowledge the external examiner, Dr. T. Ziegler, and internal department member Dr. W.J.F. Wilson, for joining the committee at short notice and for providing helpful comments to improve this work.

My thanks to the Department of Physics and Astronomy at the University of Calgary for their continued teaching assistantship and scholarship support, and for all the encouragement and enthusiasm they express towards their graduate students. I greatly enjoyed my course work, and the many times in which I was involved

in departmental activities. I would like to give special mention to Dr. Louro for our many helpful conversations which continued to improve my teaching skills in undergraduate tutorials and lab sessions.

To all my graduate collegues, Guojin Zhang, Paul Webster, James Weygand, John Rewcastle, and Chris Butenhoff, I would like to express my appreciation for making my time in Calgary a fulfilling one.

I am proud to have met many friends living in this part of Canada. Firstly, my sincere thanks and appreciation to my good friend Pankaj Dhar for his immeasurable moral support and advice on life matters. To my close friend, Carla Sparrow, for her support and companionship. I am grateful for the many times you made sure I was eating and sleeping regularly, for teaching me how to finally iron shirts properly, and for showing me how to cook meals other than spaghetti.

Formost in my life, I would like to sincerely thank my parents, and family, for their everlasting guidance, encouragement, advice and support.

Table of Contents

List of Figures

List of Tables

Chapter 1

Introduction

1.1 X-ray Sources

The first detection of x-ray sources is attibuted to sounding rockets that could reach altitudes of at least 100 km., (Friedmann *et al.*, 1951)[16]. Observations made with photon Geiger counters showed that the sun emitted x-rays. Several years later, a celestial x-ray source, Sco X-1, was detected (Giacconi *et al.*, 1962)[38]. One of the first major discoveries was the identification of the Crab Nebula as an extended x-ray source (Bowyer *et al.*, 1964)[42] and later detection of pulsed emission from a pulsar within it (Fritz *et al.*, 1969)[12]. The *Uhuru* satellite launched in 1970 (Giacconi *et al.*, 1971)[39] was dedicated entirely to celestial x-ray astronomy. Its detector of area 0.084 m^2 contained proportional counters sensitive to 2-20 keV x-rays with a collimation (FWHM) of $1°x10°$. This satellite rotated perpendicular to its field of view with a period of 12 minutes, and was placed in a low equatorial earth orbit in order to minimize the background contribution of particles trapped in the earth's radiation belts. The *Uhuru* catalog contains 339 objects consisting of binary stellar systems, supernova remnants, and galaxy clusters (Forman *et al.*, 1978)[48]. More recently, advancement in x-ray astronomy was made with the European EXOSAT satellite, launched in 1983. This satellite had a collecting area of $\sim$ 0.08 m^2, comparable to that of *Uhuru*, and carried 0.16 m^2 Medium Energy (ME) proportional counters with a relatively small field of view (FWHM of 0.75°). Study of individual

sources were made in the energy range of 1-50 keV. Unlike the *Uhuru* satellite, EXOSAT was placed in a highly eccentric orbit with an orbital period of 90 hrs. This allowed uninterrupted viewing of sources for up to several days. EXOSAT was used extensively for investigation of quasi-periodic oscillations (QPOs). These oscillations were found to be common in low-mass x-ray binaries. For a recent review of x-ray astronomy missions, see (Bradt *et al.*, 1992)[20]. The x-ray binary EXO $2030+375$ which exhibited substantial changes in spin period and pulse shape as a function of luminosity (Parmar *et al.*, 1989)[5][4] was one of EXOSAT's major discoveries. Figure (1.1) shows the distribution of binary x-ray pulsars from a recent survey made by *Ginga* (Tanaka *et al.*, 1992)[46]. This map shows seven newly discovered transient x-ray sources and in particular, the location of EXO $2030+375$ near Cyg X-1, along the galactic plane.

1.2 Be/X-ray Binary Systems

There are $\sim$ 200 x-ray binaries now known in our galaxy. These systems have evolved to contain a collapsed star and a 'normal' stellar companion. Binaries in which the x-ray source is an accreting neutron star can be divided into two distinct categories: high mass x-ray binaries (HMXBs; Cyg X-3, Cen X-3), in which the mass of companion star is $\sim 10M_{\odot}$, and low mass x-ray binaries (LMXBs), having a companion star of mass $\sim 1M_{\odot}$. HMXBs may be further subdivided into two groups according to the time dependence of their x-ray flux. The first grouping consists of stationary or 'persistent' sources, having periods less than $\sim$ 10 days and exhibiting significant fluctuations in x-ray luminosity with continuous x-ray emission.

These systems are close binaries with the companion star (optical component) nearly filling its Roche lobe. The second group of which EXO 2030 + 375 is a member, are nonstationary/transient sources showing pronounced peaks in x-ray luminosity and periods of quiescence during which x-ray emission is below the limit of detectability (Iben *et al.*, 1995)[21]. Figure (1.2) outlines the distinguishing properties of Be/X-ray binary systems in comparison to the description of standard HMXBs (adapted from Trümper *et al.*, 1986)[24]. The transient sources have eccentric orbits (e $\sim$ 0.1-0.8), with relatively long orbital periods. The companion is typically a Be supergiant star that ejects matter as a non-stationary wind, that is strongly collimated along its equatorial plane (Chen *et al.*, 1992)[15]. These supergiants lose $\sim 10^{-6} M_{\odot}$ yr^{-1} in a wind having a terminal velocity of the order of 10^3 kms^{-1}. Only a small fraction of matter from this wind is accreted by the neutron star.

Be stars

Be stars are a subclass of stars of spectral class B, showing emission lines. B stars appear to have a high enough surface temperature as to allow the presence of excited levels of neutral helium, which produces absorption lines in their optical spectrum. The presence of emission lines from Be stars, however, is believed to be caused by the presence of a circumstellar envelope surrounding the star. Atoms within this envelope could be excited to higher energy states by absorbing energetic photons released from the Be star. The observed emission lines can then be explained on the basis that these atoms will re-emit lower energy photons during deexcitation. There is also extreme variability in the amount of matter ejected from the Be star, and this is one explanation of the recurrent x-ray bursts observed from accreting

neutron stars in these systems. This consideration has been investigated by Lamb *et al.*, (1977)[11], who show that under certain conditions the intermittent, spherically-symmetric flow from a companion star can result in time-dependent emission from the neutron stellar surface which accounts for observed behaviour in bursting x-ray sources. Another possible explanation of the x-ray variability observed in Be/X-ray binary systems may be attributed to highly non-stationary, inhomogeneous accretion on the magnetic neutron star as a result of instabilities at the inner edge of the neutron star's accretion disk (Morfill *et al.*, 1984) [13]. The properties of the companion star in these binary systems greatly influence the properties of the x-ray emission from the neutron star.

1.3 EXO 2030+375

1.3.1 Physical parameters

The transient x-ray source EXO 2030+375 was first discovered by Parmar *et al.*, (1989)[5] using the EXOSAT satellite. First observations were made on May 18, 1985 when its luminosity was 10^{38} ergs s^{-1}, and continued till August 13, in which the luminosity decreased to $1.2{\cdot}10^{36}$ ergs s^{-1}. Direct observations were again made several months later on October 29, 30. A series of six flares were seen during the last of these pointed observations. Each flare had an integrated energy of $\sim 5{\cdot}10^{40}$ ergs and a duration varying between 1 hr 19 minutes and 2 hr 15 minutes. The interval between these flares varied between 3 hr 16 minutes and 4 hr 22 minutes. 42 second pulsations across the sequence of observations were also detected. The orbital period of (44.3 - 48.6 days) and eccentricity ($\sim 0.3 \pm 0.03$) were determined

from measurements of the x-ray pulse arrival times. This allowed calculation of the mass function, f(M), according to,

$$f(M) = \frac{4\pi^2(a_x sin\ i)^3}{GP_{orb}^2} = \frac{M_c sin^3\ i}{(1+q)^2}. \tag{1.1}$$

where M_c is the mass of the companion star, i is the inclination of the orbital plane with respect to the observer, P_{orb} is the orbital period, a_x is the semimajor axis of the neutron star's orbit, and $q = M/M_c$ is the mass ratio. The mass ratio of EXO 2030+375 is (9.8 $\pm$ 2.7), and q is a direct ratio that can be determined from the velocity of the companion star to that of the neutron star,

$$q = \frac{a_c sin\ i}{a_x sin\ i} = \frac{K_c P_{orb}\sqrt{1-e^2}}{2\pi a_x sin\ i} \tag{1.2}$$

$a_c$sini is the projected semimajor axis of the companion's orbit, K_c is the semi-amplitude of optical Doppler velocity curve, and e is the orbital eccentricity. EXO 2030+375 has a value for $a_x sin\ i$ of (208 $\pm$ 25) $lt - sec$, and $i > 50°$ (Stollberg *et al.*, 1994)[31][10]. Using observed changes in the spin rate of the neutron star, the distance of (5.0-5.6) kpc, and magnetic moment μ =(1.1 - 2.4)·10^{31}Gcm^3 were determined. Figure (1.3)[1] is a depiction of the EXO 2030+375 binary system showing the orbital movement of the neutron star (which may also have an accretion disk) through the Be stellar disk.

1.3.2 X-ray spectrum

The energy spectra of most x-ray pulsars are characterized by a power-law spectral energy distribution at energies below a cut-off energy, E_c, typically $\sim$ $15keV$.

[1]http://www.astro.soton.ac.uk/ ind/bex.html

Above this energy, the spectrum falls off more rapidly than can be explained by extrapolation of the power-law. The power-law equation is given as,

$$F(E) = E^{-\Gamma} exp[(E - E_c)/E_f] \tag{1.3}$$

where F(E) is the flux measured at the observer, E_f is a scaling factor, and Γ denotes the photon or spectral energy index. Parmar *et al.*, (1989)[5] has used this model in analysis of the observed spectrum of EXO 2030+375, determining best-fit values for the photon index of $\Gamma = (1.83 \pm 0.02)$, $E_c = (18.1 \pm 1.5)$ keV and $E_f = 39^{+20}_{-14}$ keV with an equivalent hydrogen column density of $(3.08 \pm 0.15) \cdot 10^{22}$ atoms cm^{-2}. Fits to the phase-averaged spectra obtained from EXO 2030+375 indicate that as the luminosity decreased, the spectra became 'harder', such that when $L = 1.2 \cdot 10^{37}$ ergs s^{-1}, the photon index was $\Gamma = (1.20 \pm 0.07)$. In addition, the high-energy cut-off also decreased with decreasing luminosity. The best-fit parameters from each spectrum were used to compute 1-20 keV luminosities, for an assumed distance of 5 kpc. These luminosities coincide with the observed pulse profiles, presented in chapter 4. Using the best-fit parameters of Parmar *et al.*, (1989)[5], the mean energy for a given photon index can be calculated using the following equation,

$$\bar{E} = \left(\int_{E_1}^{E_2} E \cdot F(E) dE \right) / g \tag{1.4}$$

where g is the normalization factor,

$$g = \int_{E_1}^{E_2} F(E) dE \tag{1.5}$$

Quoted values of pulse profiles and energies are for 1-10 keV and 1-20 keV, but 2-10 keV and 2-20 keV were used, since the detector was not very sensitive in the 1-2

keV energy range. Numerical fitting of these pulse profiles for a specific energy uses a value for the energy of observed photons, E_{obs}, of 4.5 keV. This value is close to the mean energy within the range 2-10 keV, calculated using equation (1.4) for the photon indices $\Gamma = 1.20$, $\bar{E} = 4.895$ keV, and $\Gamma = 1.83$, $\bar{E} = 4.277$ keV. The 1-20 keV luminosities (ergs s^{-1}) for each of the 1-10 keV pulse profiles require a conversion factor for the energy-integrated theoretical flux, namely,

$$L_{conv} = \frac{\int_2^{10} E \cdot F(E) dE}{\int_2^{20} E \cdot F(E) dE} \tag{1.6}$$

$L_{conv} = 0.601$, for $\Gamma = 1.83$, and 0.436, for $\Gamma = 1.20$. For theoretical pulse profiles specific to the energy 4.5 keV, the luminosity conversion factors L_{conv} are 0.136 and 0.129 for photon indices $\Gamma = 1.20, 1.83$ respectively. L_{conv} converts the theoretical flux, F_{theor}, to the observed flux, F_{obs}, according to,

$$F_{theor} = F_{obs} \cdot L_{conv} \tag{1.7}$$

In the numerical calculations of the *flat* space emission model developed in this thesis, the observed flux (cts s^{-1}) was converted to its 6 keV value in order to fit the energy-specific theoretical flux profiles.

$$L_{ct} = \frac{L_{(1-20)} N}{19 keV \; x \; 6 keV}, \tag{1.8}$$

$$F_{ct} = \frac{L_{ct}}{4\pi d^2} \tag{1.9}$$

where L_{ct} is the count luminosity averaged over pulse phase (units of cts s^{-1} keV^{-1}), N is the number of detector photon counts, and $L_{(1-20)}$ is the 1-20 keV luminosity in units of keV s^{-1}) for a distance d of 5 kpc. For the May 18, EXOSAT pulse profile of EXO 2030+375, having an observed luminosity of $1.0 \cdot 10^{38}$ ergs/s, the value of F_{ct} is 0.183 cts s^{-1} keV^{-1} cm^{-2}.

The BATSE x-ray spectrum

The x-ray spectrum corresponding to the Burst and Transient Source Experiment (BATSE) observations of EXO 2030+375 is shown in Figure (1.4) (Norton *et al.*, 1994)[2]. Each of the 12 observed outbursts were seen in seven Large Area Detector (LAD) 2.048 time resolved energy channels (20-120) keV. The first three channels (20-50) keV registered the largest part of the x-ray signal (Stollberg *et al.*, 1994)[31]. Spectral fitting for the integrated flux within the energy range (20-50) keV was performed using an Optically Thin Thermal Bremsstrahlung (OTTB) model with a pivot energy of 44 keV (Stollberg *et al.*, 1994)[31]. Fitting of the BATSE spectrum indicates a bias towards lower energies of the channel range (20-50) keV. The mean energies for the energy range (20-50) keV of the BATSE pulse profiles were calculated using equation (1.4) for Γ=1.20 and Γ=1.83, as 32.8 and 34.2 keV respectively. For a flat spectrum (F(E)=constant), the expected mean energy is,

$$\begin{aligned} \bar{E} &= \frac{\int_{E_1}^{E_2} E \cdot F(E) dE}{\int_{E_1}^{E_2} F(E) dE} = \frac{F(E) \int_{E_1}^{E_2} E \cdot dE}{F(E) \int_{E_1}^{E_2} dE} \\ &= \frac{1}{2} \frac{E_2^2 - E_1^2}{E_2 - E_1} \\ &= \frac{1}{2} \frac{(E_2 + E_1)(E_2 - E_1)}{E_2 - E_1} \\ &= \frac{E_1 + E_2}{2} = \frac{(20 + 50) keV}{2} = 35 keV \end{aligned} \tag{1.10}$$

The luminosity conversion factors $L_{ct,\omega}$ at the specific energy of 35 keV are 0.030 and 0.032 for Γ = 1.20 and Γ = 1.83, respectively. The theoretical profiles of the emission model were fitted to the observed profiles at 10 and 35 keV. The results of varying the E_{obs} energy are presented in the numerical results section.

1.4 Accretion onto Neutron Stars

The transfer of mass from the companion star to the compact, neutron star in a binary system can take place in two different ways; by *Roche/tidal lobe* overflow, or by a stellar wind. Figure (1.5) contrasts these two processes (Börner, 1980)[6]. Roche lobe or tidal lobe overflow occurs when matter flows over the gravitational potential saddle point or 'inner Lagrangian' point between the two stars. The common equipotential surface for each star that passes through the Lagrangian point (LP) is termed a Roche lobe if the spin of the neutron star is synchronized with the rotation of the binary system, or a tidal lobe if the neutron star is not rotating significantly. The companion star expands, filling its Roche lobe and loses matter through the LP at approximate rates of $3 \cdot 10^{-4}$-$3 \cdot 10^{-8} M_{\odot}\ yr^{-1}$. Disruption to the flow of matter through the LP can arise due to nuclear burning in the companion star, magnetic braking of the orbital motion, and tidal coupling between the neutron star and the accreting plasma of matter (Ventura and Pines, 1991)[25]. The difference between the rotation rates of both stars has a large effect on the rate and amount of matter that is accreted by the neutron star. For the case of spherical, steady-accretion[2] of matter at a rate $\dot{M}$ onto the neutron star (mass M_x, radius R_x), at a free-fall velocity, v_{ff}, the emergent luminosity is,

$$L_x = \frac{1}{2}\dot{M}v_{ff}^2 = \frac{G\dot{M}M_x}{R_x}, \tag{1.11}$$

This equation assumes that all the energy of the inflowing matter is converted to gravitational potential energy, which subsequently heats the surrounding gas and

[2]equations 1.11 to 1.14 are from Shapiro and Teukolosky, (1983)[45].

causes radiation emission. Figure (1.6)[3] depicts the accretion process and the resulting x-ray emission. The efficiency of this radiant emission is estimated according to the ratio,

$$\epsilon = \frac{L_x}{\dot{M}c^2} = \frac{GM_x}{R_x c^2}, \tag{1.12}$$

and for neutron stars $\epsilon \sim 0.1$ (Börner, 1980)[6]. With the majority of this emission being thermal-blackbody radiation from the surface of the neutron star of temperature T_b, and assuming that the accreting matter is optically thick, then,

$$L_x = 4\pi R_x^2 \sigma T_b^4 \tag{1.13}$$

and an approximate value for the observed luminosity can be found. For an observed luminosity of the order of 10^{37} ergs s^{-1}, and R_x=10 km, the temperature $T_b \sim 10^8$ K ($\sim$ 1 keV). The luminosity range for the EXOSAT and BATSE observations of EXO 2030+375 range between 10^{36}-10^{38} ergs s^{-1}. This indicates that low accretion rates onto the neutron star in EXO 2030+375 of $\sim 8.5 \cdot 10^{-9} - 8.5 \cdot 10^{-9} M_\odot yr^{-1}$ are sufficient to give the observed range of luminosity. Such accretion rates are far less than those expected from Roche lobe overflow through the LP point of $3{\cdot}10^{-4} - 3{\cdot}10^{-8} M_\odot$ yr^{-1} which suggests that accretion by the neutron star in EXO 2030+375 may be from a stellar wind of the companion star. Waters *et al.*, (1988)[28] have calculated the expected luminosity from low velocity winds in Be/X-ray binaries based on a simple wind accretion model. This model assumes that the radius in which matter is accreted by the neutron star is much smaller than the vertical extent of the disk of the Be star. For a compact object at periastron, they derive an expected

[3]http://www.astro.soton.ac.uk/ ind/xrpulsar.html

luminosity of,

$$L_x = 4\pi G^3 M_x^3 R_x^{-1} a^{-2}(1-e)^{-2} R_* \left(1 + \frac{v_{orb}^2}{v_w^2}\right)^{-3/2} v_w^{-4} F_* \qquad (1.14)$$

where a and e are the semi-major axis and eccentricity of the orbit, R_* and F_* are the radius and mass flux of the Be star, M_x and R_x are the mass and radius of the neutron star. V_{orb} and v_w are the orbital velocity of the neutron star, and *radial* outflow velocity of the Be star respectively. Kepler's third law can be substituted into equation (1.14) and re-stated involving the orbital period, P_{orb}, of the binary system. Setting P_{orb}=46 days, M_x=1.4$M_\odot$, R_x=10 km, R_*=10$R_\odot$, $F_* \sim 10^{-6}$ g cm^{-2} s^{-1}, v_w=100 km s^{-1}, $v_{orb} \sim v_w$, and e=0.33, an estimate of the expected luminosity of the EXO 2030+375 system is calculated to be $\sim 2{\cdot}10^{37}$ ergs s^{-1}. Accordingly, accretion from a spherical stellar wind can explain the observed luminosity range of EXO 2030+375. The approximate distance at which matter from a stellar wind is gravitationally captured is termed the 'accretion radius', and is important in specifying the x-ray emission geometry of a neutron star.

$$r_a = \zeta \frac{2GM_x}{(v_{rel}^2 + c_s^2)} \sim 2.65{\cdot}10^{10}{\cdot}M_x \frac{(v_{rel}^2 + c_s^2)}{1000\ kms^{-1}}\ cm \qquad (1.15)$$

where $\zeta \sim 1$ is a geometrical constant, c_s is the sound speed of the gas in the accretion stream, and v_{rel} is the relative velocity between the neutron star of mass M_x and the accretion stream of gas (Henrichs, 1983)[19]. For EXO 2030+375 the calculated accretion radius for c_s=10 km s^{-1}, $v_{rel} \sim v_{orb} \sim$ 10 km s^{-1} (low velocity wind), is $\sim 7.0 \cdot 10^4 km$.

The Ghosh and Lamb accretion model

Parmar *et al.* (1989)[5] have correlated the spin period and x-ray luminosity of EXO 2030+375, according to function $-\dot{P}_s \propto \mathrm{L}^m$, where $\dot{P}_s$ is the time rate of change of the spin-period of the neutron star, L is the observed luminosity, and m is a parameter of the model (Ghosh and Lamb, 1979)[32]. Acceptable fits for the Ghosh and Lamb accretion torque model were obtained only for the two lowest luminosities observed from EXO 2030+375. This model assumes that the magnetic field of the neutron star is not completely excluded from an accretion disk and that partial threading of magnetic flux through the disk exerts a torque which slows the spin of the neutron star when the radius r_m (equation 1.16 below) is close to the corotation radius, r_c (equation 1.17). As a result of the dependence $-\dot{P}_s$ on luminosity being substantially different for their simplified model, their results suggest that a more detailed consideration of the interaction of the neutron star's magnetosphere with an accretion disk is needed for EXO 2030+375. It is suggested that if the accretion disk is perfectly diamagnetic and surface currents exclude the stellar magnetic field, the regions of the disk outside the corotation radius may be responsible for a centrifugal wind which carries away angular momentum, thereby reducing $\dot{P}_s$ (Ghosh and Lamb, 1979)[32]. In comparison to the stellar wind accretion radius calculated in the preceeding section, an estimate of the Alfvén or magnetospheric radius for disk accretion is obtained by equating the ram pressure of radially inflowing matter having a velocity v_r; ρv_r^2 (spherical accretion), to the magnetic pressure, $B^2/8\pi$. This yields,

$$r_m = 3{\cdot}10^8 \mu_{30}^{4/7} M_x^{1/7} R_6^{-2/7} L_{37}^{-2/7} \ cm, \tag{1.16}$$

where $\mu_{30} = \mu/10^{30}$ is the magnetic moment of the neutron star in G cm^3, M_x is the mass of the neutron star in solar units, R_6 is the radius in units of 10^6 cm and L_{37} is the x-ray luminosity in units of 10^{37} ergs s^{-1}. For EXO 2030+375, the calculated value of r_m from its highest observed luminosity of $1{\cdot}10^{38}$ ergs s^{-1} to its lowest of $1.2{\cdot}10^{36}$ ergs s^{-1}, using $\mu_{30} = 11.5$, $M_x = 1.4$, $R_6 = 1.0$, varies from (6.58 - 23.3)$\cdot 10^4$ km respectively. The strength of the magnetic field, B, for neutron stars is typically 10^{12} Gauss. The distance, r_m, is interpreted as the radius at which matter inflow begins to be stopped by magnetic stresses of the stellar magnetic field of a neutron star. Comparison of the accretion radius of a stellar wind of $\sim 7.0 \cdot 10^4$ from equation (1.15) with the calculated range of $r_m \sim (6.58-23.3){\cdot}10^4$ km suggests that the stellar wind from the companion star is of high velocity and far greater than $v_{rel} \sim v_{orb} \sim 10$ km s^{-1}. Whether an x-ray binary accretes matter from a stellar wind or from an accretion disk, the extent of the accretion radius is large. The distant accretion flow is important in establishing boundary conditions (initial conditions) for matter which forms the x-ray emission or accretion columns of neutron stars (Mészáros, 1992)[35]. These initial conditions are determined according to the initial magnetic field lines along which matter is channeled along the polar regions of the neutron star, possibly reaching its surface. Contrary to such an assumption, (Illarionov and Sunyaev, 1975)[1] have described a 'propellar effect' whereby even though matter is dominated by the magnetic field within the radius r_m, the centrifugal force can cause matter to be thrown far away from the neutron star. The radius in which this effect can take place is termed the co-rotation radius and is estimated by balancing

gravity and the centrifugal force,

$$r_c = \frac{GM_x}{\Omega_s^2}^{1/3} \sim 1.5 \cdot P^{2/3} M_x^{1/3} \; cm \tag{1.17}$$

where Ω_s is the spin-period of the neutron star. Assuming that magnetohydrodynamic (MHD) instabilities do not cause matter to exchange field lines, the initial loading of the field lines at r_m will determine the loading of the emission regions, and therefore its emission geometry. Figure (1.7) adapted from Ghosh and Lamb, 1979[33] shows the Ghosh and Lamb disk model and the connection of the stellar magnetic field lines from the accretion disk at r_m to the emission regions of a neutron star.

1.5 Proposed Emission Region Geometries

The size of the region with respect to the radius r_m in which accreted matter attaches or 'threads' to the magnetic field lines of a neutron star is presently unclear. Focus in the study of neutron stars in binary systems has instead been given to establishing the geometry of their emission regions through a comparison of the observations of their x-ray emission with theoretical models. The x-ray emission geometry indirectly determines the extent of the threaded region; a completely filled column of emission suggests that this region is large, allowing extensive loading of magnetic field lines, whereas a partially-filled region (hollow funnel) might indicate a small region for the accreted matter to be channelled to the polar regions. Furthermore, the possibility of unequal loading of matter from an accretion disk leads to different amounts of matter being channelled to each polar region of the neutron star. The asymmetric loading of matter from an accretion disk may arise from uneven contact between the

magnetosphere and accretion disk. The four diagrams at the top of Figure (1.8) show the wide range of possible emission region geometries (Mészáros, 1984)[34]. Instabilities in the accretion flow may cause the accretion flow to be disrupted breaking it into subdivided regions, both vertical and horizontal to the neutron star surface (Elsner and Lamb, 1976)[40]. The two lower diagrams of Figure (1.8) depict the two distinct geometries of emission in neutron stars: fan-beam and pencil-beam emission (Mészáros, 1984)[34].

A standoff shock

Zeldovich and Shakura, (1986)[52] have proposed that plasma effects which induce a collisionless, standoff shock region, lying above the neutron star surface, may be present in the emission regions of high-luminosity (L>10^{37}) ergs s^{-1} x-ray pulsars. The solution of one-dimensional hydrodynamic and radiative diffusion equations shows that the outgoing radiation will not shock the inflowing stream of accreted gas until,

$$L_x > 5{\cdot}10^{36}\frac{\sigma_T}{\sigma_s} r_5 R_6^{-1} M_{1.4} \tag{1.18}$$

where $\sigma_T = 6.653{\cdot}10^{-29}\mathrm{m}^2$ is the Thomson cross-section for scattering of unpolarized radiation incident upon a stationary electron, σ_s is the effective scattering cross section, r_5 is the radius of the emission region in units of 10^5cm, and R_6 and $M_{1.4}$ are the radius and mass of the neutron star in units of 10^6cm and $1.4M_\odot$ respectively. In the case where a shock exists in the emission region, x-ray emission from the post-shock region below is directed outwards, perpendicular to the magnetic field at the neutron star surface, resulting in 'fan-beam' emission. The height of this standoff shock decreases with decreasing luminosity. In the absence of a shock, for sufficiently

low luminosities, inflowing particles in the emission region decelerate via multiple Coulomb collisions producing radiation that is emitted perpendicular to the neutron star surface (pencil-beam emission).

1.6 Radiative-Transport in Strongly Magnetized Plasmas

The strong magnetic fields that surround neutron stars cause the electron energy levels to be quantized in the transverse direction. The consequence of this constraint on the electrons means that electromagnetic waves propagating in the surrounding plasma have well-defined polarization normal modes (Mészáros, 1984)[34]. For magnetic fields near to the critical value of $4.4{\cdot}10^{13}$ G, vacuum polarization involving virtual electron-positron pairs are believed to play an important role in determining the polarization properties of the atmospheric medium. Coulomb particle collision rates are also strongly dependent on the strength of the magnetic field. Mészáros, (1984,1992)[34][35] has extensively investigated the physical processes which take place in neutron star atmospheres. The complexity of determining the angle, frequency and polarization properties of neutron star atmospheres has led to the study of simplified geometries of homogeneous atmospheres containing magnetized plasma (Harding *et al.*, 1984)[3],(Nagel, 1981,1984)[49][50],(Pavlov *et al.*, 1985)[14],(Wang and Frank, 1981)[53],(Mészáros and Nagel, 1985)[36][37]

1.6.1 Numerical calculations for columns and slabs of emission

Mészáros and Nagel, (1985)[36] have performed numerical calculations of radiation transfer in magnetized plasmas for slab and cylindrical idealized atmospheres. The

slab geometry is infinite in the transverse direction, while the cylindrical geometry is infinite in height, in order to simplify the radiation field to a dependence on a single spatial dimension. The spatial dimension r (linear depth) is defined for the slabs to vary from -R to R from its line of symmetry, but varies between 0 and R between sides in the cylinder geometry. These atmospheres are homogeneous in temperature and density, and have a constant magnetic field directed either perpendicular to the slab surface, or along the cylinder axis. Generalized boundary conditions were used for these self-emitting atmospheres involving a numerical grid of eight-angles, 32 frequencies and 2 normal polarization modes. Their calculations use a magnetic field strength of $3.3{\cdot}10^{12}$ G with a cyclotron frequency $\frac{h}{2\pi}\omega_B$ of 38 keV. Temperatures satisfy $kT < \frac{h}{2\pi}w_B$ so that transitions of electrons to levels higher than $n = 1$ can be neglected. Table (1.1) outlines the physical parameters for the models considered. The numerical results of model D, for the angle and frequency dependence of emission from a deep column of depth y=$5{\cdot}10^4$ g cm^{-2} were used in specifying emission from the surface of the accretion columns in the asymmetric emission model.

1.6.2 Local emission intensity data

The intensity profiles for models (B→F) of Mészáros and Nagel, (1985) were cubic-spline fitted and corrected for changing cyclotron frequency in the r and θ direction. Figures (1.9) and (1.10) show the results of the spline interpolation for a deep column of emission. Results of spline interpolation for both the shallow/deep slabs and column emitting elements appear in the Appendix section. The data is used to define the functional dependence of local intensity on the local emission angle θ' and the cyclotron frequency $\omega = \omega_c = \omega_B$. The cyclotron frequency in the accretion

column assumes values smaller than the polar cap cyclotron frequency, due to the reduction of the magnetic field in the radial direction by a factor of $\frac{1}{r^3}$. This frequency is then further altered by the effect of relativistic redshifting to a distant observer. The cyclotron frequency in the accretion column above the neutron star decreases from the polar cap cyclotron frequency proportional to the change in the strength of the magnetic field as a function of r and θ, according to,

$$\omega_c = \frac{zeB(r,\theta)}{\gamma m} \tag{1.19}$$

For a non-relativistic electron, the charge $z = 1$, m is the rest mass of the particle, and $\gamma = \sqrt{1 - \left(\frac{v}{c}\right)^2} \rightarrow 1$, so that one has,

$$\omega_c = \frac{eB(r,\theta)}{m_e} \tag{1.20}$$

$B(r,\theta)$ is proportional to the value for the surface magnetic field strength B_o.

1.6.3 Gravitational redshift of ω_c

For purposes of the *curved* space asymmetric emission model, the effect of gravitational redshift of the frequency of radiation must be considered. The gravitational redshift of the radiation frequency is a result of the conservation of mass-energy contained within Einstein's Theory of Relativity. If one considers two particles, an electron and a positron, to be at rest, each with rest mass m_o at a large distance from the neutron star, which then subsequently fall toward its stellar surface, the total mass-energy E acquired by the particles at a distance r from the star is,

$$E \equiv m_r c^2 = \left(m_o c^2 + \frac{m_o MG}{r} \right) = m_o c^2 \left(1 + \frac{MG}{rc^2} \right) \tag{1.21}$$

Here m_o is the rest mass, M is the mass of the neutron star, G is the gravitational constant, and c is the speed of light.

These particles then collide in a head-on collision (no energy or momentum loss) as a result of their deflection from the stellar surface, and annihilate to produce two photons. These photons are then considered to escape from r without frequency shift to re-collide at a large distance from the star leading to the formation of an electron-positron pair. With energy conserved, the frequency seen by a distant observer at a distance d is less than the emitted frequency at r, and is given by,

$$\omega_c(d) = \omega_c(r) \left(1 + \frac{MG}{rc^2} \right)^{-1} \tag{1.22}$$

One can also express the shift in frequency from $r \rightarrow d$, denoted $\Delta\omega$, as a fractional change of the local cyclotron frequency,

$$\frac{\Delta\omega}{\omega_c(r)} = \left\{ \frac{\omega_c(d) - \omega_c(r)}{\omega_c(r)} \right\} = -\frac{MG}{rc^2} \left[1 + \frac{MG}{rc^2} \right]^{-1} \tag{1.23}$$

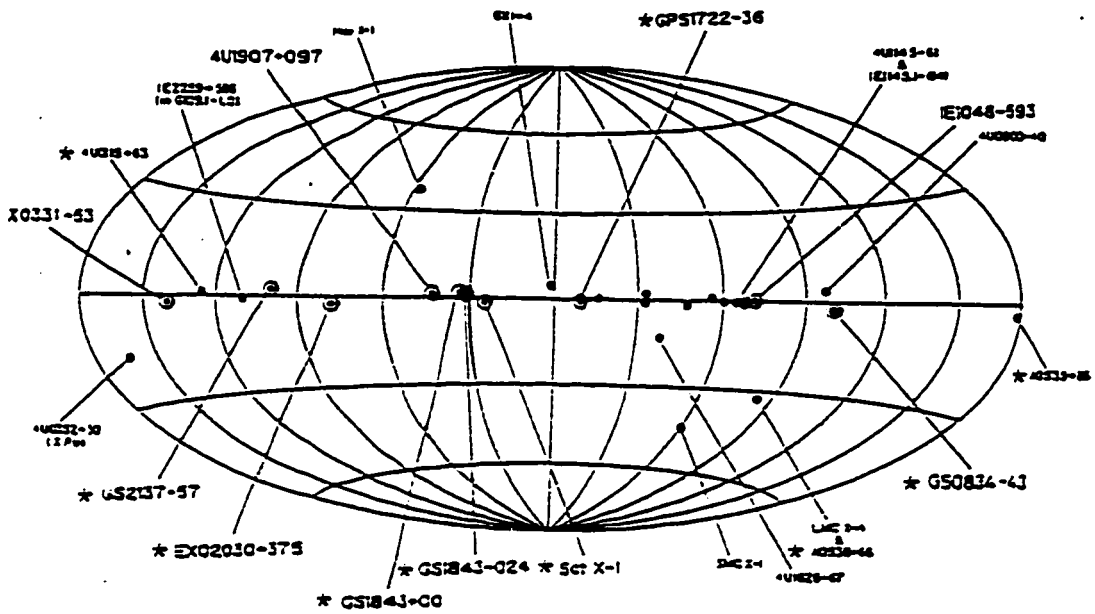

Figure 1.1: The galactic distribution of binary x-ray sources, showing the location of EXO 2030+375 near the galactic plane, transient sources are indicated with an asterisk (Tanaka *et al*, 1992).

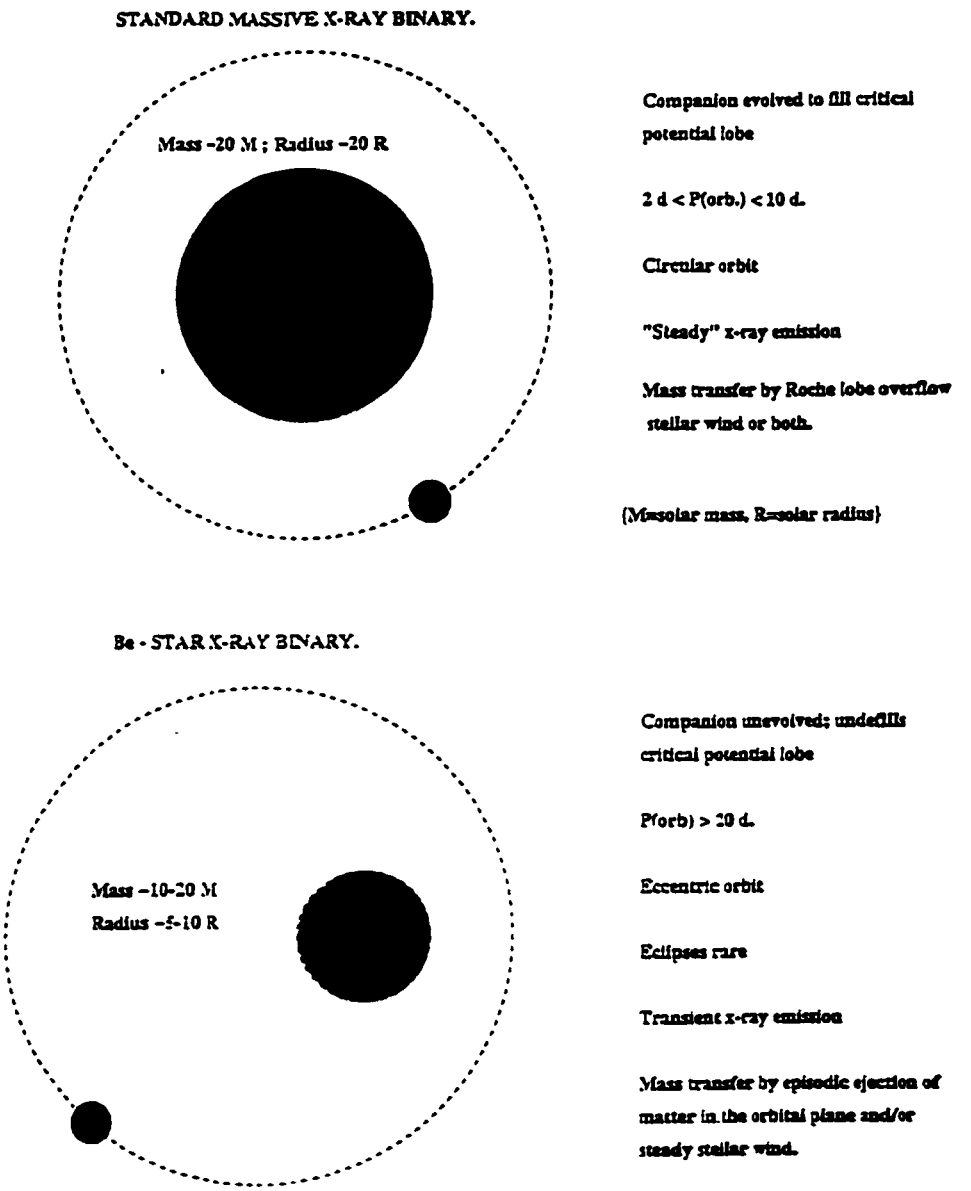

Figure 1.2: Comparative outline of standard High-Mass, and Be/X-ray binary systems (adapted from Trümper *et al*, 1986).

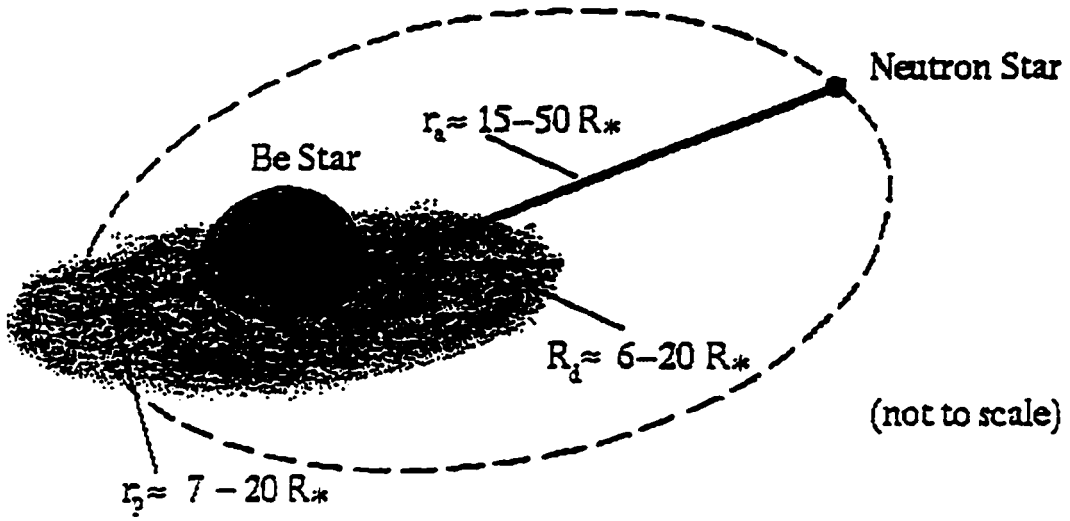

Figure 1.3: The binary system EXO 2030+375 (http://www.astro.soton.ac.uk).

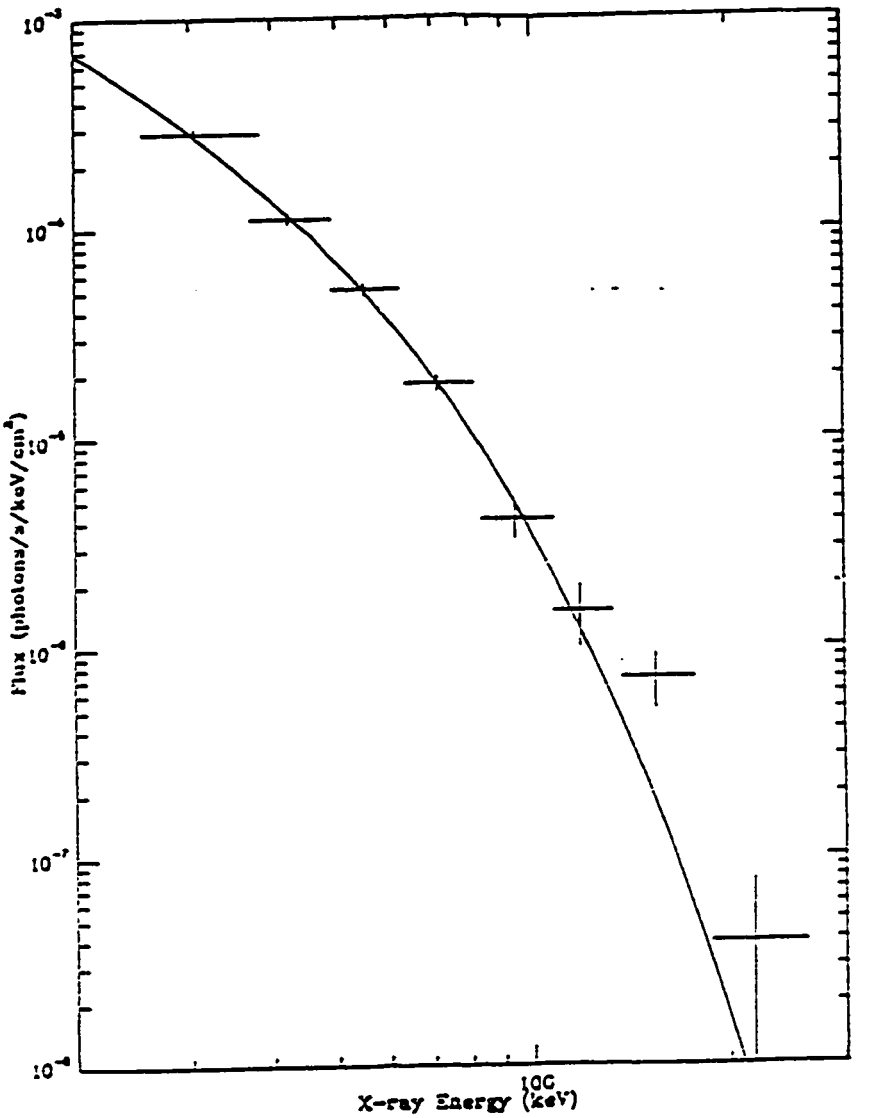

Figure 1.4: The mean BATSE x-ray spectrum of EXO 2030+375 during an observed outburst. The solid line is a best-fit curve for a thermal bremstrahlung model for the pulsed x-ray flux (Norton *et al*, 1994).

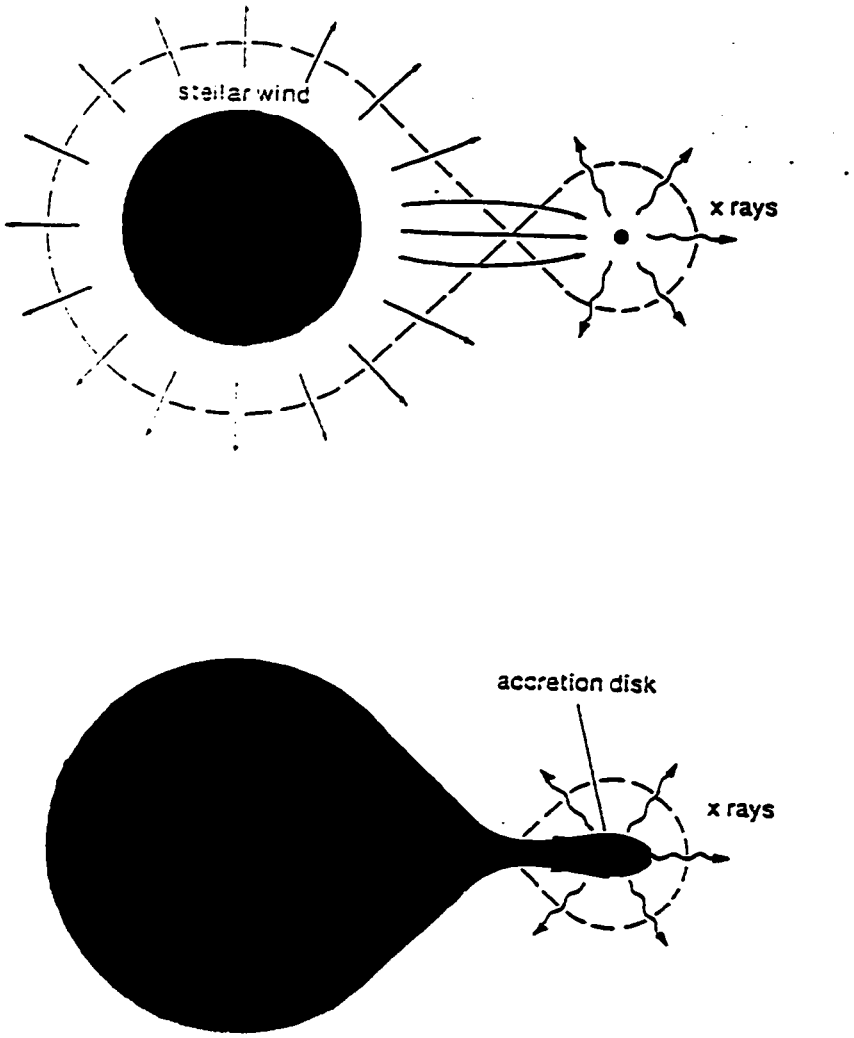

Figure 1.5: Mass accretion by the neutron star from its companion; via a stellar-wind or Roche-lobe overflow resulting in the formation of an accretion disk around the neutron star (Börner, 1980).

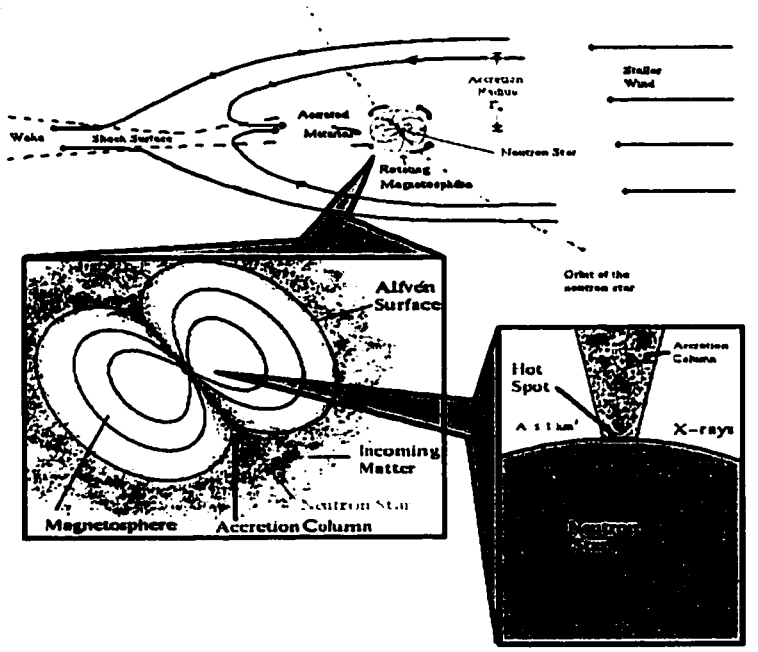

Figure 1.6: The process of mass accretion leading to x-ray emission from a neutron star (http://www.astro.soton.ac.uk/ ind/xrpulsar.html).

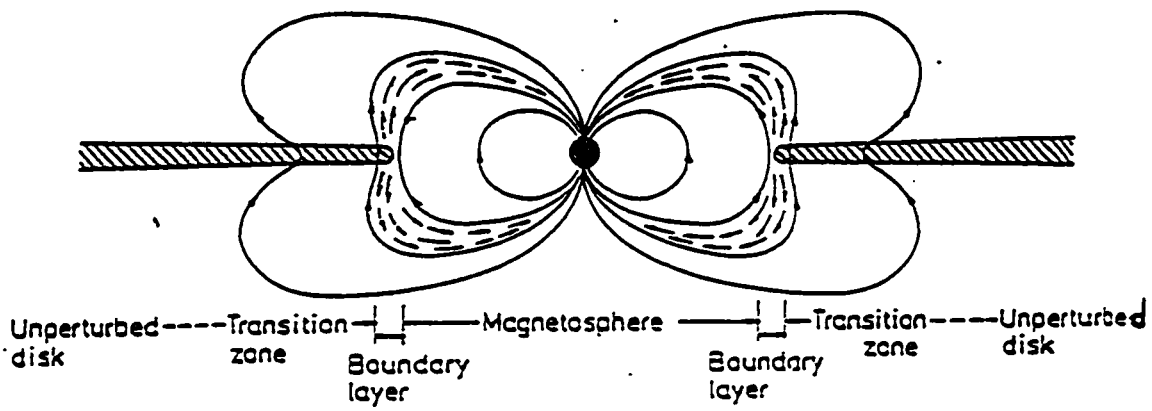

Figure 1.7: The Ghosh and Lamb model of disk accretion (adapted from Ghosh and Lamb, 1979).

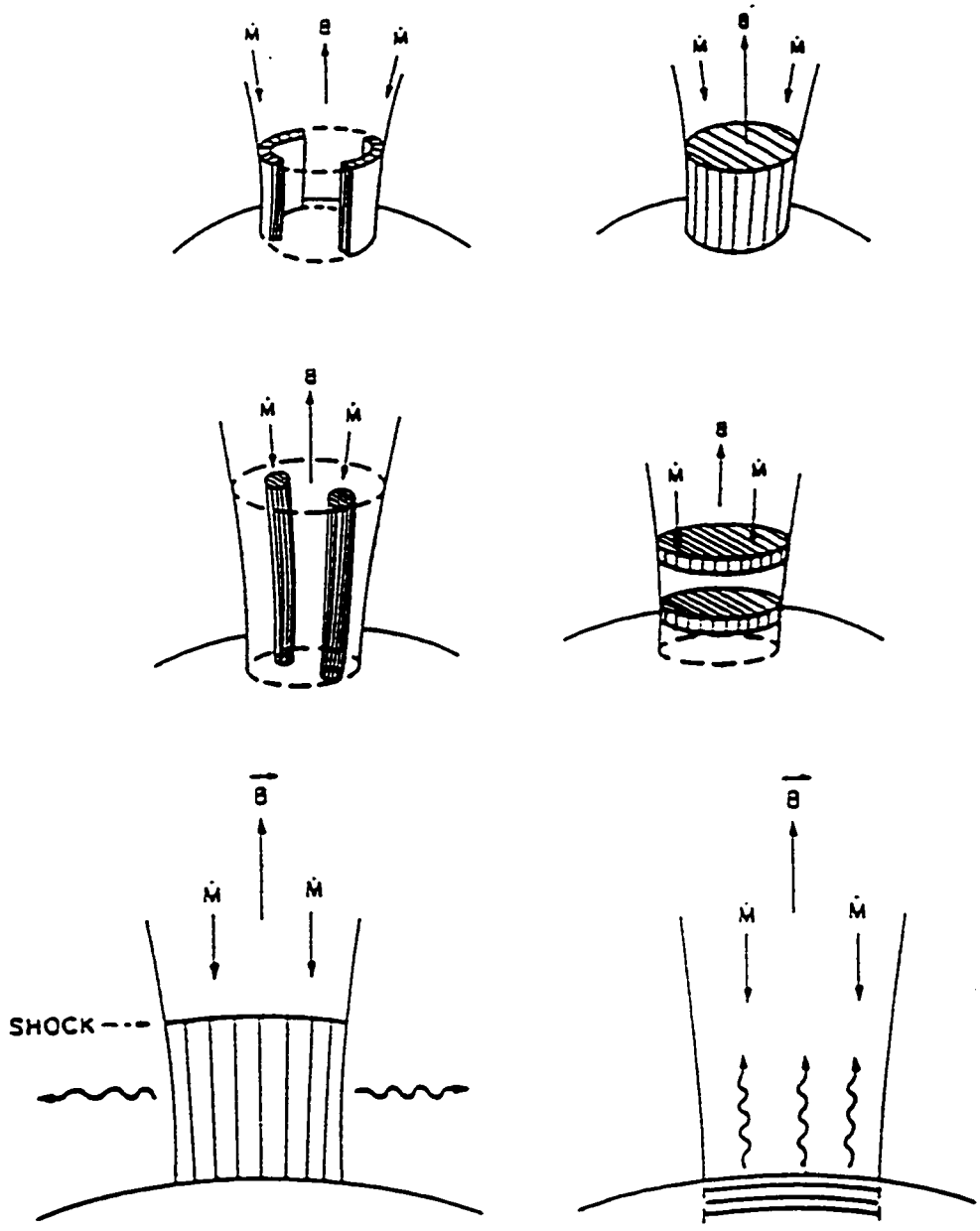

Figure 1.8: Top: model depictions for possible slab and columned filling of an emission region. Bottom: The direction of photon emission for the cases of a shock front above the neutron star (NS) surface, (fan-beam emission), and with emission directly from the NS surface, (pencil-beam emission) (Mészáros, 1984).

Model Descriptions and Parameters

($B = 3.3 \times 10^{12}$G, cyclotron frequency = $(h/2\pi)\omega_n = 38$ keV)

Models	Plasma Parameters				
	density(g/cm^3)	kT (keV)	$(h/2\pi)\omega_B$ (keV)	radius (cm)	depth (g/cm^2)
shallow slab - model B	0.50	8.0	38.0	10^2	50.0
shallow column - model C	0.50	8.0	38.0	10^2	50.0
deep slab - model E	0.50	8.0	38.0	10^5	5×10^4
deep column - model D	0.50	8.0	38.0	10^5	5×10^4
special slab* - model F	1.67×10^{-4}	7.0	38.0	$= 10^4$	5×10^{-2}

*slab model with exterior illuminating source (all other models are self-illuminating)

Note: $\tau_T >> 1$ in both the deep and shallow cases ($\tau_T = 20$ (shallow) and $\tau_T = 2 \times 10^4$ (deep))

Table 1.1: Physical parameters for the calculations of Mészáros, 1985, for magnetized slab and column emitting elements. Model D for an optically-thick, self-illuminating, planar region of Thomson optical depth, ($\tau_T = 2 \cdot 10^4$), with a magnetic field perpendicular to the surface was used for surface emission.

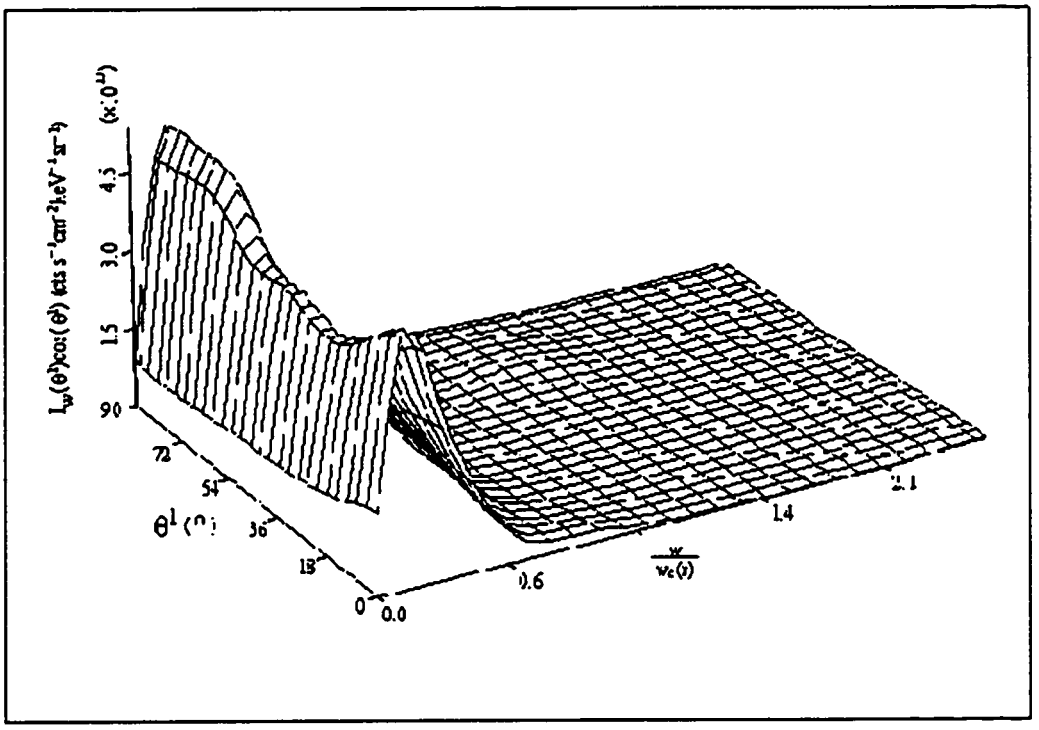

Figure 1.9: 2D-dimensional spline interpolation of radiative transfer data for a deep column of emission.

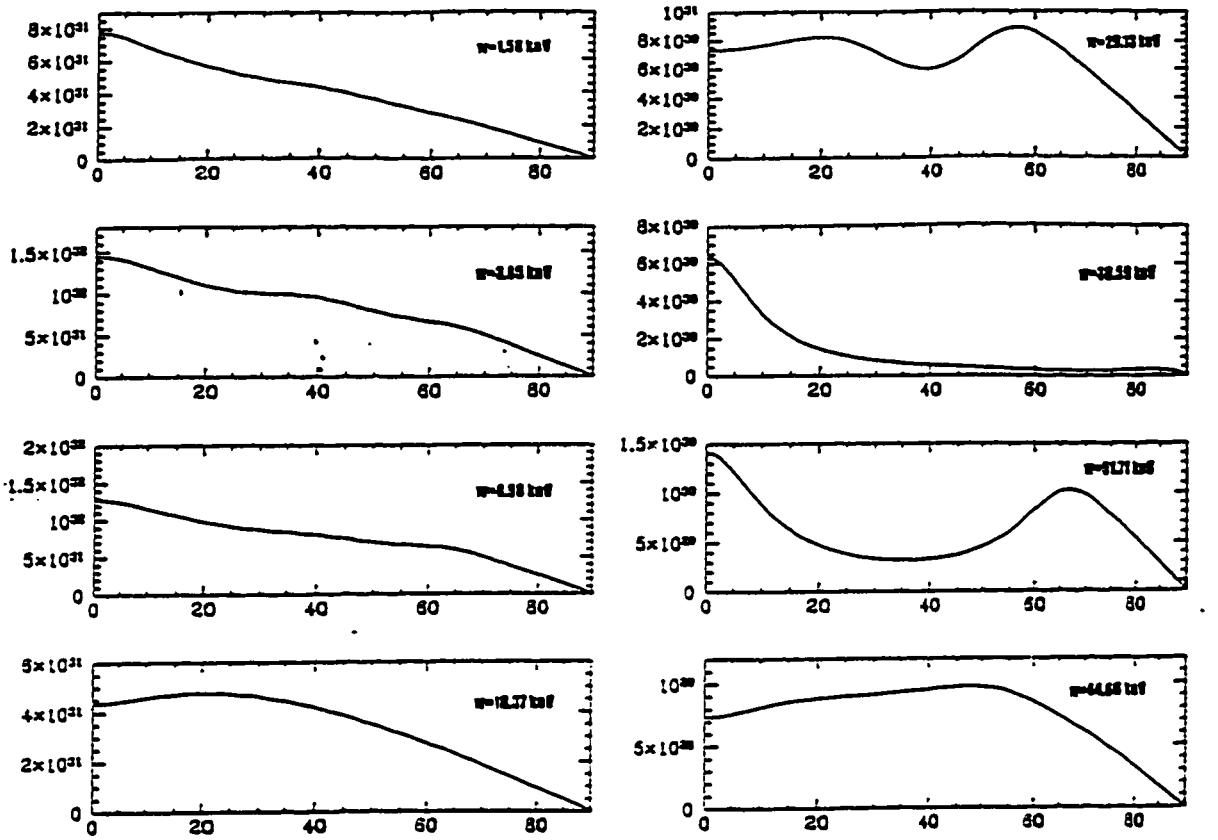

Figure 1.10: Spline interpolation curves of local emission intensity $I_\omega cos(\theta')$ in photons $s^{-1}cm^{-2}keV^{-1}sr^{-1}$ versus emission angle, θ', for a self-illuminating column of density 0.50 g cm^{-3}, radius 10^5 cm, $kT = 38.0$ keV, and atmospheric depth $5 \cdot 10^4$ g cm^{-2}.

Chapter 2

Asymmetric Emission Model of EXO 2030+375

2.1 Motivation

2.1.1 Phenomenological models

In the field of astrophysics, advanced numerical methods are often employed in solving sets of equations in order to develop self-consistent computer models. The purpose of such an endeavour, for instance, may be to examine physical processes taking place at a microscopic level. However, in physical systems which are not readily testable, the normal scientific method has difficulties due to the lack of experimental data. The importance of phenomenological models in the development of a science is to raise new hypotheses. The reductionist approach to scientific practice suggests that in striving to produce meaningful conclusions through rational, deductive thought, one relies also on being able to reduce problems into individual or compartmental concepts. The process of such a building block approach has both its benefits as well as its disadvantages. It is for this reason that phenomenological models are useful. It is important, however, that these models are developed to include reasonable explanations to what is already known, or believed to be true, and be applied in such a way that the fitting of such models to observations can lead to further deductions. The framework of science itself is comprised of interconnecting, successive deductions, and the unification of concepts can often lead to new and significant discoveries. Nonetheless, if phenomenological models are to lead to meaningful and

verifiable conclusions, they must at the same time be able to reproduce scientifically accepted ones as well. This is necessary, for example, in order for such conclusions to be used in deciding between different, or even competing theories.

In trying to explain observations from Be/X-ray binary systems, many different theories presently exist concerning the geometry of the emission region, the neutron star accretion process, the presence of a disk, stellar-wind, or 'disc-like' wind around the neutron star. This is one reason why a phenomenological model for the emission region is constructed. Its geometry partly depicts the standard model of such systems, (Davidson and Ostriker, 1973)[27], and extends the work of recently developed models (Riffert and Mészáros, 1988)[18]. Certain aspects of the geometry include new considerations; the effect of gravitational light-bending on emission seen by an external observer, the realistic reduction of the cyclotron frequency with height above the emission polar cap, the effect of the curvature of magnetic field lines on which accreted matter flows, and how variable accretion rates alter the emission geometry of a neutron star.

2.2 The Emission Model

This emission model considers the asymmetric loading of matter onto the magnetic field lines of a neutron star as providing the basis for the asymmetry observed in the pulse profiles of EXO 2030+375, obtained by the EXOSAT and BATSE satellites. Due to the strong gravitational attraction of the neutron star in this binary system, matter is drawn from the Be companion either by a stellar wind, or by matter flowing through the Lagrangian point of the system. This matter forms a disk around the

neutron star. Magnetic stresses remove angular momentum from the gas in the disk, so rapidly that gas flow at Keplerian velocities soon ends. Once within the magnetosphere, the strong gravitational field of the neutron star pulls matter from the accretion disk. Matter then flows along the magnetic field lines towards the poles of the neutron star. The amount of matter available for loading the magnetic field lines is variable and depends on the variable separation distance (eccentric orbit) between the neutron star and its companion. This suggests that at different points along the neutron star's orbital path, only certain magnetic field lines will be responsible for particle loading. Therefore, the emission region of the neutron star can be partially-filled (i.e. asymmetric about the magnetic axis in the azimuthal direction, φ). The limits on φ, $(\varphi : \varphi_0 \rightarrow \varphi_L)$ are free parameters in the model and alter the overall azimuthal-symmetry of the emission geometry into a partial or asymmetric one responsible for photon emission (see Figure 2.1). The equation for the magnetic field lines are used to define the sides of the emission regions and are taken as that of a normal dipole field (flat space) or as a corrected equation for the dipole magnetic field under Schwarzschild geometry (curved space). A second emission region is located on the opposite polar region from the first and is bounded in the same way. The symmetry axis of the second emission can be offset from the neutron star's magnetic axis by angles $(\theta_{off}, \varphi_{off})$ as shown in Figure (2.3). The parameter θ_m, takes in account the situation where the magnetic axis and the rotation axis of the neutron star are not aligned, so that only a fraction of the field lines will intercept an accretion disk at angles favorable for accretion. An additional tilt angle where the plane of rotation is inclined with respect to the orbital axis of the binary system could be considered, but is not at this point an initial consideration

of this model. At high accretion rates (high luminosities) it is expected that a sheet of decelerating plasma extends upwards from the stellar surface. The height of each emission region above the stellar surface, denoted $R_c^{(1)}$ and $R_c^{(2)}$ for emission region 1 and 2 respectively, is also a free parameter in this model.

2.2.1 The model parameters

When gravitational light-bending is neglected, the general model considers two emission regions of different size, with one emission region offset from the first. This model has 16 parameters which relate directly to the model geometry and are involved in the fitting procedure. E_{cyc} is the neutron star surface cyclotron energy, and E_{obs} is the observed energy.

$$F_T = F_T(\mathbf{R}_o, \theta_o, \mathbf{d}, \theta_m, \theta_r, \tilde{\phi}_1, \theta_{off}, \phi_{off}, \varphi_o^{(1)}, \varphi_o^{(2)}, \varphi_L^{(1)}, \varphi_L^{(2)}, \mathbf{R}_L^{(1)}, \mathbf{R}_L^{(2)}, \mathbf{\Phi}_o, \Phi) \quad (2.1)$$

R_o - radius of neutron star

θ_o - angle between the magnetic axis and a radial vector for the point at which the magnetic field line defining the sides of the emission regions connects to the neutron star surface, (refer to Figures (2.1) and (2.7)).

d - distance of neutron star from observer

$\tilde{\phi}_1$ - azimuthal angle of the observer in the (X_2, Y_2, Z_2) coordinate system of reference measured from the Y_2 axis (Figure (2.1))

θ_m - angle between the rotation and magnetic axes

θ_r - angle between the rotation axis and line-of-sight

θ_{off} - initial polar angle offset of magnetic axis of second emission region (Figure (2.2))

ϕ_{off} - initial azimuthal coordinate offset for magnetic axis of second emission region (Figure (2.2))

$\varphi_o^{(1)}$- lower integration limit of azimuthal angle for first emission region measured from the Y_2 axis

$\varphi_o^{(2)}$ - lower integration limit of azimuthal angle for second (offset) emission region measured from the Y_2 axis

$\varphi_L^{(1)}$ - upper integration limit of first emission region in the azimuthal direction measured from the Y_2 axis

$\varphi_L^{(2)}$ - upper integration limit of second emission region in the azimuthal direction measured from the Y_2 axis

$R_L^{(1)}$ - radial height of first emission region measured from $R_L = 0$ at the centre of the star.

$R_L^{(2)}$ - radial height of second emission region (from $R_L = 0$ at centre of star)

Φ_o - initial phase angle

Φ - phase angle

2.2.2 Total flux from emission regions

The total flux over the two emission regions is obtained by adding the flux for each individual emission region for a particular direction to the observer (θ_1, ϕ_1), relative to the magnetic axis of the neutron star,

$$F_T(\theta_1, \phi_1) = F_{(1)}(\theta_1, \phi_1) + F_{(2)}(\theta_1, \phi_1) \tag{2.2}$$

Following Leahy, 1991[8], the flux from the second emission region, $F_{(2)}(\theta_2, \phi_2)$,

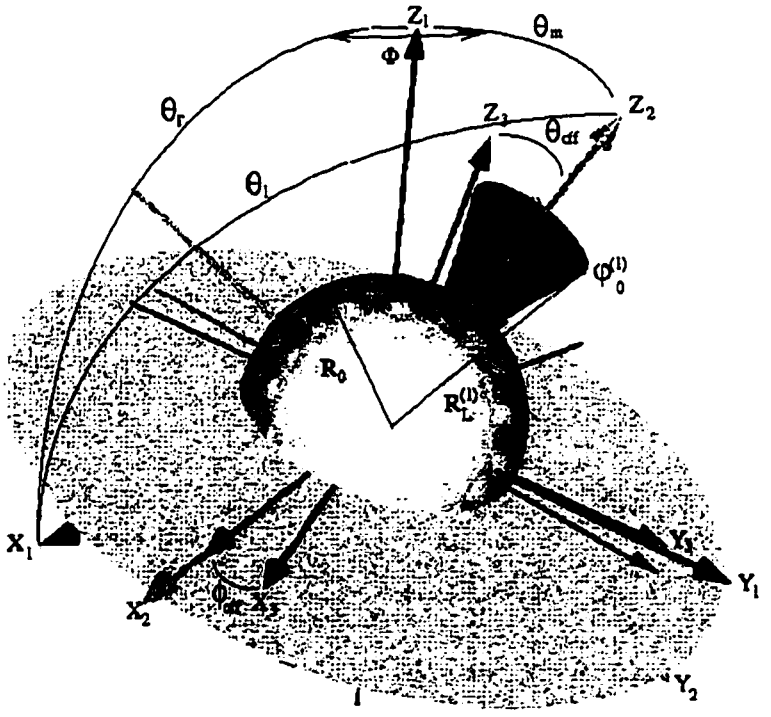

Figure 2.1: VRML visualization of the model showing parameter definitions. The (X_1, Y_1, Z_1) is the rotational system of coordinates with Z_1 as the rotation axis, (X_2, Y_2, Z_2) is the coordinate system referencing the magnetic axis Z_2, and (X_3, Y_3, Z_3) is the coordinate system referencing Z_3 as the axis of symmetry of the second emission region.

can be found from $F_{(1)}(\theta_1, \phi_1)$ since $F_{(2)}$ depends on ϕ_1 through the dependence of θ_2 on θ_1 and ϕ_1:

$$\begin{aligned} cos\theta_2 &= cos\theta_1 cos\theta'_{off} + sin\theta_1 sin\theta'_{off} cos\phi_1 \\ \theta'_{off} &= (\pi - \theta_{off}) \end{aligned} \tag{2.3}$$

where θ_2 is the angle between the second emission region and the direction to the observer. Definitions for the variables appearing in equation set (2.3) are shown in Figures (2.1) and (2.3). By virtue of equations (2.3), equation (2.2) can be re-stated as,

$$F_T(\theta_1, \phi_1) = F_{(1)}(\theta_1, \phi_1) + F_{(1)}(\theta_2) \tag{2.4}$$

where $\theta_2 = \theta_2(\theta_1, \phi_1)$.

2.2.3 Definitions of associated angles

The relationship between the observer's angle θ_1, and the pulse phase angle, $\Phi = 2\pi t/P + \Phi_o$ (in radians) (P is the period of neutron star rotation), is, from spherical trigonometry,

$$\cos\theta_1 = \cos\theta_m \cos\theta_r + \sin\theta_m \sin\theta_r \cos\Phi \tag{2.5}$$

θ_m is the angle between the rotation axis of the neutron star and the magnetic axis, θ_r is the angle between the rotation axis and the observer, and θ_1 is the angle between the magnetic axis and the observer. The pulse phase angle Φ is, therefore, the angle between the $\hat{e}_m$ and $\hat{e}_r$ directions as viewed from the rotational pole, where $\hat{e}_m$ and $\hat{e}_r$ are unit vectors oriented in the positive Y_1 and X_1 directions respectively (see

Figure 2.1). The above spherical-trigonometric relation between the angle θ_1, θ_m, and θ_r can also be expressed as,

$$\cos\theta_r = \cos\theta_1 \cos\theta_m + \sin\theta_1 \sin\theta_m \cos(\phi_1 - \phi_{off}) \tag{2.6}$$

where $(\phi_1 - \phi_{off})$ is the angle between the $\hat{e}_1$ and $\hat{e}_m$ directions, where $\hat{e}_1$ is a unit vector directed in the direction of θ_1. An offset angle ϕ_{off} is included in equation (2.6) for generality. For the purposes of this model, the inclusion of this offset angle applies only for the observer angle with respect to the second emission region. From this equation, then, the azimuthal angle ϕ_1, (Li, L., 1995)[29] of the observer, as measured from the X_2 axis in the clockwise direction is

$$\phi_1 = \phi_{off} + \cos^{-1}\left\{\frac{\cos\theta_r - \cos\theta_1 \cos\theta_m}{\sin\theta_1 \sin\theta_m}\right\} \tag{2.7}$$

For the numerical calculations, the angle ϕ_1 above (measured from the X_2 axis) is transformed to $\tilde{\phi}_1$ measured from the Y_2 axis through the equation,

$$\tilde{\phi}_1 = \phi_1 - \frac{\pi}{2} \tag{2.8}$$

Equation (2.7) can also be derived by considering successive Euler angle rotations from a system $S \rightarrow S'$, where S is the fixed reference system and S' rotates with the neutron star. For a clockwise rotation about the z' axis (the rotation axis of the neutron star) by an angle $-\Phi$, the rotation matrix is,

$$R_z(\Phi) = \begin{bmatrix} cos\Phi & -sin\Phi & 0 \\ sin\Phi & cos\Phi & 0 \\ 0 & 0 & 1 \end{bmatrix} \tag{2.9}$$

A successive, counterclockwise rotation about the y′ axis by an angle θ_m has the rotation matrix,

$$R_{y'}(\theta_m) = \begin{bmatrix} cos\theta_m & 0 & -sin\theta_m \\ 0 & 1 & 0 \\ sin\theta_m & 0 & cos\theta_m \end{bmatrix} \tag{2.10}$$

The product of these matrices representing the full coordinate transformation $S \rightarrow S'$ is then given by,

$$A(\theta_m, \Phi) = R_y(\theta_m) R_z(\Phi) \tag{2.11}$$

The reverse transformation from $S' \rightarrow S$ is,

$$\begin{bmatrix} x \\ y \\ z \end{bmatrix} = \tilde{R}_z(\Phi)\tilde{R}_y(\theta_m) \begin{bmatrix} x' \\ y' \\ z' \end{bmatrix} \tag{2.12}$$

The position vector for an observer in the S system is $\hat{p} = (rsin\theta_r, 0, rcos\theta_r)$, and in the S' system is $\hat{p'} = (rsin\theta_1 cos\phi_1, rsin\theta_1 sin\phi_1, rcos\theta_1)$. With the observer coordinates substituted into equation (2.12) above, we obtain the equation for z as,

$$\begin{aligned} z &= sin\theta_m x' + cos\theta_m z' \\ cos\theta_r &= sin\theta_m (sin\theta_1 cos\phi_1) + cos\theta_m (cos\theta_1) \end{aligned} \tag{2.13}$$

which is rearranged to give the previous result in equation (2.7) with the offset angle omitted.

$$cos\phi_1 = \left(\frac{cos\theta_r - cos\theta_1 cos\theta_m}{sin\theta_1 sin\theta_m} \right) \tag{2.14}$$

2.3 Equations for the Magnetic Field Lines

2.3.1 The dipole magnetic field

For a Newtonian (flat space) dipole field,

$$\vec{B} = B_r\hat{r} + B_\theta\hat{\theta} \tag{2.15}$$

where the components of the magnetic field are,

$$(B_r, B_\theta) = \left(\frac{2\mu\cos\theta}{r^3}, \frac{\mu\sin\theta}{r^3}\right) \tag{2.16}$$

where θ is measured clockwise from the magnetic axis. The angle σ, $0 \leq \sigma \leq \pi$ between the unit vector $\hat{s}$ along the magnetic field line and the unit radial vector $\hat{r}$ is given by the ratio of the components of the magnetic dipole field,

$$\tan\sigma = \left(\frac{B_\theta}{B_r}\right) = \left(\frac{rd\theta}{dr}\right) = \left(\frac{\frac{\mu\sin\theta}{r^3}}{\frac{2\mu\cos\theta}{r^3}}\right) = \left(\frac{\tan\theta}{2}\right) \tag{2.17}$$

The equation of the magnetic field line from the neutron star surface is then obtained by integrating over the radial coordinate from the neutron star radius R_o to position r, and θ_o to θ,

$$\int_{R_o}^{r} \frac{dr}{2r} = \int_{\theta_o}^{\theta} \frac{d\theta}{\tan\theta} \tag{2.18}$$

Integrating gives,

$$\frac{1}{2}\ln\left(\frac{r}{R_o}\right) = \ln(\sin\theta) - \ln(\sin\theta_o) \tag{2.19}$$

and,

$$\ln\left(\frac{r}{R_o}\right)^{1/2} = \ln\left(\frac{\sin\theta}{\sin\theta_o}\right) \tag{2.20}$$

giving the equation of the magnetic field lines as,

$$\left(\frac{\sin\theta}{\sin\theta_o}\right) = \sqrt{\frac{r}{R_o}} \tag{2.21}$$

$r = r(\theta)$ is then given by $r = \left(\frac{R_o \sin^2\theta}{\sin^2\theta_o}\right)$where R_o and θ_o are fixed parameters.

In terms of cylindrical polar coordinates $z = r\cos\theta$ and $y = r\sin\theta$ we have,

$$\vec{B} = \frac{R_o}{\sin^2\theta_o}\left((\sin^2\theta\cos\theta)\hat{k} + (\sin^3\theta)\hat{j}\right) \tag{2.22}$$

where the unit vector $\hat{k}$ is oriented along the axis of rotation (Z_1 axis).

2.3.2 A modified dipole magnetic field

(Wassermann and Shapiro, 1983)[22] and (Petterson, 1975)[26] have derived general relativistic solutions for vacuum magnetic multipoles in a Schwarzschild background. These solutions apply within the approximate regime where the mass-radius relation of the neutron star satisfies , $R > 2M$, and relativistic effects are important. They allow further accuracy in determinations of the surface magnetic field strength of neutron stars from cyclotron line observations, assuming that these lines are formed at its magnetic poles. Maxwell's equations in *curved* space-time are

$$F_{\mu\nu,\alpha} + F_{\alpha\mu,\nu} + F_{\nu\alpha,\mu} = 0, \tag{2.23}$$

$$\frac{\partial}{\partial x^\nu}\left(\sqrt{|g|}F^{\mu\nu}\right) = 4\pi\sqrt{|g|}j^\mu.$$

The field tensor $F_{\mu\nu}$ is related to the vector potential A_μ according to,

$$F_{\mu\nu} = \frac{\partial A_\mu}{\partial x^\nu} - \frac{\partial A_\nu}{\partial x^\mu} \tag{2.24}$$

For the case of static magnetic fields, in the absence of electric fields, we have $A_o = 0$, and $F_{\mu\nu}$ has only spatial components. With the magnetic field assumed to be azimuthally-symmetric, the 4-vector can be expressed as $\mathbf{A} = A^\phi(r,\theta)\mathbf{e}_\phi$. In addition, if one assumes that the electromagnetic fields are *small* enough to make changes in the geometry negligible, the Schwarzschild metric for $G = c = 1$, given by

$$(ds)^2 = -(1-2M/r)(dt)^2 + (1-2M/r)^{-1}(dr)^2 + r^2(d\theta^2 + sin^2\theta d\phi^2), \tag{2.25}$$

can be used. The metric tensor g is then,

$$g = \begin{bmatrix} -(1-2M/r) & 0 & 0 & 0 \\ 0 & (1-2M/r)^{-1} & 0 & 0 \\ 0 & 0 & r^2 & 0 \\ 0 & 0 & 0 & r^2 sin^2\theta \end{bmatrix} \tag{2.26}$$

The nonvanishing components of $F_{\mu\nu}$ are then found to be,

$$\begin{aligned} F^{\theta\phi} &= F^{\phi\theta} = g^{\theta\theta} g^{\phi\phi} A_{\phi,\theta} \\ &= r^{-4} sin^{-2}\theta A_{\phi,\theta}, \\ F^{r\phi} &= -F^{\phi r} = g^{rr} g^{\phi\phi} A_{\phi,r} \\ &= (1-2m/r) r^{-2} sin^{-2}\theta A_{\phi,r}. \end{aligned} \tag{2.27}$$

From the determinant of the metric tensor g, we have,

$$\sqrt{|g|} = r^2 sin\theta \tag{2.28}$$

and substituting equations (2.27) , (2.28) into the field equations (2.23), in the case of no sources (the 4-current vanishes), gives the result,

$$r^2\frac{\partial}{\partial r}\left(\left(1-\frac{2M}{r}\right)\frac{\partial A_\phi}{\partial r}\right)+sin\theta\frac{\partial}{\partial\theta}\left(\frac{1}{sin\theta}\frac{\partial A_\phi}{\partial\theta}\right)=0 \tag{2.29}$$

This partial-differential equation can be solved by expressing the 4-vector as a separate function of r and θ,

$$A_\phi = R(r)\Theta(\theta) \tag{2.30}$$

(Wassermann and Shapiro, 1983)[22] express the resulting separable solutions in terms of Legendre polynomials, and derive the component of the magnetic field for *curved* space as,

$$B_r = \frac{\mu\sin\theta}{r^3}\left[6x^3\sqrt{1-x^{-1}}\ln(1-x^{-1})+\frac{6x^2(1-\frac{x^{-1}}{2})}{\sqrt{1-x^{-1}}}\right] \tag{2.31}$$

and angular component,

$$B_\theta = \frac{2\mu\cos\theta}{r^3}\left[-3x^3\ln(1-x^{-1})-3x^2\left(1+\frac{x^{-1}}{2}\right)\right] \tag{2.32}$$

Here x is the scaled radius,

$$x = \left(\frac{r}{2M}\right) \tag{2.33}$$

This modification from the Newtonian case essentially causes the magnetic field strength to decrease *less* rapidly with radial distance r, and to decrease *less* rapidly with θ increasing along a magnetic field line. Figures (2.4) and (2.5), on pages 61 , 62 show the effect of this modification. As a consequence, the emission surface for a photon subtends a larger angle than in the Newtonian case. This effect may be responsible for contributing to broader peaks in the fan-beam component to the observed pulse profiles. In addition, (Brainerd and Mészáros, 1991)[30] have reduced

the above expression which involves analytic functions, to a series approximation given as

$$B_\theta = \frac{\mu \sin\theta}{r^3}\sqrt{1-\frac{R_s}{r}}b_\theta \equiv \frac{\mu \sin\theta}{r^3}\sqrt{1-\frac{R_s}{r}}\left[\sum_{i=0}^{\infty}\frac{3(i+1)}{i+3}\left(\frac{R_s}{r}\right)^i\right] \tag{2.34}$$

and

$$B_r = \frac{2\mu \cos\theta}{r^3}b_r \equiv \frac{2\mu \cos\theta}{r^3}\left[\sum_{i=0}^{\infty}\frac{3}{i+3}\left(\frac{R_s}{r}\right)^i\right] \tag{2.35}$$

R_s is the Schwarzschild radius,

$$R_s = \left(\frac{2GM}{c^2}\right) \tag{2.36}$$

At large r, $x = r/2M \gg 1$, and the modified dipole equations, (2.34), (2.35), reduce to the *flat* space result for a magnetic dipole,

$$B_\theta \approx \frac{\mu sin\theta}{r^3} \tag{2.37}$$

$$B_r \approx \frac{2\mu cos\theta}{r^3} \tag{2.38}$$

The equation for the magnetic field lines originating from the surface of the neutron star is derived as follows,

$$\tan\sigma = \left(\frac{rd\theta}{dr}\right) = \left(\frac{B_\theta}{B_r}\right) = \sqrt{1-\frac{R_s}{r}}\left(\frac{b_\theta}{2b_r}\right)\tan\theta, \tag{2.39}$$

where σ is the angle between the unit vectors, $\hat{r}$ and $\hat{s}$, as defined for the *flat* space model shown in Figure (2.7). Integrating the above expression, gives

$$\int_{\theta_o}^{\theta}\frac{d\theta}{\tan\theta} = \int_{R_o}^{r}\frac{1}{r}\sqrt{1-\frac{R_s}{r}}\left(\frac{b_\theta}{2b_r}\right)dr \tag{2.40}$$

and solving from the stellar surface to a point (r, θ)

$$\ln(\sin\theta) - \ln(\sin\theta_o) = \int_{R_o}^{r} \frac{1}{r}\sqrt{1 - \frac{R_s}{r}}\left(\frac{b_\theta}{2b_r}\right) dr \tag{2.41}$$

this leads to,

$$\left(\frac{\sin\theta}{\sin\theta_o}\right) = \sqrt{\frac{r}{R_o}} \exp\left[\frac{1}{2}\int_{R_o}^{r} g(r')r'^{-1}dr'\right] \tag{2.42}$$

where,

$$g(r') = \left(\frac{b_\theta}{b_r} - 1\right) \tag{2.43}$$

and taken to first order in $\left(\frac{R_s}{r}\right)$ is,

$$\left(\frac{\sin\theta}{\sin\theta_o}\right) = \sqrt{\frac{r}{R_o}}\left[1 + \frac{3R_s}{8R_o}\left(1 - \frac{R_o}{r}\right)\right] \tag{2.44}$$

It is important to test whether this equation is one to one, so that each point on the magnetic field line corresponds to a specific r and is not counted more than once in the determination of the emission region flux. This equation can be solved as a quadratic in r

$$(a + 2ab - ab^2)r^2 + (2ab^2R_o - 2abR_o - 1)r - ab^2R_o^2 = 0 \tag{2.45}$$

where a is a function of θ,

$$a \equiv \left(\frac{\sin^2\theta_o}{R_o\sin^2\theta}\right) \tag{2.46}$$

and b is a constant,

$$b \equiv \left(\frac{3R_s}{8R_o}\right) \tag{2.47}$$

Since the above equation is two-valued in r, one is forced to use $\theta = \theta(r)$ in defining the emission region. Therefore, for the flux calculation, the integrand must be in terms of r in referring to points on the emission surface.

2.4 Equations for Magnetic Field Strength

For *flat* space, the ratio of the magnetic field strength, $B(r,\theta)$, to the stellar magnetic field strength, $B_o(R_o,\theta_o)$ is

$$\left\{\frac{B(r,\theta)}{B_o}\right\} = \left(\frac{R_o}{r}\right)^3 \sqrt{\frac{3\cos^2\theta + 1}{3\cos^2\theta_o + 1}} \tag{2.48}$$

and substituting $\theta = \theta(r)$ into this equation gives,

$$\left\{\frac{B(r,\theta)}{B_o}\right\} = \left(\frac{R_o}{r}\right)^3 \sqrt{\frac{4 - 3\left(\frac{r}{R_o}\sin^2\theta_o\right)}{4 - 3\sin^2\theta_o}} \tag{2.49}$$

and for *curved* space is,

$$\left\{\frac{B(r,\theta)}{B_o}\right\} = \left(\frac{R_o}{r}\right)^3 \sqrt{\frac{b_\theta^2\left(1 - \frac{R_s}{r}\right)\sin^2\theta + 4b_r^2\cos^2\theta}{b_{\theta_o}^2\left(1 - \frac{R_s}{R_o}\right)\sin^2\theta_o + 4b_{R_o}^2\cos^2\theta_o}} \tag{2.50}$$

whereby one can again replace θ in terms of R_o, θ_o and r.

2.4.1 (Model A) - The *Flat* Space Model

Flux integral - single emission region

Integrating the spectral flux over frequency ω gives

$$F_{(1)} = \int F_{(1)\omega} d\omega \tag{2.51}$$

where $F_{(1)}$ is the flux from the first emission region. Substituting the expression for the solid-angle, for *flat space* we have,

$$\begin{aligned} F_{(1)\omega} &= \frac{\sin\theta_o}{d^2} \int_S I_\omega(\theta')(\hat{p}\cdot\hat{n}_s) r \sin\theta ds d\varphi, \\ &= \frac{\sin\theta_o}{d^2} \int_S I_\omega(\theta')(\hat{p}\cdot\hat{n}_s) r \sin\theta \sqrt{1 + r^2\left(\frac{\tan\theta}{2r}\right)^2}\, dr d\varphi \end{aligned} \tag{2.52}$$

The dot product term $(\hat{p}\cdot\hat{n}_s)$, where $\hat{p}$ and $\hat{n}_s$ are the unit vectors in the direction of the observer and normal to the emission region surface respectively, must now be written in terms of model angles. For a given point (r,θ,φ), on the magnetic field line, the angle between the unit radial vector $\hat{r}$ and the unit vector tangent to the field point $\hat{s}$ is the angle σ. One can re-orient the unit vector normal $\widehat{n_s}$, normal to the emission region surface S, into a unit normal vector $\widehat{n_k}$, that is perpendicular to the magnetic axis or $\hat{k}$ direction. Taking a slice at constant $z = r\cos\theta$ through the emission region yields a circle in the x-y plane with radius $\rho = r\sin\theta$ (see Figure 2.6). Thus, the equation for the radial vector for such a circle is given by,

$$\overrightarrow{\rho} = (-r\sin\theta\sin\varphi)\hat{i} + (r\sin\theta\cos\varphi)\hat{j} \tag{2.53}$$

The unit vector in the direction of $\overrightarrow{\rho}$ and parallel to the circular slice is

$$\hat{n}_k = \frac{(-\rho\sin\varphi)\hat{i} + (\rho\cos\varphi)\hat{j}}{\rho} = (-\sin\varphi)\hat{i} + (\cos\varphi)\hat{j} \tag{2.54}$$

and $\hat{n}_k \rightarrow \widehat{n_s}$ involves a rotation by an angle $(\theta+\sigma)$ in the Z_1 direction, so that the un-normalized unit vector $\widetilde{n_s} = \widehat{n_k} + \tan(\theta+\sigma)\hat{k}$, and when normalized is,

$$\widehat{n_s} = \frac{\widetilde{n_s}}{|\widetilde{n_s}|} = \left\{ \frac{-\sin\varphi\hat{i} + \cos\varphi\hat{j} + \tan(\theta+\sigma)\hat{k}}{\sqrt{(-\sin\varphi)^2 + (\cos\varphi)^2 + (\tan(\theta+\sigma))^2}} \right\}, \tag{2.55}$$

$$= \left\{ \frac{-\sin\varphi\hat{i} + \cos\varphi\hat{j} + \tan(\theta+\sigma)\hat{k}}{\sqrt{1 + (\tan(\theta+\sigma))^2}} \right\} \tag{2.56}$$

so that we have for the unit vector normal to the emitting surface S,

$$\widehat{n_s} = \left\{ \frac{-\sin\varphi\hat{i} + \cos\varphi\hat{j} + \tan(\theta+\sigma)\hat{k}}{\sec(\theta+\sigma)} \right\} \tag{2.57}$$

The propagation unit vector $\hat{p}$ is oriented in the z-y plane at an angle θ' with respect to $\widehat{n_s}$ and is,

$$\hat{p} = \cos\theta_1\hat{k} + \sin\theta_1\cos\phi_1\hat{j} - \sin\theta_1\sin\phi_1\hat{i}. \tag{2.58}$$

where θ_1 and ϕ_1 arise because the signal is assumed to propagate toward the observer. The dot product term is then,

$$(\hat{p}\cdot\widehat{n_s}) = \cos\theta' = \left\{ \frac{\sin\theta_1(\cos\phi_1\cos\varphi + \sin\phi_1\sin\varphi) + \cos\theta_1\tan(\theta+\sigma)}{\sec(\theta+\sigma)} \right\} \tag{2.59}$$

or similarly,

$$\cos\theta' = \cos\theta_1\cos(\theta+\sigma+\frac{\pi}{2}) + \sin\theta_1\sin\phi_1\sin(\theta+\sigma+\frac{\pi}{2})\sin\varphi, + \sin\theta_1\cos\phi_1\sin(\theta+\sigma+\frac{\pi}{2})\cos\varphi \tag{2.60}$$

This result is then substituted into the flux integral expression, and for the case of *flat* space, $\sin\theta$ can be replaced by $\sqrt{\frac{r}{R_o}}\sin\theta_o$ giving,

$$F_{(1)\omega} = \left(\frac{\sin\theta_o}{d^2}\right)\int_S I_\omega(\theta')(\hat{p}\cdot\widehat{n_s})r\sqrt{\frac{r}{R_o}}\sqrt{1+r^2\left(\frac{\tan\theta}{2r}\right)^2}\,dr d\varphi \tag{2.61}$$

which reduces to,

$$F_{(1)\omega} = \left(\frac{\sin\theta_o}{d^2}\right)\int_S I_\omega(\theta')\,(\hat{p}\cdot\widehat{n_s})\sqrt{\frac{r^3}{R_o}\left(1+\left(\frac{\tan\theta}{2}\right)^2\right)}\,dr d\varphi \tag{2.62}$$

A similar expression can be found for *curved* space, where the relevant equation for f' is used. The integrand above must now be written in terms of only the integration variables r and φ and model parameters. Using the trigonometric relation, $\csc^2\theta - \cot^2\theta = 1$, one finds

$$\tan^2\theta = \left(\frac{\sin^2\theta}{1-\sin^2\theta}\right) = \left(\frac{\frac{r}{R_o}\sin^2\theta_o}{1-\frac{r}{R_o}\sin^2\theta_o}\right) = \left(\frac{-\sin^2\theta_o}{\sin^2\theta_o - \frac{R_o}{r}}\right) \tag{2.63}$$

And with,

$$\tan(\theta+\sigma) = \left(\frac{\tan\theta+\tan\sigma}{1-\tan\theta\tan\sigma}\right) \tag{2.64}$$

Substituting for $\tan\sigma = \left(\frac{\tan\theta}{2}\right)$ and the result for $\tan^2\theta$ gives,

$$\tan(\theta+\sigma) = \left(\frac{3\tan\theta}{2-\tan^2\theta}\right) = \left\{\frac{3r\sin^2\theta_o\sqrt{\sin^2\theta_o - \frac{R_o}{r}}}{2R_o - 3r\sin^2\theta_o}\right\} \tag{2.65}$$

Local emission angle equation

From spherical-trigonometry, the equation for θ' in terms of coordinate angles θ_a, φ_a of the radial direction $\hat{r}$, and θ_b, φ_b of $\hat{n}_s$, is

$$\cos\theta' = \cos\theta_a \cos\theta_b + \sin\theta_a \sin\theta_b \cos(\varphi_a - \varphi_b) \tag{2.66}$$

When there is no gravitational light bending, these angles are $\theta_a = \theta_1$, and $\varphi_a = \phi_1$, while $\theta_b = \left(\theta + \sigma + \frac{\pi}{2}\right)$, and $\varphi_b = \varphi$. The angles (θ_1, ϕ_1) represent the direction to the observer. So the above equation takes the form,

$$\cos\theta' = \cos\theta_1 \cos\left(\theta + \sigma + \frac{\pi}{2}\right) + \sin\theta_1 \sin\left(\theta + \sigma + \frac{\pi}{2}\right) \cos(\phi_1 - \varphi) \tag{2.67}$$

2.4.2 (Model B) - The *Curved* Space Model

Flux integral - single emission region

In *curved* space the flux integral is,

$$F_{(1)\omega} = \frac{\sin\theta_o}{d^2} \int_S I_\omega(\theta')(\hat{p}\cdot\hat{n}_s) r \sin\theta \sqrt{1 + r^2 \left(\frac{\tan\sigma}{2}\right)^2}\, dr d\varphi \tag{2.68}$$

and substituting for $\tan\sigma$ one obtains,

$$F_{(1)\omega} = \frac{\sin\theta_o}{d^2} \int_S I_\omega(\theta')(\hat{p}\cdot\hat{n}_s) r \sin\theta \sqrt{1 + r^2 \left(\frac{\tan\theta}{2r}\sqrt{1 - \frac{R_s}{r}}\left(\frac{b_\theta}{b_r}\right)\right)^2}\, dr d\varphi \tag{2.69}$$

From the equation for the magnetic field lines (to first-order), we define

$$\eta \equiv \sin\theta = \sin\theta_o \sqrt{\frac{r}{R_o}} \left[1 + \frac{3R_s}{8R_o}\left(1 - \frac{R_o}{r}\right)\right] \tag{2.70}$$

with,

$$\Rightarrow \cos\theta = \sqrt{1-\eta^2} \tag{2.71}$$

and thus,

$$\tan\theta = \frac{\eta}{\sqrt{1-\eta^2}} \tag{2.72}$$

so that $r\sin\theta$ yields,

$$r\sin\theta = \sin\theta_o \frac{r^{3/2}}{\sqrt{R_o}}\left[1+\frac{3R_s}{8R_o}\left(1-\frac{R_o}{r}\right)\right] \tag{2.73}$$

As with the case of no gravitational light-bending, we must express $\tan\theta$, and $\tan(\theta+\sigma)$ in the integrand in terms of the integration variables,

$$\tan^2\theta = \left(\frac{\sin^2\theta}{1-\sin^2\theta}\right) = \left(\frac{\eta^2}{1-\eta^2}\right) \tag{2.74}$$

and recalling that,

$$\tan\sigma = \sqrt{1-\frac{R_s}{r}}\left(\frac{b_\theta}{b_r}\right)\frac{\tan\theta}{2} \tag{2.75}$$

we have,

$$\begin{aligned}\tan(\theta+\sigma) &= \left(\frac{\tan\theta+\tan\sigma}{1-\tan\theta\tan\sigma}\right) = \left[\frac{\tan\theta\left(1+\sqrt{1-\frac{R_s}{r}}\left\{\frac{b_\theta}{2b_r}\right\}\right)}{1-\tan^2\theta\sqrt{1-\frac{R_s}{r}}\left(\frac{b_\theta}{2b_r}\right)}\right] \\ &= \left[\frac{\frac{\eta}{\sqrt{1-\eta^2}}\left(1+\sqrt{1-\frac{R_s}{r}}\left\{\frac{b_\theta}{2b_r}\right\}\right)}{1-\frac{\eta^2}{1-\eta^2}\sqrt{1-\frac{R_s}{r}}\left(\frac{b_\theta}{2b_r}\right)}\right]\end{aligned} \tag{2.76}$$

Thus, the flux expression with gravitational light-bending considered is,

$$F_{(1)\omega} = \frac{\sin\theta_o}{d^2} \int_S I_\omega(\theta')(\hat{p}\cdot\hat{n}_s)\eta\sqrt{1+r^2\left(\frac{\tan\sigma}{2}\right)^2}\,dr d\varphi \tag{2.77}$$

The intensity I_ω appearing in the above equation can be written in terms of a photon distribution function, $f(\mathbf{r},\mathbf{n},\nu,t)d\Omega d\nu$, which is the number of photons per unit volume at a location $\mathbf{r}$ and time t, with frequencies within the range $(\nu,\nu+d\nu)$, propagating at velocity c in the direction $\mathbf{n}$ into a solid angle, $d\Omega$. The frequency-specific intensity is related to f as,

$$I_\nu = \nu^3 f, \qquad \omega = 2\pi\nu \tag{2.78}$$

The propagation of radiation near a neutron star can then be described in terms of f within a relativistic transport equation. (Riffert, 1986)[17] has derived a co-moving radiation transfer equation, specializing the result to the case of spherically-symmetric flow around a central mass. They consider a slowly rotating mass for which the gravitational effects from external flow are negligible (Riffert and Mészáros, 1988)[18].

Local emission angle equation

If one defines an angle K' between the radial vector pointing toward an emission point $Q = Q(r_o,\theta_o,\varphi)$, and the radial vector point to the observer; since $\hat{r}$, and $\widehat{n_s}$ have the same φ component, $\theta' = \left(\frac{\pi}{2} - K'\right)$, or

$$\sin\theta' = \sin\left(\frac{\pi}{2} - K'\right) = \cos K' \tag{2.79}$$

The angle between the radial vector pointing $\hat{r}$ toward the emission point Q and the local propagation vector $\hat{p}$ is defined as K'. The angle K' is,

$$K'(r, r_o, \mu_o) = b \int_{r_o}^{r} \left[x^2 - b^2\left(1 - \frac{1}{x}\right)\right]^{-\frac{1}{2}} \frac{dx}{x} + Q'(r_o, \mu_o) \tag{2.80}$$

where,

$$Q'(r_o, \mu_o) = \begin{cases} 0 & \mu_o \geq 0 \\ 2b \int_{r_m}^{r_o} \left[x^2 - b^2\left(1 - \frac{1}{x}\right)\right]^{-\frac{1}{2}} \frac{dx}{x} & \mu_o < 0 \end{cases} \tag{2.81}$$

Here,

$$\mu_o = \cos\theta' \tag{2.82}$$

Where θ' is the local emission angle with respect to the normal, at the emission point $Q = Q(r_o, \theta_o, \varphi)$. The definitions of r_o, b, r_m, are given in the next section. If one takes the observer to be infinitely far away from the neutron star, denoted now by an indicative subscript, the equation for $K' \rightarrow K'_\infty$ is,

$$K'_\infty(r \rightarrow \infty, r_o, \mu_o) = b \int_{r_o}^{\infty} \left[x^2 - b^2\left(1 - \frac{1}{x}\right)\right]^{-\frac{1}{2}} \frac{dx}{x} + Q'(r_o, \mu_o) \tag{2.83}$$

Here K'_∞ is the angle between the radial vector passing through the emission point, $Q(r_o, \theta_o, \varphi_o)$, and the unit vector pointing in the direction to the observer at infinity. Using spherical trigonometry, we have,

$$cosK'_\infty = cos\theta_1 cos\theta + sin\theta_1 sin\theta cos(\varphi - \phi_1) \tag{2.84}$$

The evaluation of K'_∞ can be handled for two separate cases; for $Q' = 0$, and $Q' \neq 0$. For the case $Q' = 0$, Leahy *et al.*, (1995)[9] has derived a linear, light-bending equation for K'_∞ given as,

$$cosK'_\infty = acosK' + b \tag{2.85}$$

where the value of a and b for $r_o = \left(\frac{R_o}{R_*}\right)$, and $(2 \leq r_o \leq 5)$ is,

$$\begin{aligned} a &= \frac{2.653}{r_o^2} + \frac{0.381}{r_o} + 1.068, \\ b &= \frac{-2.944}{r_o^2} + \frac{0.232}{r_o} - 0.087 \end{aligned} \tag{2.86}$$

Combining equations (2.79) and (2.85), the relation between K'_∞ to the local emission angle θ' for the case of $Q' = 0$ is,

$$cosK'_\infty = asin\theta' + b \tag{2.87}$$

For the case $Q' \neq 0$, the integrals in equations (2.80) and (2.81) must be numerically evaluated. For given values of θ_1, ϕ_1, $\theta = \theta(r, \theta_o, R_o)$, and φ, the value of K'_∞ can be calculated using equation (2.84). Using this value of K'_∞, the value of θ' lying in the integrand of equations (2.80) and (2.81), must be determined. A routine to handle this task could pass through the range, $-\frac{\pi}{2} \leq \theta' \leq \frac{\pi}{2}$, calculating the value of K'_∞ from the integral expression. When K'_∞ calculated from the integral corresponds to its calculation from the spherical-angle equation (2.84), the subsequent value θ' is then selected.

2.5 Shadowing Effects

Shadowing by the neutron star of each emission region, based on the angle to the observer is taken into account in the calculation of the overall flux. Shadowing of one emission region on the other is also considered. The generalized conditions for when shadowing should be taken into account are further complicated in the case of gravitational-light bending.

2.5.1 Shadowing of emission regions by the neutron star

Equations for model A *(flat-space)*

For the case of *shadowing by the neutron star of the second emission region*, the polar angle to the observer is,

$$\theta_1 \prec \left(\frac{\pi}{2} + \theta_{off}\right) \tag{2.88}$$

where the observer lies at (d, θ_1, ϕ_1) (refer to Figure 2.9). All points (r, θ, φ) of the emission region at a distance $\rho = r\sin\theta$ from the magnetic axis, and satisfying the condition,

$$\rho_2^2 = (r\sin(\theta - (\pi - \theta_2)))^2 \leq R_o^2 \qquad 0 \leq \theta_2 \leq \pi \tag{2.89}$$

are to be omitted from the flux calculation of $F_{(2)}(\theta_1, \phi_1)$. Similarly, for *shadowing of the first emission region*, the polar angle to the observer must lie within the range,

$$\theta_1 \succ \left(\frac{\pi}{2} - \theta_{off}\right) \tag{2.90}$$

and all points (r, θ, φ) which satisfy,

$$\rho_1^2 = (r\sin(\theta - (\pi - \theta_1)))^2 \leq R_o^2 \qquad 0 \leq \theta_1 \leq \pi \tag{2.91}$$

again are to be omitted from the flux calculation of $F_{(1)}(\theta_1, \phi_1)$.

Equations for model B *(curved space)*

In the ϕ_1 plane of the observer, r_m is the minimum distance of approach to the neutron star of a photon ray. Points that are shadowed in the gravitational light-

bending case satisfy,

$$r_m^2 \leq R_o^2 \tag{2.92}$$

where r_m is given in equation, (2.97). The impact parameter b is given as,

$$\frac{r}{A}\left(1-\mu^2\right)^{1/2} = b = \frac{r_o}{A_o}\left(1-\mu_o^2\right)^{1/2} \tag{2.93}$$

and,

$$A_o = \left(1-\frac{1}{r_o}\right)^{1/2} \tag{2.94}$$

It is important to note that r_o is the magnitude of the radius vector at the emission point from the center of the neutron star (in Schwarzschild units), or,

$$r_o = \left(\frac{r}{R_s}\right) = r\left(\frac{c^2}{2GM}\right) \tag{2.95}$$

The lower limit on the integral for $Q'(r_o, \mu_o)$ is found from solving the cubic equation,

$$r_m^3 - b^2(r_m - 1) = 0 \tag{2.96}$$

The radial distance r_m represents the minimum distance, or closest approach of a photon, measured from the center of the neutron star. This distance is meaningful in the case where a photon has been emitted above the star, and travels in a downward direction. The largest root of the above cubic equation is taken, since it is at the largest possible r that the orbit of a light ray will experience a 'turning point' in its motion, and as given by (Wald, 1984)[41] as,

$$r_m = \frac{2b}{\sqrt{3}} \cos\left[\frac{1}{3}\cos^{-1}\left(-\frac{3^{3/2}M}{b}\right)\right] \tag{2.97}$$

and M is the mass of the neutron star. A solution for positive r_m exists only for,

$$b^2 > \frac{27}{4} \tag{2.98}$$

$$\mu_o > -\sqrt{1 - \frac{27}{4r_o^2}\left(1 - \frac{1}{r_o}\right)} \tag{2.99}$$

If this condition is not satisfied then the photon will fall back onto the neutron star surface, and will not reach the observer. In the calculation of the flux we must account for emitted radiation that falls upon the neutron star and is not observed. With $\mu = 0$, and $r = R_o$, equation (2.93) gives,

$$\mu_{R_o} = -\sqrt{1 - \frac{R_o^2}{r_o^2}\left(\frac{1 - \frac{1}{r_o}}{1 - \frac{1}{R_o}}\right)} \tag{2.100}$$

where R_o is the radius of the neutron star, and r_o is the radial coordinate at the point of emission, in Schwarzschild units. Thus, photons will not be observed whenever $\mu_o < \mu_{R_o}$.

2.5.2 Shadowing by the emission regions

In addition, for the path of photons which are strongly bent by gravitational light-bending, a photon emitted from a point $(r_o, \theta_o, \varphi_o)$ in the *ith* emission region may circle around the neutron star, hitting the same point for,

$$K'(R_L^{(i)}, r_o, \mu_o) = 2(\pi - \theta_o) \qquad r < R_L^{(i)} \tag{2.101}$$

These points must be discarded from the flux calculation. Also, the photon may circle and hit the same point, but within the other, *jth* emission region, so that,

$$K'(R_L^{(j)}, r_o, \mu_o) = (\pi - 2\theta_o) \qquad r < R_L^{(j)} \tag{2.102}$$

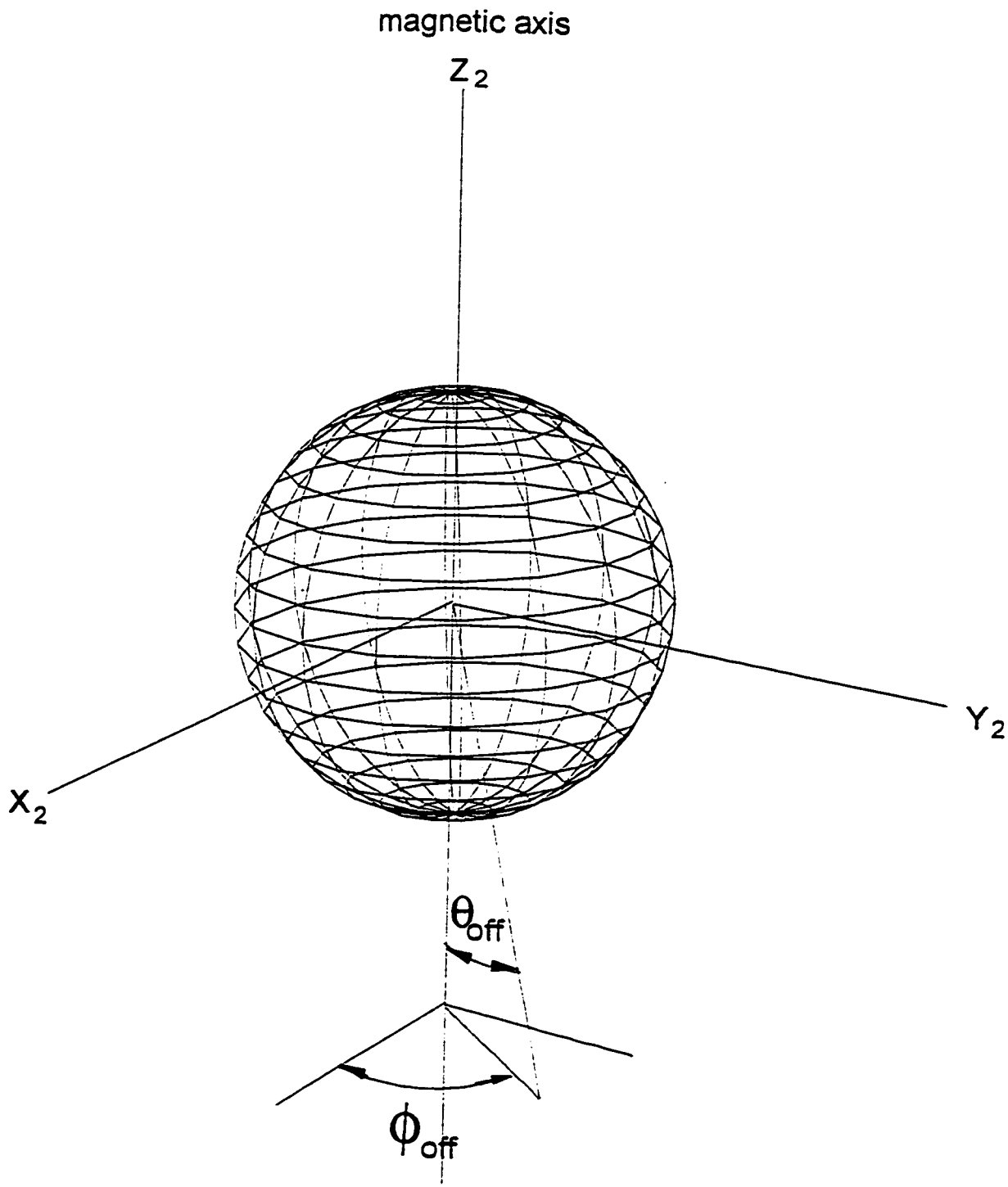

Figure 2.2: Definition of the offset angles. θ_{off} and ϕ_{off}.

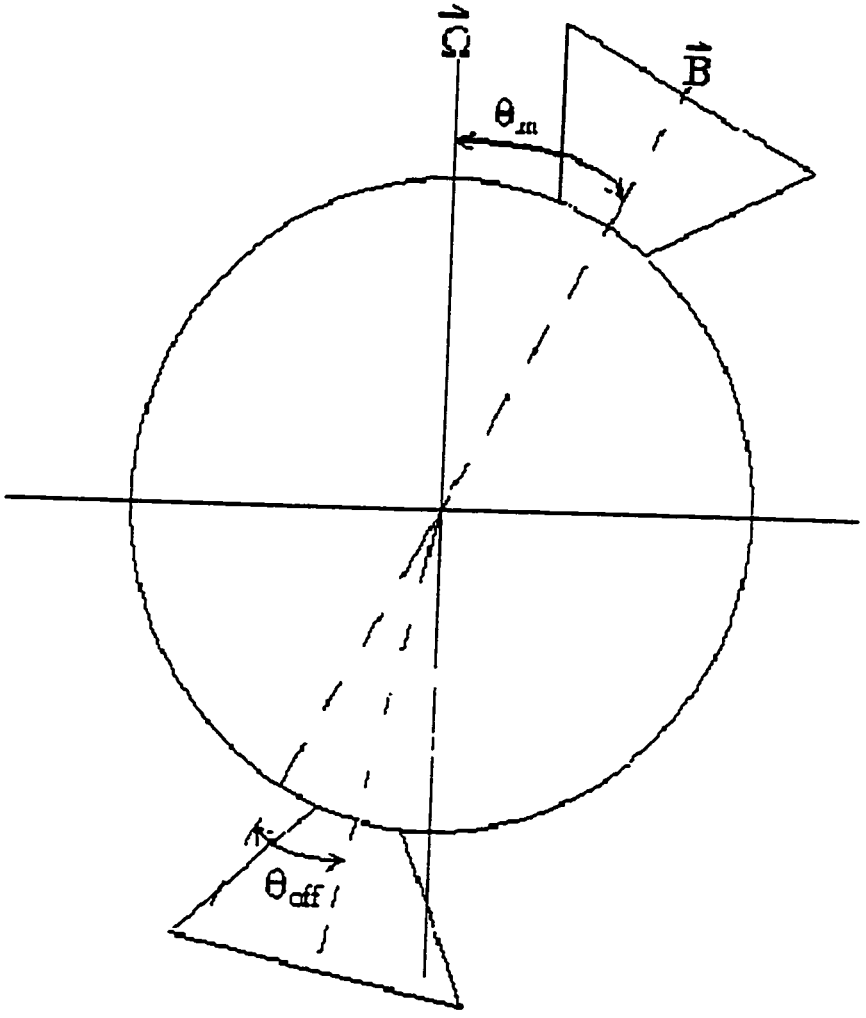

Figure 2.3: Diagram showing the definition of the offset angle for the location of the second emission region from the magnetic axis.

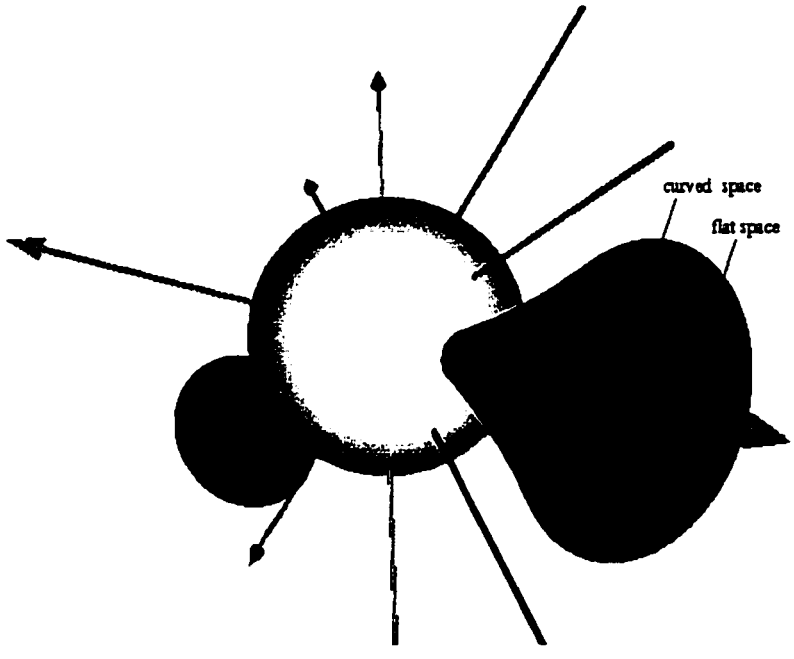

Figure 2.4: VRML visualization showing the emission surface variation due to the modified field geometry within a Schwarzschild metric.

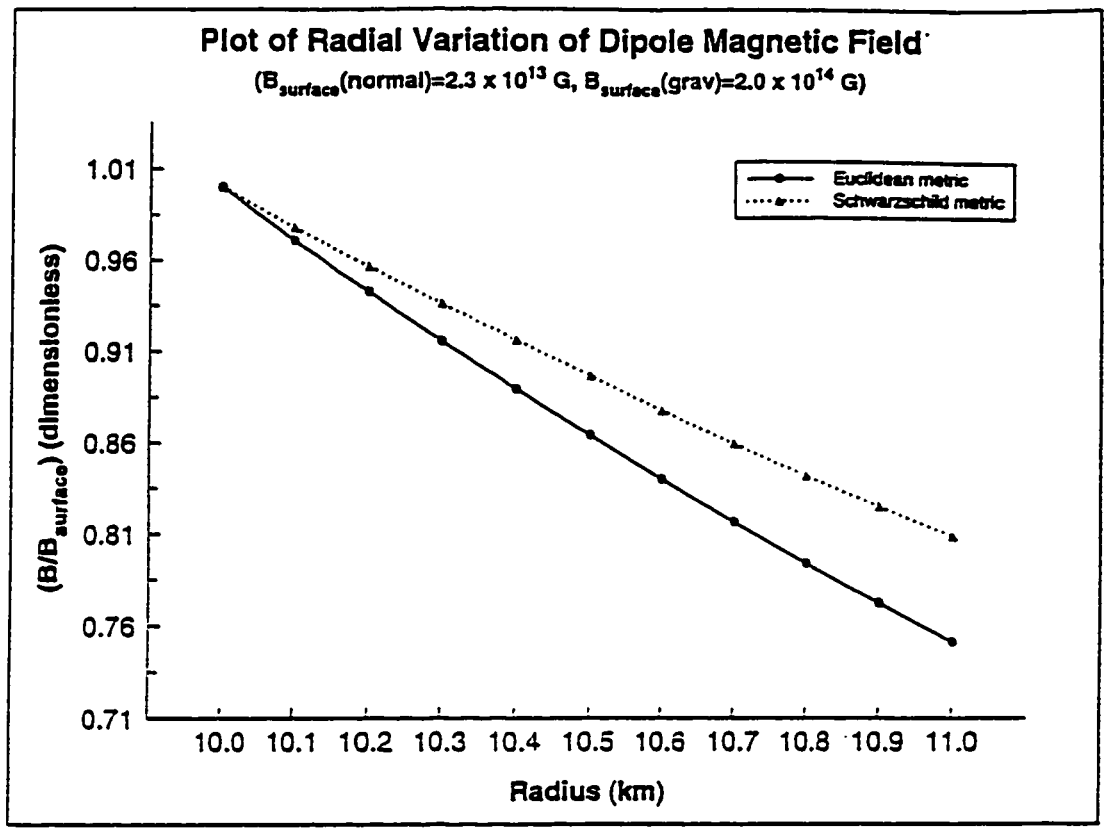

Figure 2.5: A comparison of the magnetic field strengths for the flat and curved space models.

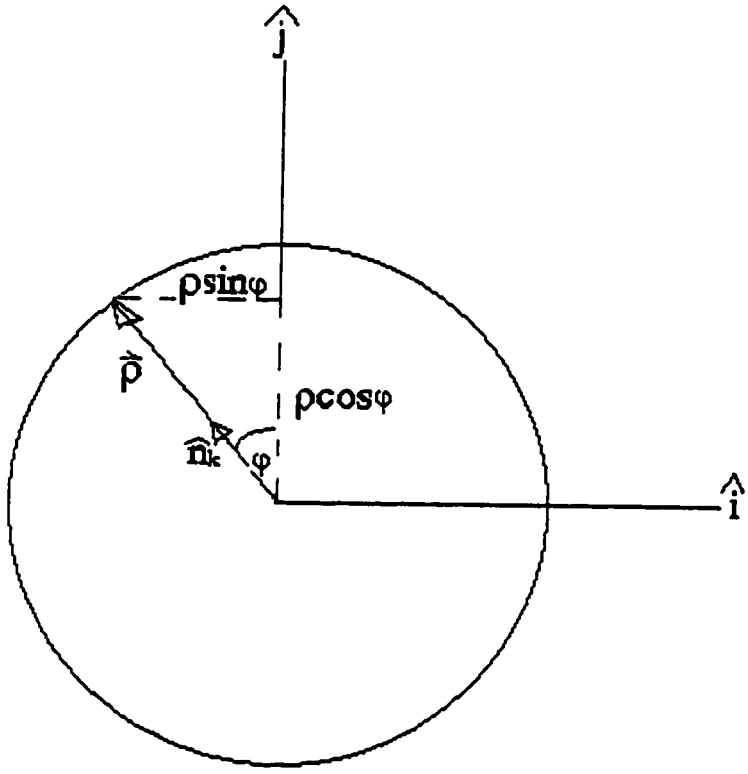

Figure 2.6: Diagram showing the definition of the vectors, $\vec{\rho}$, $\hat{n_k}$, and the angle φ.

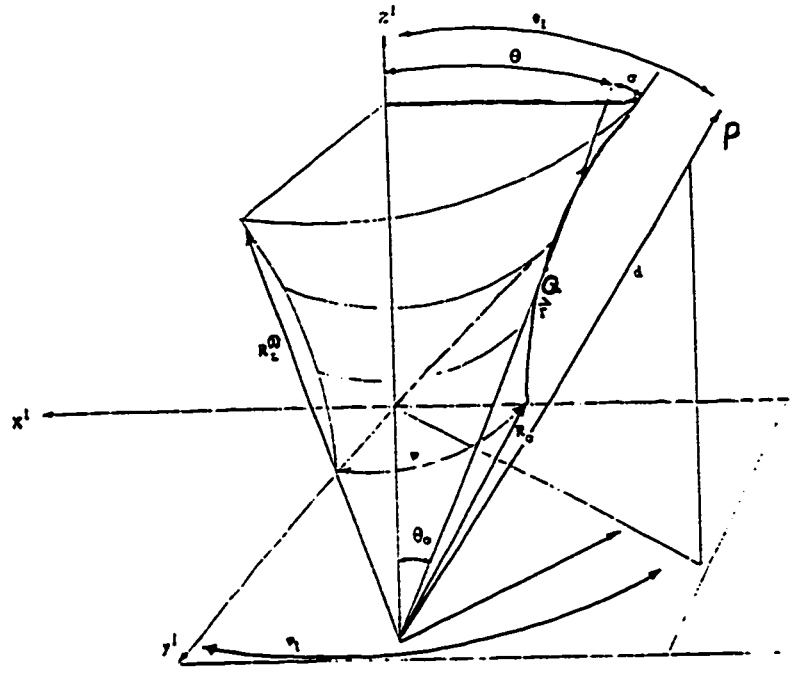

Figure 2.7: Schematic of model A, showing angle definitions used in describing emission from a point Q located on the surface of the emission region and travelling in a straight path towards a distant observer located at point P, a distance d from the centre of the neutron star.

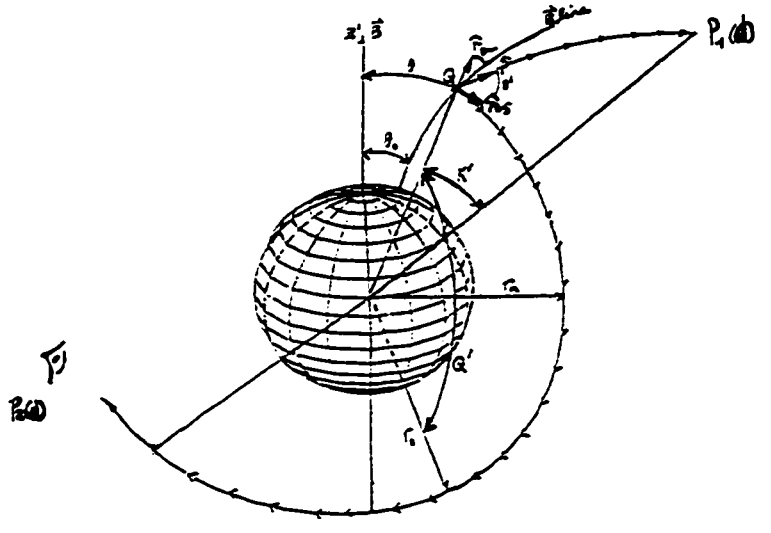

Figure 2.8: Schematic of model B, showing the gravitational light-bending of photon paths, and angle definitions.

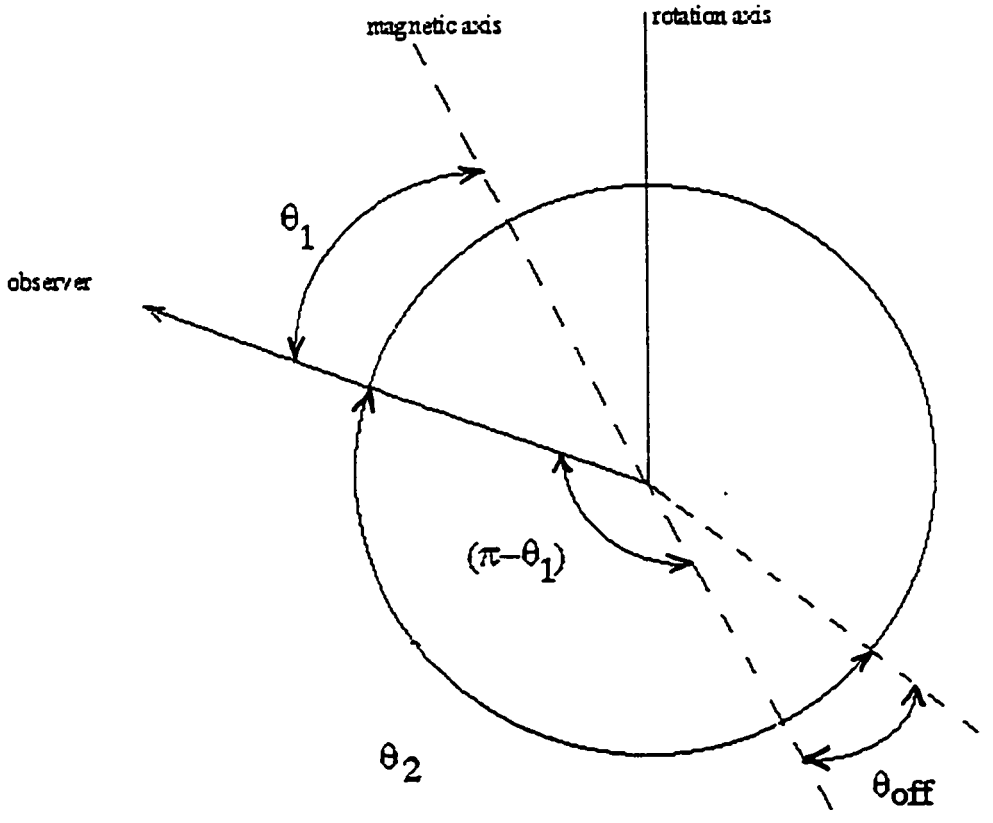

Figure 2.9: Diagram showing the angles used in the equations for shadowing of the neutron star on the emission regions.

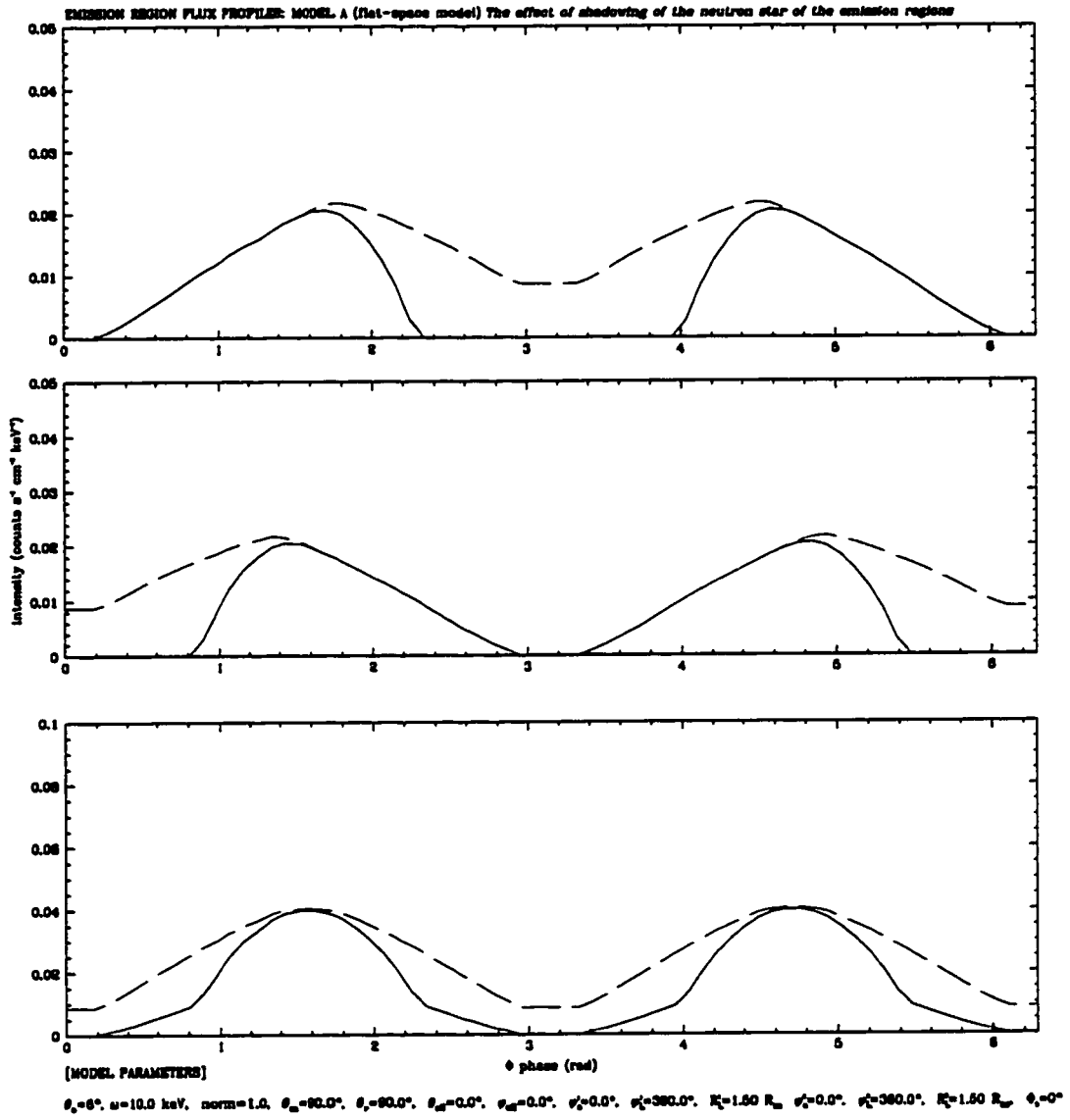

Figure 2.10: The effect shadowing of the emission regions by the neutron star. The solid line is the calculated intensity profile of emission seen by a distant observer with shadowing considered; the dashed line is the profile without shadowing.

Chapter 3

Numerical Calculations and Analysis

3.1 Evaluation of the Flux Integrals

The flux integrals for the *flat* space model were numerically evaluated using the IMSL[1] routine DQAND. This routine approximates an n-dimensional iterated integral in the form,

$$\int_{a_1}^{b_1} \cdots \int_{a_n}^{b_n} f(x_1, \cdots, x_n) dx_n \cdots dx_1 \tag{3.1}$$

Approximation is acheived by iterated applications of product Gauss formulas. An initial estimate of the integral is found using a two-point tensor product formula for each direction spanned by an integration variable. A new estimate is then calculated by doubling the number of points (reducing the step-size) in the i^{th} direction. If this new estimate does not change appreciably, the step-size is restored to its former value. This process of evaluation proceeds until a complete sweep over the limits of integration results in no increase in the number of sample points. A desired level of absolute and relative error necessary for convergence can be specified. The model code uses this routine in performing integration over the r and φ variables, for an initial set of the 16 geometrical parameters. Since the local emission intensity is both a function of angle and energy, energy-integrated theoretical pulse profiles require an additional integration over frequency ω. An overview of the sequence of equation evaluations used in evaluating the flux integrals is shown in Figures (3.1) and (3.2).

[1]Inter. Math. and Stat. Lib.

3.1.1 The physical basis of the model parameters

The Neutron Star Equation of State

Mass estimates of x-ray pulsars (Rappaport and Joss, 1981)[43] provide determinations for lower bounds on the maximum mass of stable neutron stars. In a recent study, (Li and Wang, 1995)[51], semi-empirical mass-radius (M-R) relations were calculated for four x-ray pulsars, namely, Cen $X-3$, 4U $1626-67$, Her $X-1$ and EXO $2030+375$, using observed data and a modified accretion torque model. These mass-radius relations relate to the exterior behaviour of a neutron star, depending on the nature of the plasma accretion flow onto the stellar surface and on the properties of emission from plasma just above the surface. The results of the study show, in particular, that the theoretical mass-radius relation for EXO $2030+375$ is consistent with a stiff equation of state, yielding mass and radius values near typical of neutron stars, ($1.2M_{\odot}$ and 14.5 km). These calculations support the hypothesis that neutron stars have mass $\sim$ $1.4M_{\odot}$ as might be expected from stellar evolution theory (Pines and Ventura, 1991)[25]. Figure (3.4) from (Li and Wang, 1995)[51] shows a comparison of the mass-radius relations of EXO $2030+375$. The three theoretical curves for the equation of state for neutron stars shown are the mean-field (MF), three-nucleon interaction (TNI), and the Reid+pion-condensate ($R+\pi$) states, see (Wassermann and Shapiro, 1983)[22] and references therein. The calculated M-R curve for EXO $2030+375$ shown as a solid line in Figure (3.4) is consistent with all three equations of state. Comparison of the fastness parameter values for the three equations of state with the value of 0.10 calculated from the 0.2 Hz QPO's detected

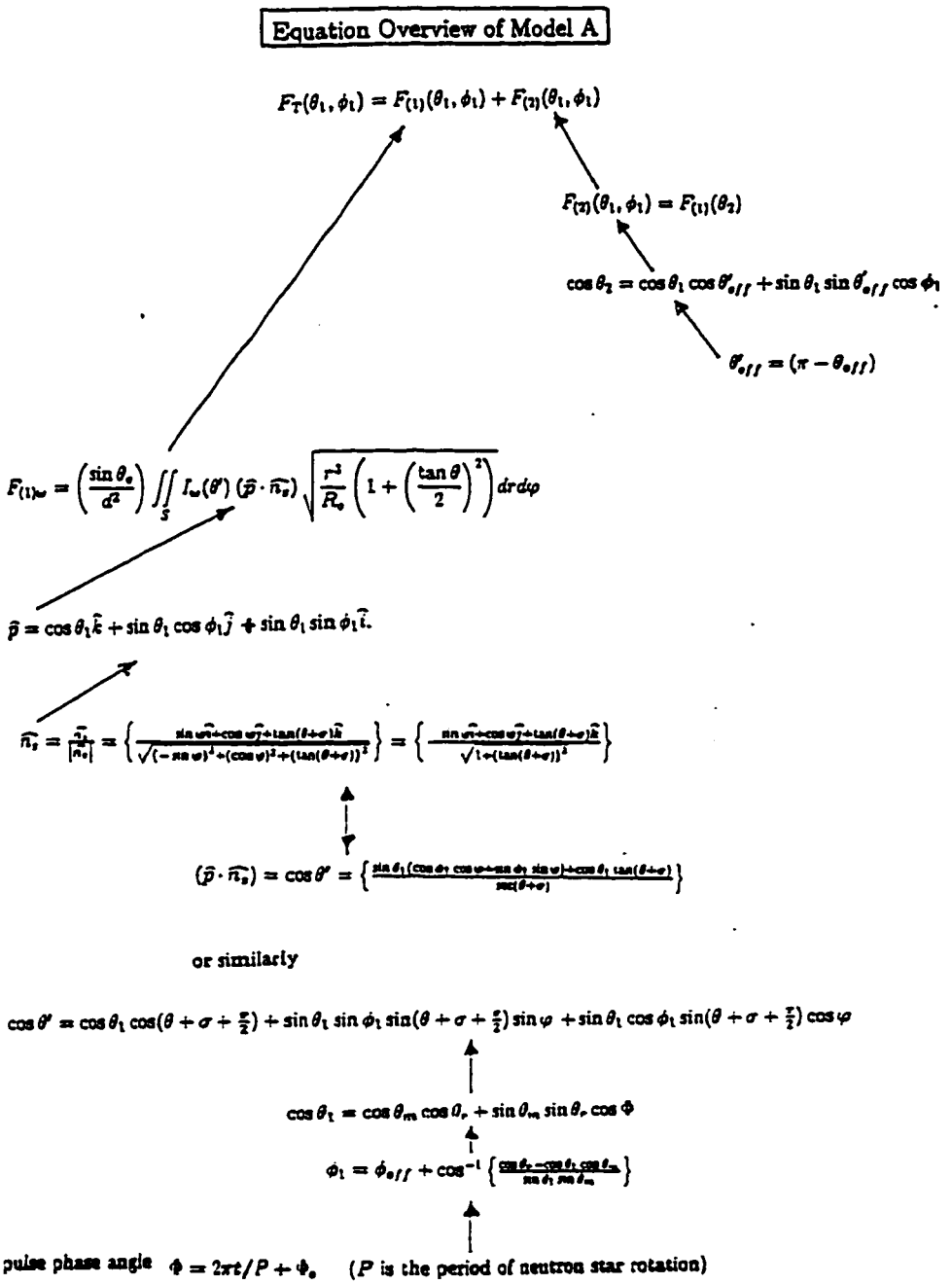

Figure 3.1: Equation overview of *flat* space model (A).

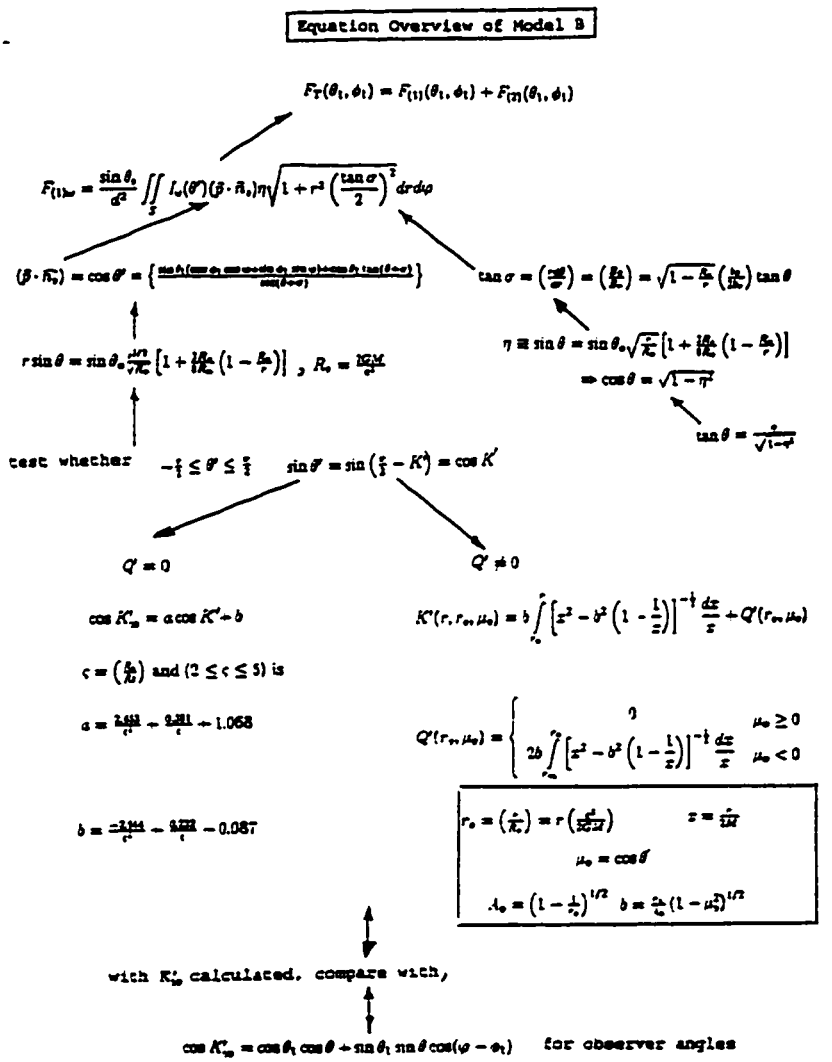

Figure 3.2: Equation overview of *curved* space model (B).

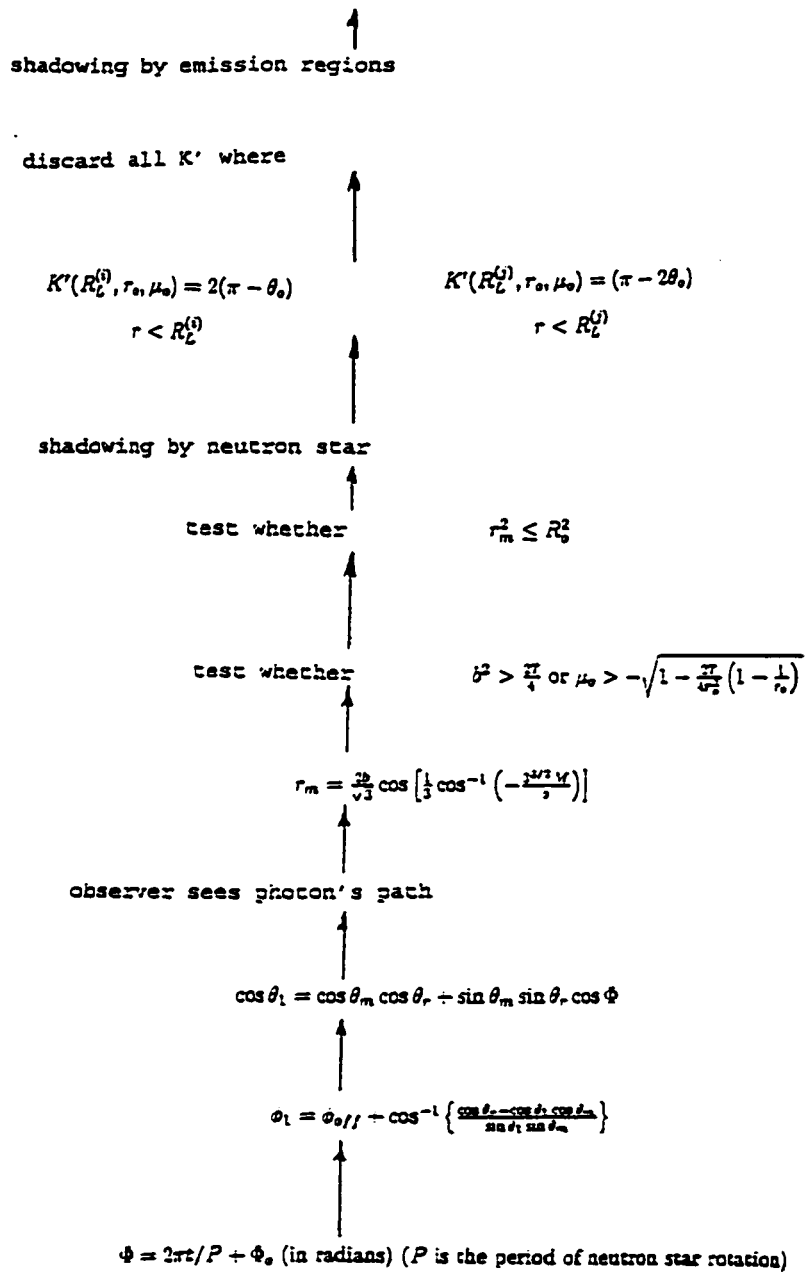

Figure 3.3: Equation overview of *curved* space model (B) continued.

during the outburst of EXO 2030 + 375 in 1985, however, add support to the stiff (MF) equation of state (Li and Wang, 1995)[51]. For the purposes of the emission model, however, the values of ($1.4M_{\odot}$ and 10.0 km) were used in all calculations, lying midway between the theoretical curves for the ($R + \pi$) and (TNI) equations of state for EXO 2030 + 375.

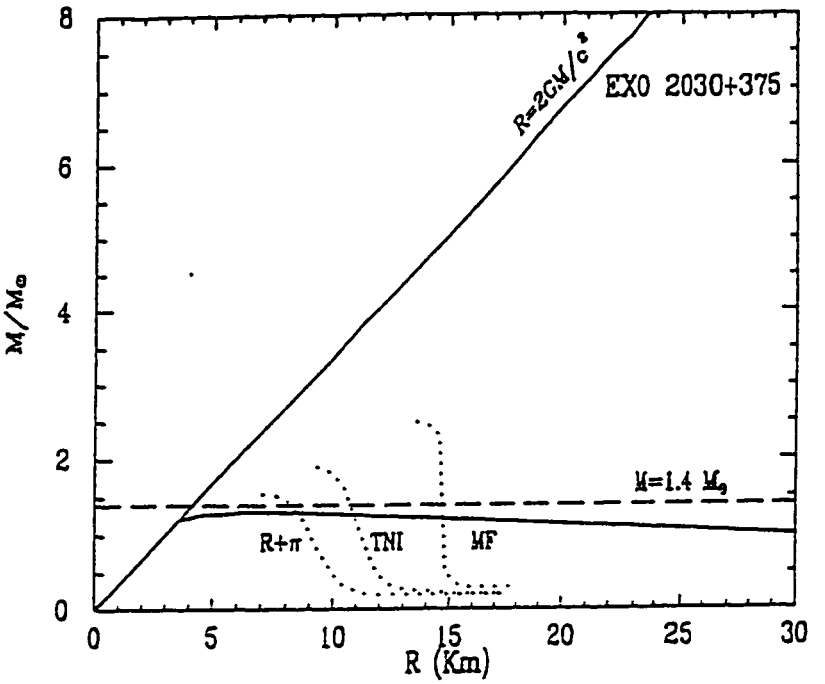

Figure 3.4: Comparison of the mass-radius relations of EXO 2030 + 375. Dotted curves are the M-R relations (interior) based on the theoretical $R + \pi$, TNI and MF equations of state of neutron stars. The solid curve is the calculated M-R curve for EXO 2030 + 375. The dashed line is the estimate of mass from x-ray and optical observations.

3.2 Test Cases

This section presents various test cases of the theoretical model, showing the effect of varying each of the model parameters. All the test case results have $\theta_o = 6°$, and completely filled emission regions of radial height $R_L^{(i)} = 1.5R_o$ from the centre of the neutron star, with no offset angles unless specified otherwise. The various profiles appearing in each figure are shown varying from a solid line to dashed lines, in sequence with the successive values of the parameter that is varying. The figures each display from top to bottom, the profile from the first emission region, the second emission region, and the total profile from both emission regions. Although the model parameters are not fully independent, knowledge of how each parameter can affect the profile of emission was used in finding suitable input parameter vectors for the fitting of the observed pulse profiles.

Cyclotron frequency, w_{cyc}

Figure (3.5) shows the effect of increasing the cyclotron frequency in the model. An increasing cyclotron frequency implies a higher magnetic field strength at the surface of the neutron star. A reduced number of points were chosen for the calculation of this profile which makes it less smooth. The asymmetric peaks in the top two graphs for the intensity seen by an observer arises from the dependence of the local emission intensity on angle and frequency as shown in Figure (1.9). The steep drop-off and rise in the peaks are due to shadowing (refer to Figure 2.10).

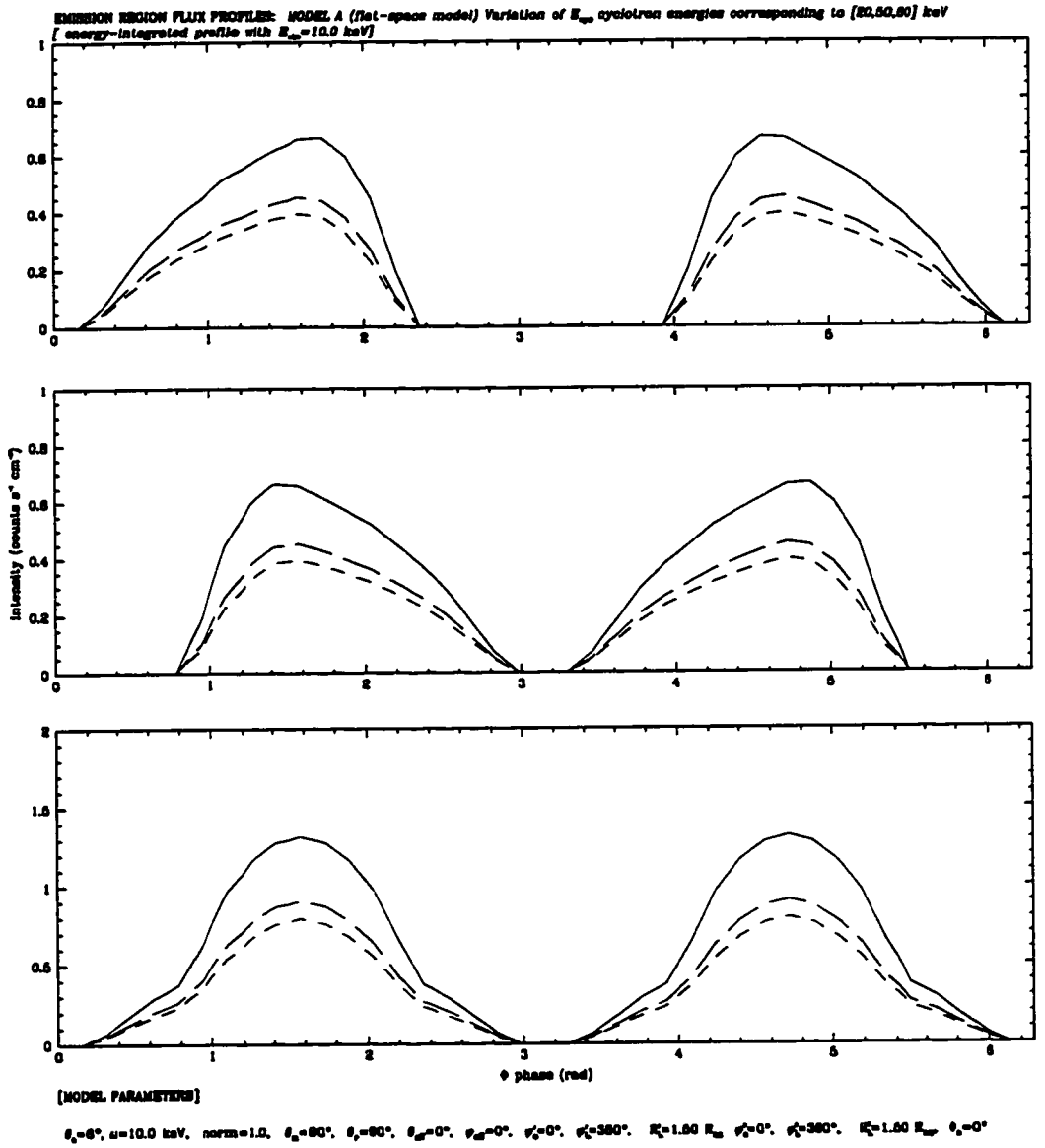

Figure 3.5: Variation of the cyclotron frequency at the neutron star surface for successive values (20, 50, 60) keV, E_{obs} = 10 keV. $I(\theta', \omega)$ is integrated over both angle and frequency in producing the profile.

Observed energy, E_{obs}

Variation of the observed energy for the model is shown in Figure (3.6). As E_{obs} varies as (6.0,10.0,20.0) keV, the peaks of the resulting emission profile become sharper and increase in magnitude slightly.

Opening angle θ_o

Figure (3.7) shows the effect of varying the opening angle θ_o, for two emission regions of equal height $R_L^{(i)} = 1.5R_o$, $i = (1, 2)$. The angle between the magnetic and rotation axes is chosen to be 90°. The observer angle, $\theta_r = 90°$, places the observer in a plane that bisects the emission regions about the magnetic axis symmetrically. As a result of the emission being directed from the sides of the emission regions; as the opening angle increases, the theoretical profile shows enlarging peaks which become less broad. As a result of the sides of each of the emission regions being shifted towards one another, a smaller angular range becomes available for the fan-beam emission.

Magnetic axis angle, θ_m

Variation of the magnetic axis angle in the model, θ_m=(0.0, 22.5, 45.0, 90.0)°. for an observer angle of $\theta_r = 90°$ are shown in Figure (3.8). As the magnetic angle decreases, more emission is shadowed by the neutron star and the intensity curve in Figure (3.8) flattens out. For $\theta_m = 0°$, the observer sees a constant line of emission due to the azimuthal symmetry of the completely-filled regions.

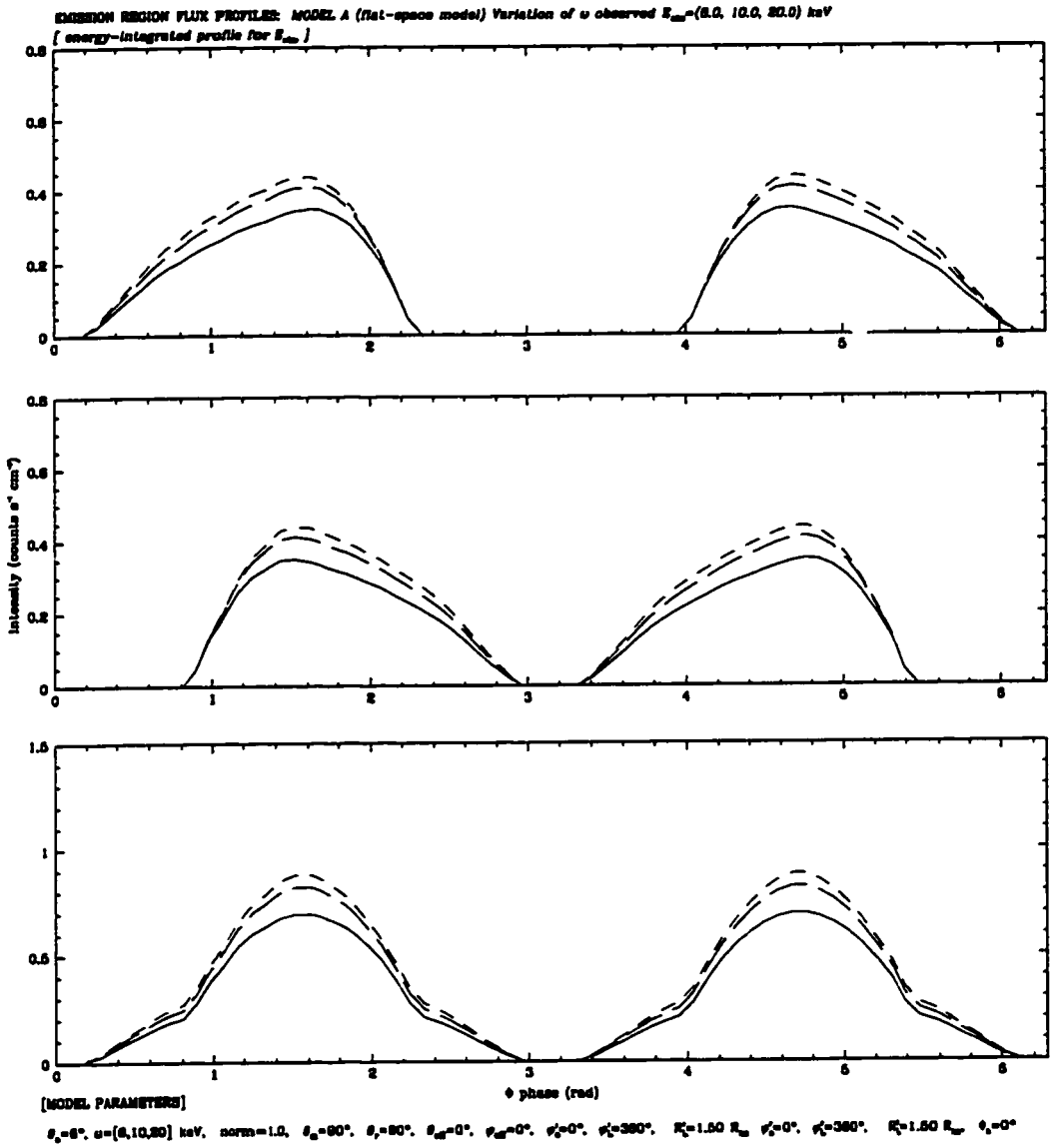

Figure 3.6: Variation of the observed energy, for values of E_{obs}=(6, 10, 20) keV, (energy-integrated profile).

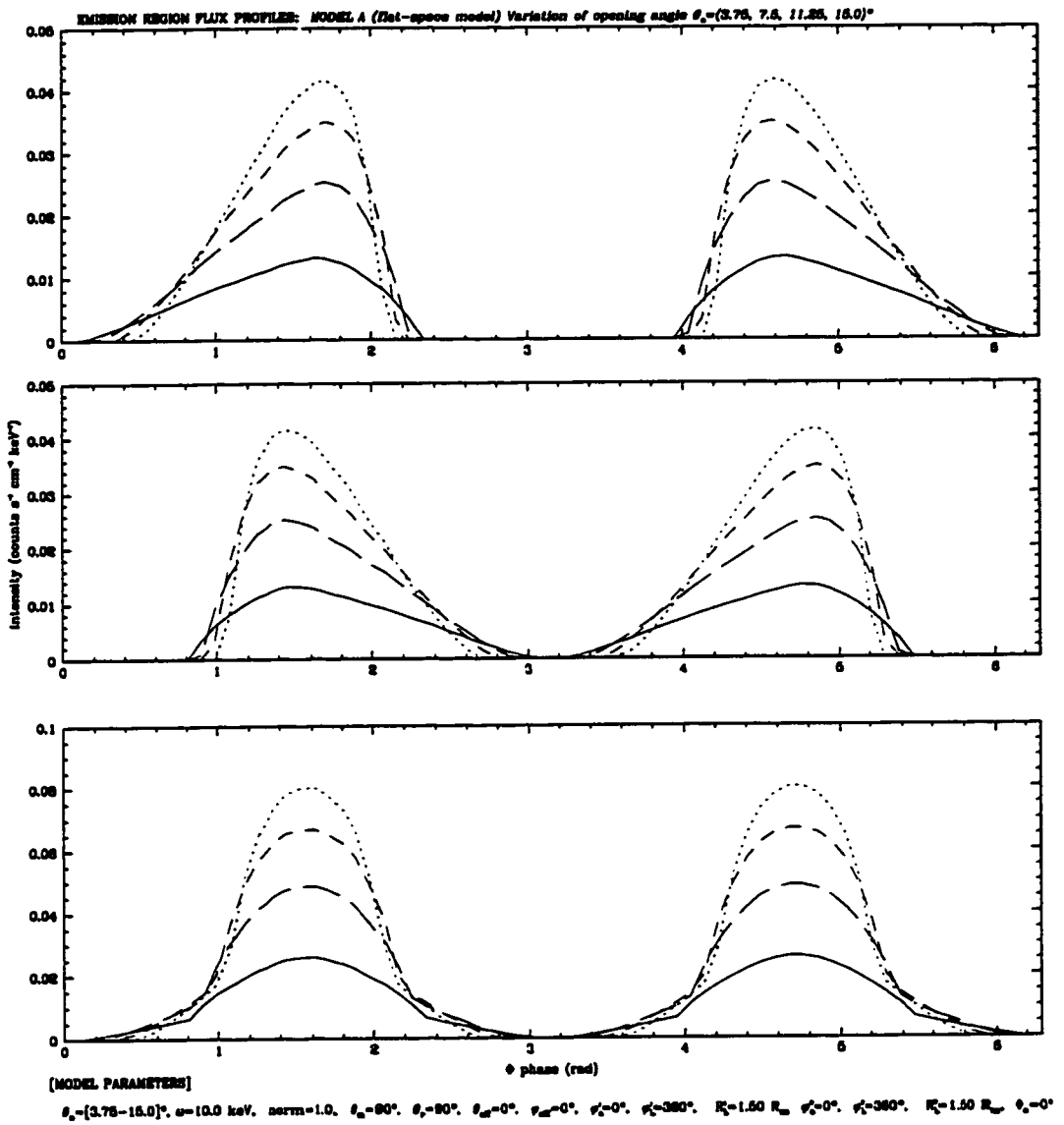

Figure 3.7: Variation of the emission region opening angle θ_o=(3.8, 7.5, 11.3, 15.0)°.

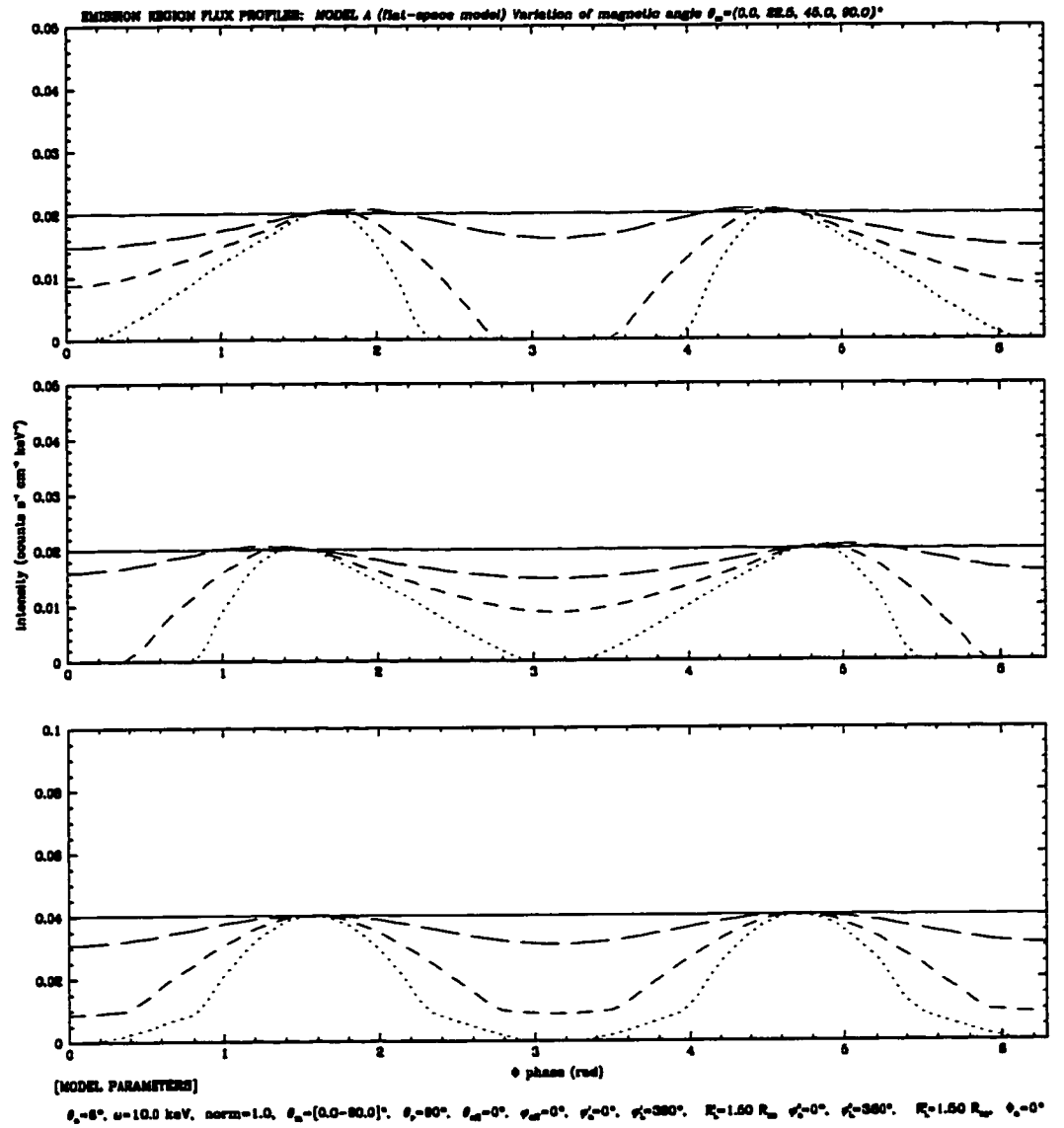

Figure 3.8: Variation of the magnetic axis angle, θ_m=(0.0, 22.5, 45.0, 90.0)°.

Observer angle, θ_r, θ_m constant

The observer angle was varied from $\theta_r = (20, 40, 60, 90)°$ at a constant magnetic axis angle of $\theta_m = 0°$ (magnetic and rotation axes are aligned), and the results are shown in Figure (3.9). In the middle graph of Figure (3.9), the $\theta_r = 20°$ and $\theta_r = 40°$ curves are absent due to shadowing by the neutron star. In every case of the observer angle, the profile is constant. As the observer angle increases, more of the emission from the sides of the emission region is seen. Figures (3.10) - (3.12), show the effect of varying the observer angle for different, constant magnetic axis angles. As the emission regions are tilted away from the rotation axis the constant profile seen when $\theta_m = 0°$ begins to show more feature. These model profiles are consistent with the results of Wang and Welter, (1981)[54] for a fan-beam, point-source flux distribution.

Polar offset angle, θ_{off}

Variation of the polar offset angle, θ_{off}, is shown in Figure (3.13). As the polar offset angle is increased, the second emission region tilts away from the magnetic axis, reducing the separation between the two emission regions. The fan-beam profile from the second emission region is shifted so that more emission is seen from its sides, at times when emission is not seen from the first emission region.

Azimuthal offset angle, φ_{off}

In order to test the variation of the azimuthal offset angle, the emission regions were taken to have the same radial heights R_L with zero polar offset angle, θ_{off}, but were partially-filled over an angular range of 90°. In this way, as the filled section is rotated around the azimuthal coordinate by an angle of φ_{off} (in the second emission

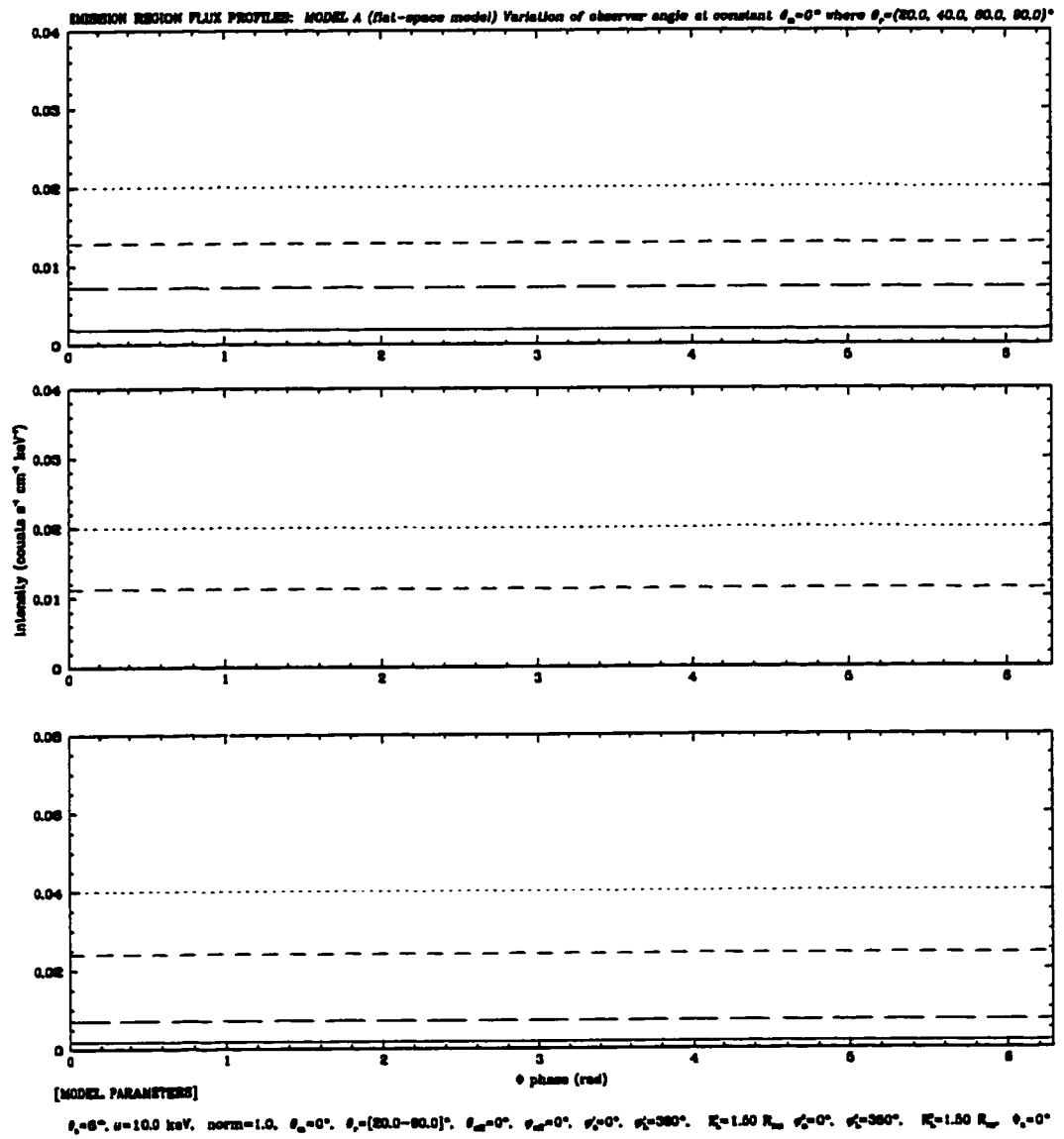

Figure 3.9: Variation of the observer angle $\theta_r = (20, 40, 60, 90)°$, at constant $\theta_m = 0°$.

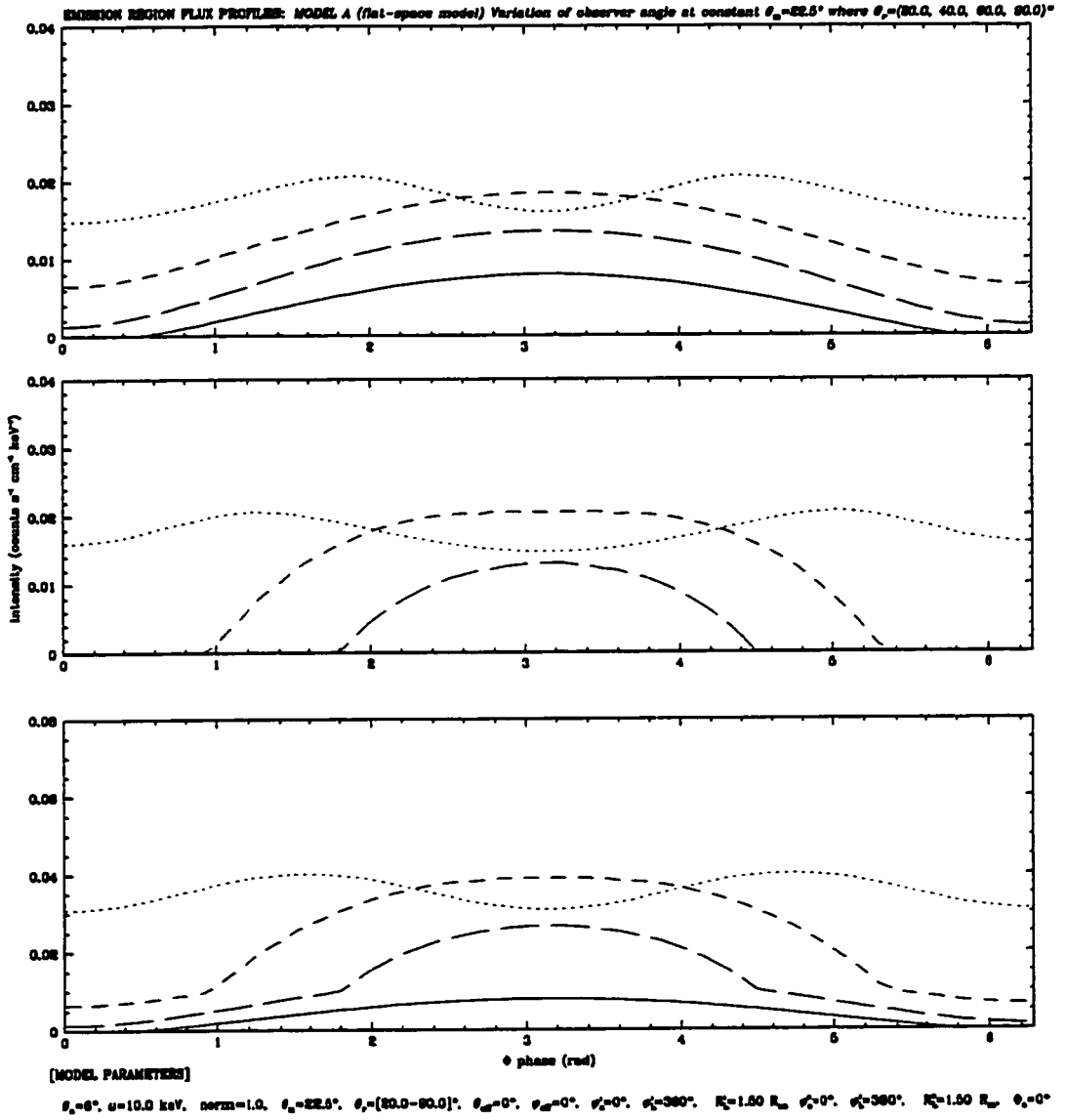

Figure 3.10: Variation of the observer angle, θ_r=(20, 40, 60, 90)° at constant θ_m=22.5°.

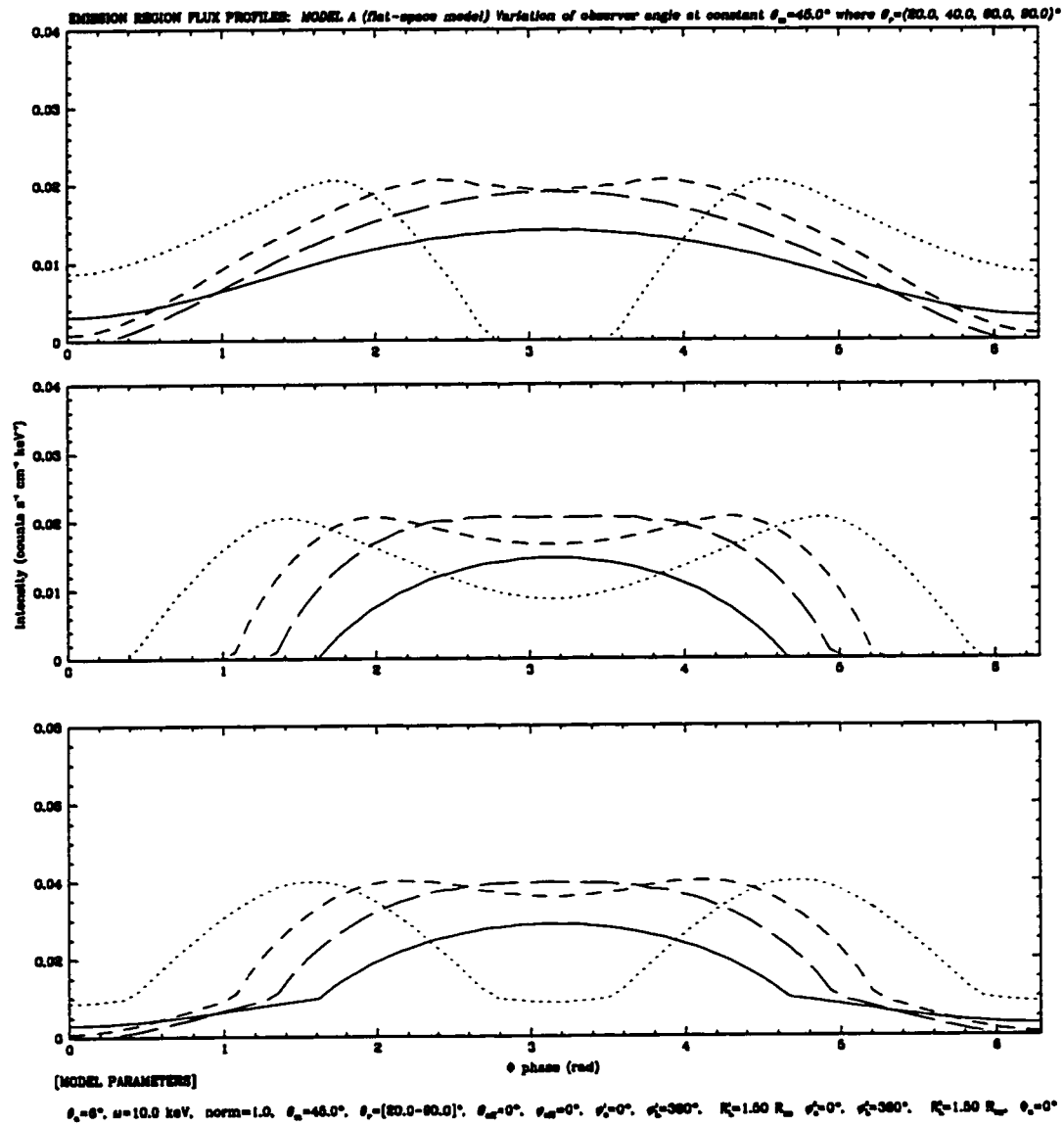

Figure 3.11: Variation of the observer angle, $\theta_r = (20, 40, 60, 90)°$ at constant $\theta_m = 45.0°$.

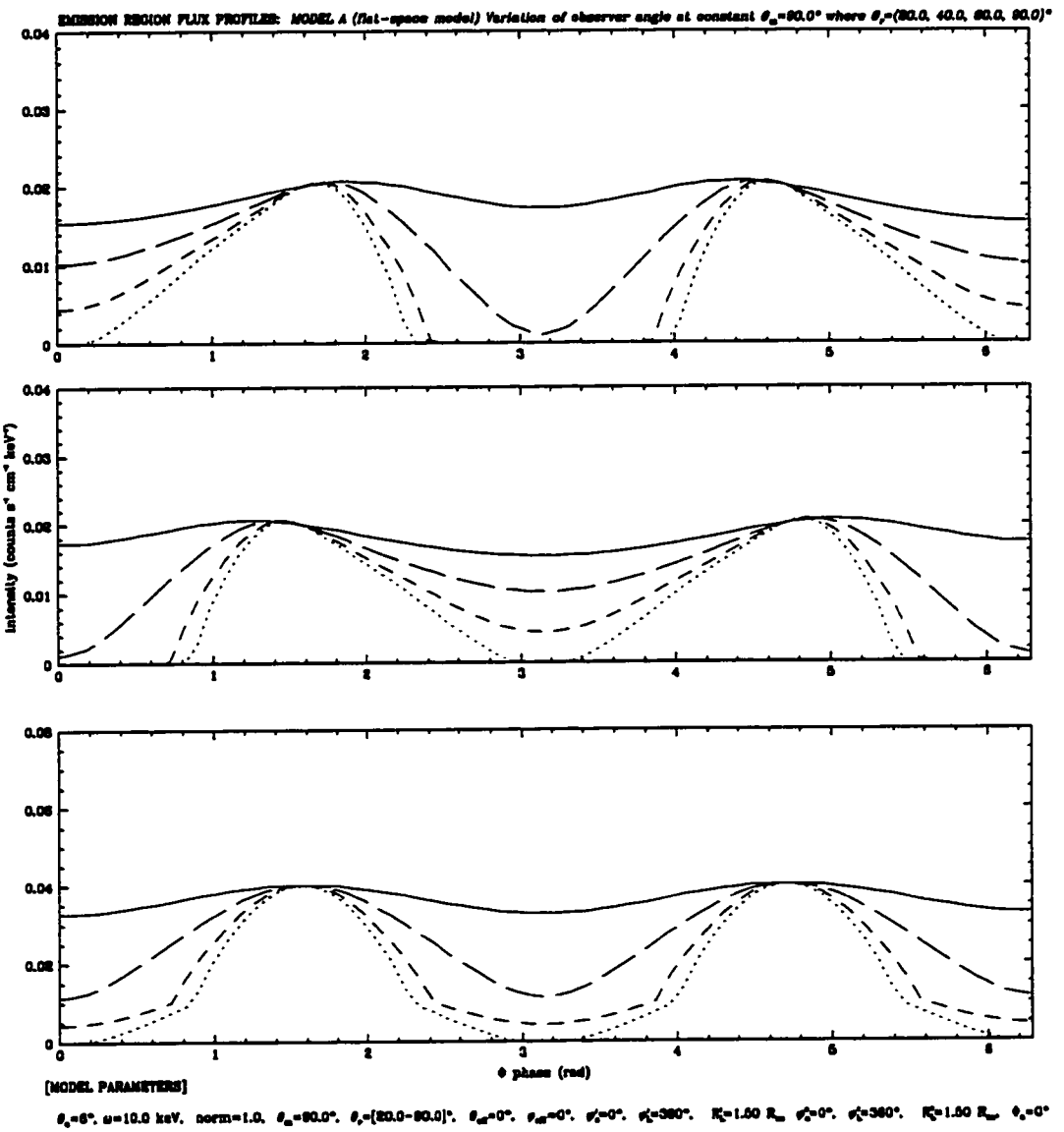

Figure 3.12: Variation of the observer angle, $\theta_r = (20, 40, 60, 90)°$ at constant $\theta_m = 90.0°$.

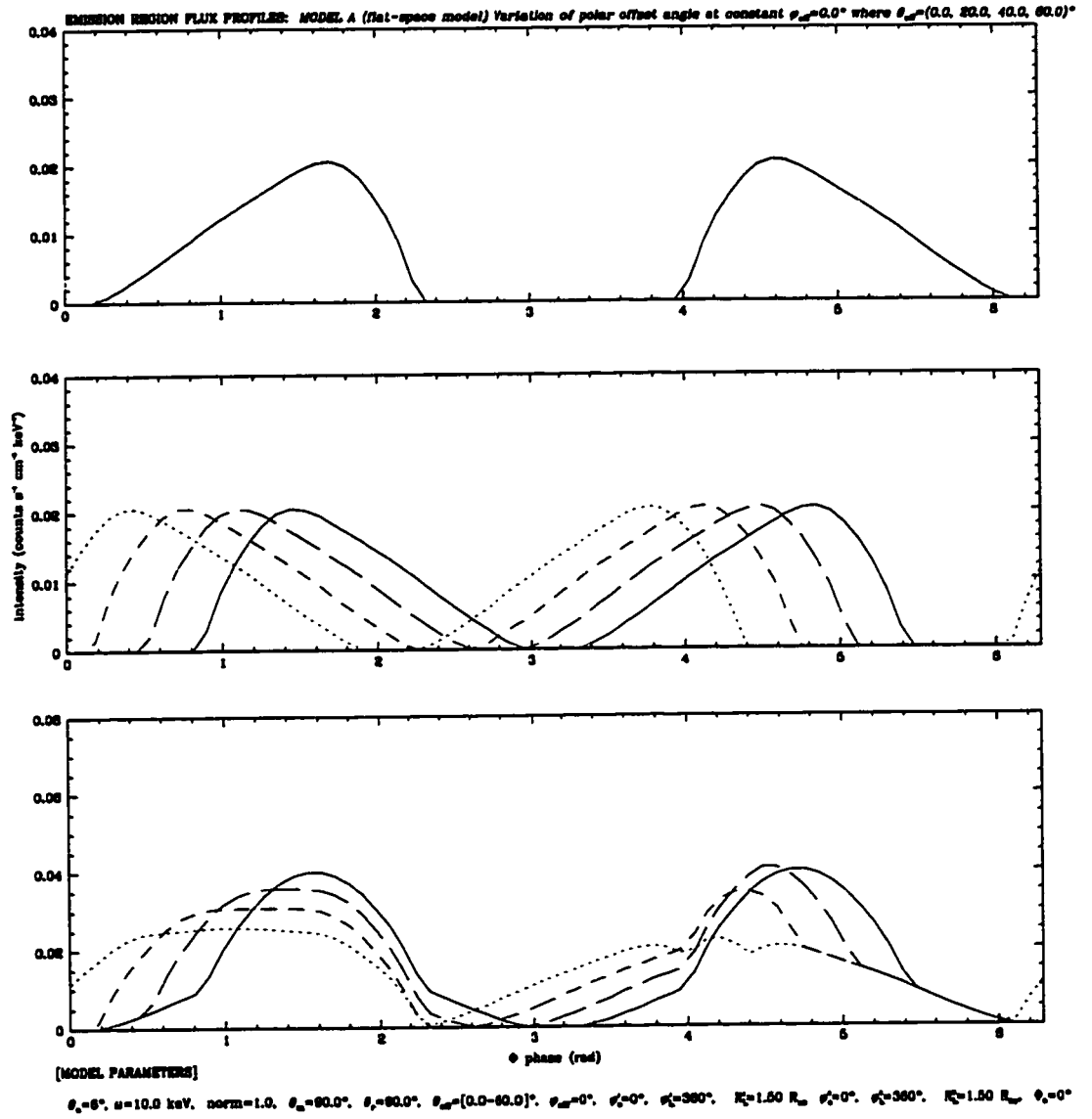

Figure 3.13: Variation of the polar offset angle, $\theta_{off} = (0.0, 20.0, 40.0, 60.0)°$ for constant $\varphi_{off} = 0.0°$.

region), the emission is seen by the observer positioned at an angle of 90° earlier in the phase of the neutron star (refer to Figure (3.14)).

Angular range of filling, φ_o, φ_L

Figure (3.15) shows the profiles for different amounts of filling of the emission regions when the emission regions are aligned with respect to the rotation axis of the neutron star, ($\theta_m = 0°$). For completely-filled regions, a constant line is profiled and is consistent with the test case shown in Figure (3.9). As the filling of the emission regions is reduced, the partially-filled section of the emission region is seen over a smaller range of phase by an observer. Effectively, the sides of the emission peaks seen in the profile become less broad, until for a partial-filling of 90°, a well-defined peak of emission is seen, which is not seen at all by an observer for certain times in the phase of rotation. In Figure (3.15) the intensity is zero for a phase of zero to $\frac{\pi}{2}$ since the outer emitting surface of each partially-filled region is directed away from the observer i.e. a value of $\varphi = 180°$ is pointing at the observer at $\Phi = 0$. Since there is no emission from the inner surface of the regions, the intensity is zero for observer directions behind the outer surface of the partially-filled emission regions. Figure (3.16) shows the sequence of results for the 90° rotation of partial-filled emission regions when $\theta_m = 0°$, for a $\varphi = 70°$ range, about the magnetic axis. The filled sections of each emission region are fixed relative to each other, and then azimuthally shifted together relative to zero phase. This effect can also be produced by simply varying the initial azimuth angle of the observer, Φ_o. For the first emission region; $\varphi_o^{(1)} = 10°$, $\varphi_L^{(1)} = 80°$, while for the second region; $\varphi_o^{(2)} = 190°$, $\varphi_L^{(2)} = 260°$. The emission peak for the first emission region is then effectively shifted with respect

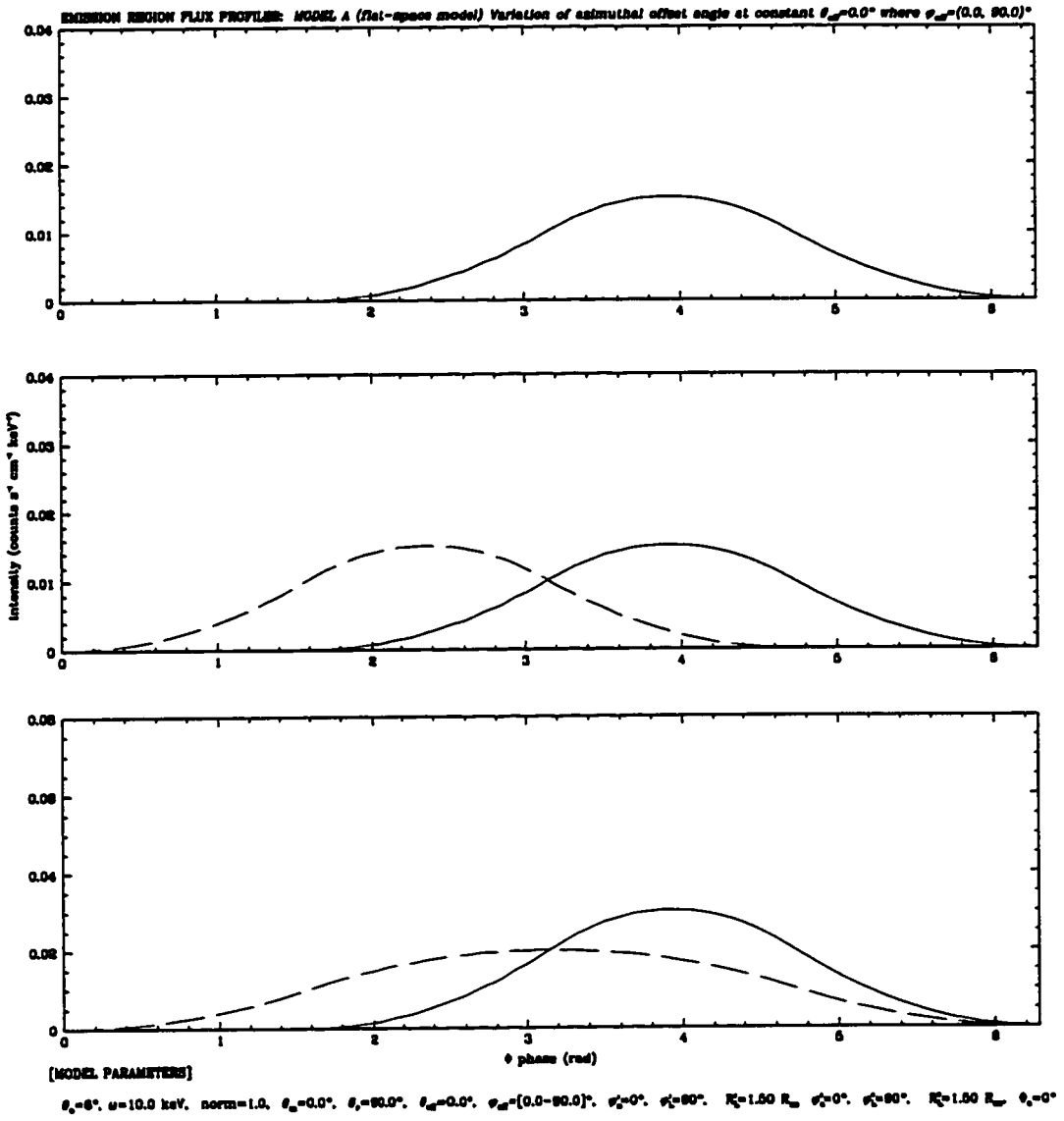

Figure 3.14: Variation of the azimuthal offset angle, $\varphi = (0.0, 90.0)°$ at constant $\theta_{off} = 0.0°$, for partially-filled regions where $\varphi_{o,L} = (0.0, 90.0)°$.

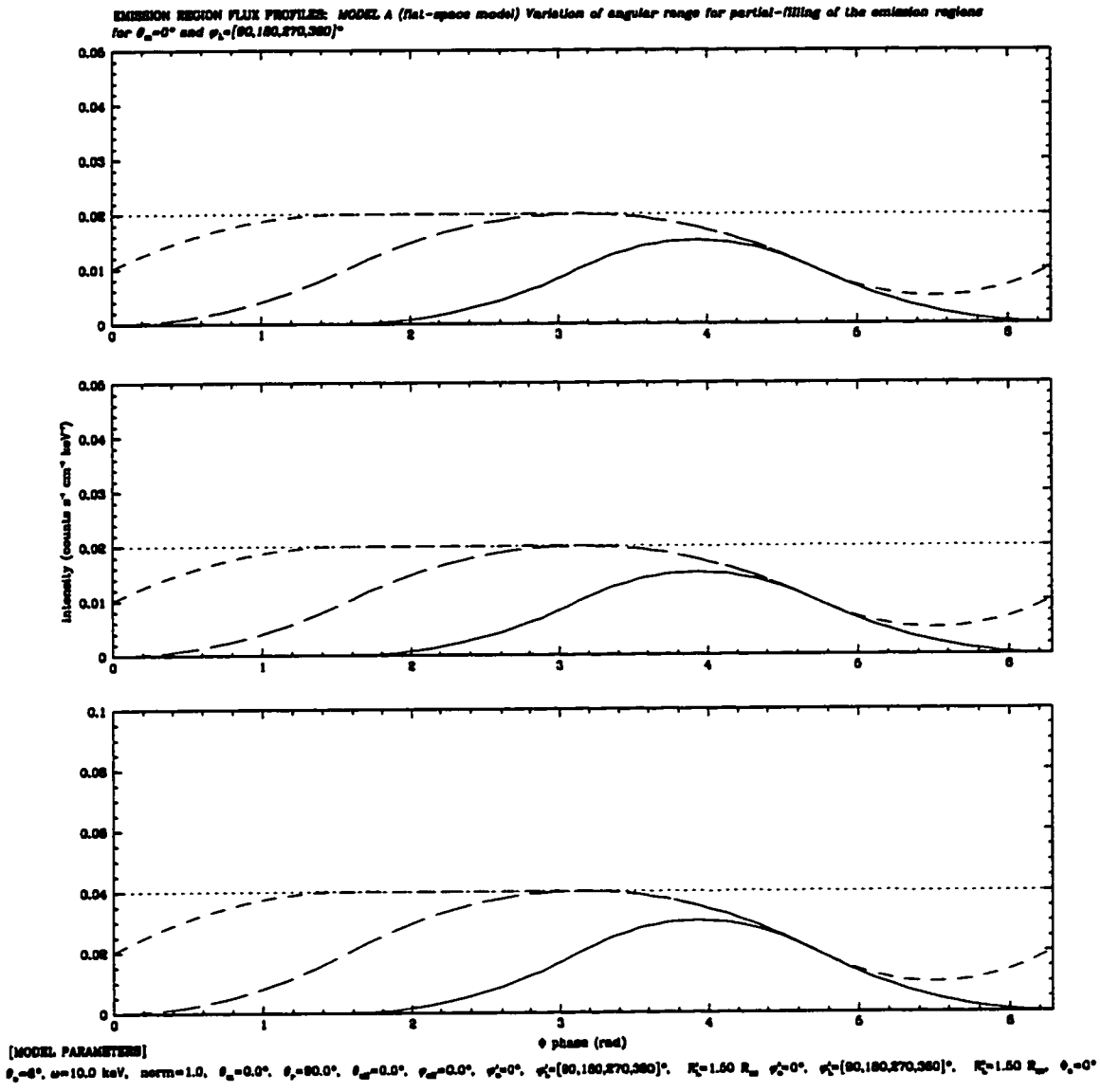

Figure 3.15: Variation of the angular range for partial-filling of the emission regions, $\theta_m = 0°$, and $\varphi_L^i = (90, 180, 270, 360)$, $i = 1, 2$.

to the second as shown. The total emission profile for this test case shows that two individual peaks can form in the pulse profiles as a result of partially-filled emission regions that are azimuthally shifted. Figures (3.17)-(3.20) show different test cases for partial-filling of the emission regions at different observer and magnetic axis angles.

Radial height, R_L^i

Figure (3.21) shows the effect of varying the radial height of the emission regions at a constant value for θ_r and θ_m. The profiles are shifted higher for the increasing radial height of the emission regions. With the sides of the emission regions following the curved magnetic field lines, the increasing radial height means that the normal vector for points near the top of each region will be directed at an increasing angle with respect to the magnetic axis. The increasing angle to the magnetic axis raises the rise and drop-off of the peaks, as seen in Figure (3.21).

Phase shift, Φ_o

Variation of the phase shift parameter is shown in Figure (3.22). This parameter is the initial phase angle for the emission profile where $\Phi_o = 0$ means that the azimuthal angle $\varphi = 0$, and is pointing to the observer. Variation of this parameter shifts the full emission profile of the neutron star.

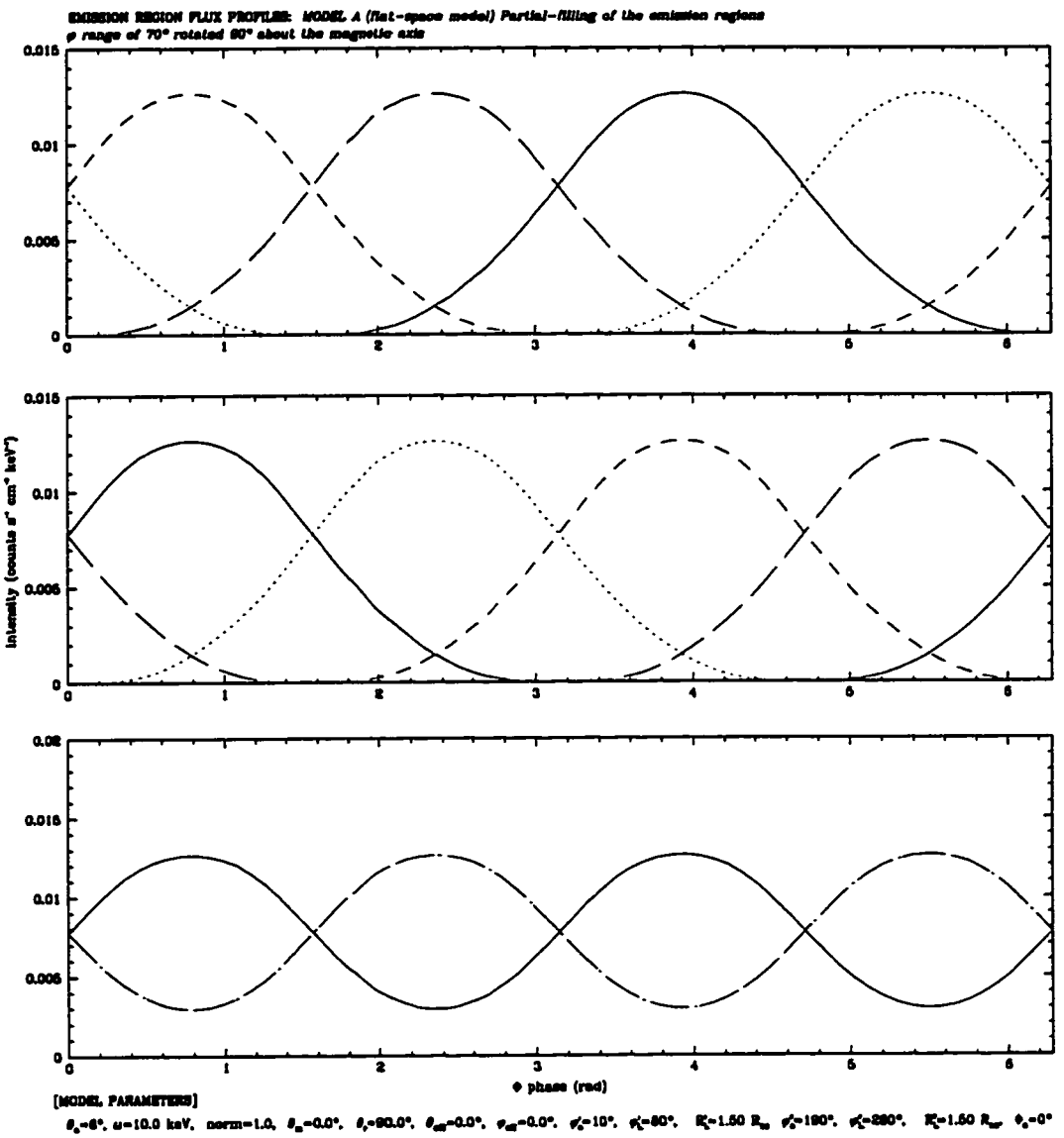

Figure 3.16: Azimuthal rotation of a partial-filling section of azimuthal extent of 70°, in 90° steps about the magnetic axis.

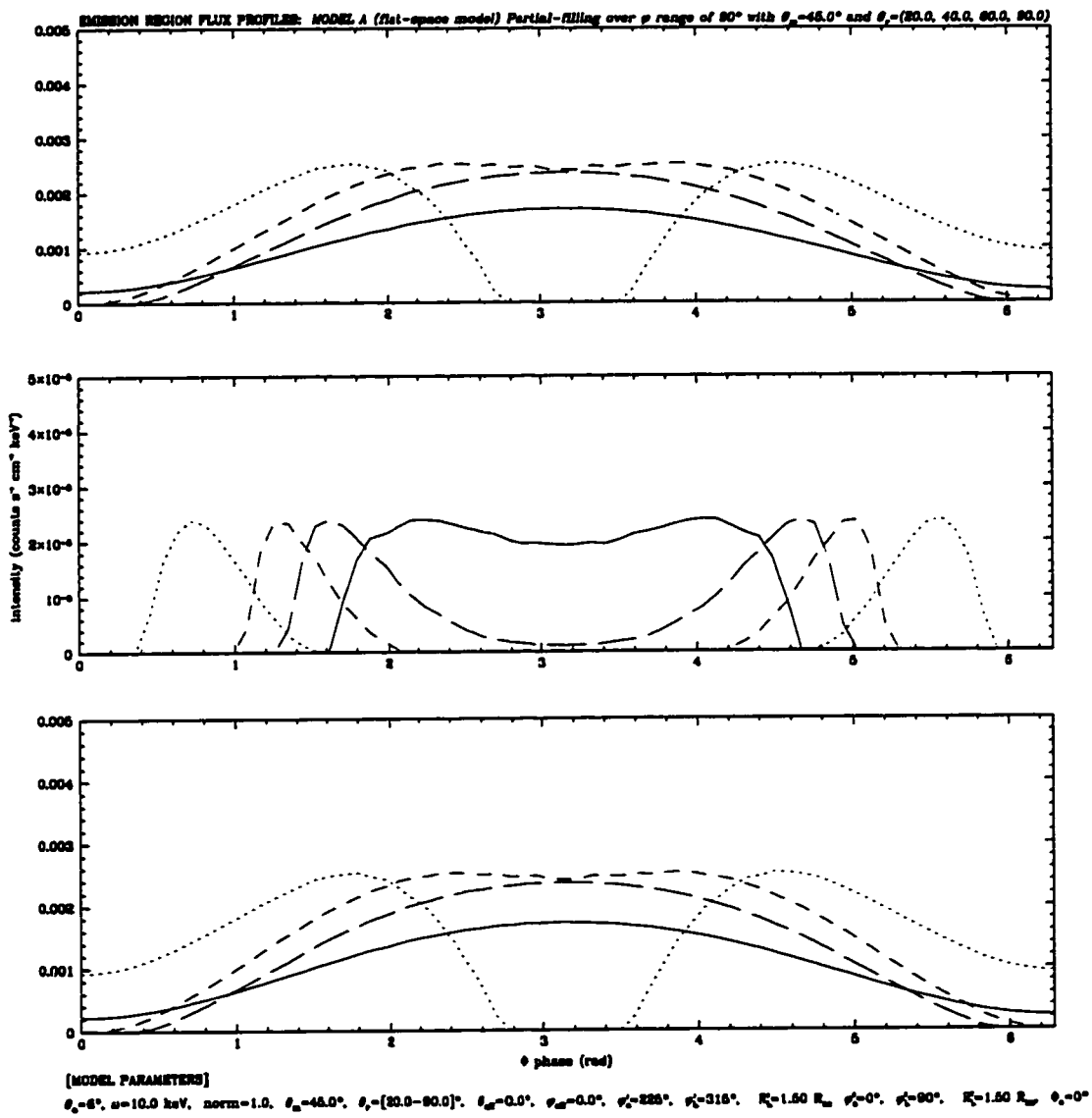

Figure 3.17: Partial-filling over a φ range of 90° with θ_m=45°, for θ_r=(20, 40, 60, 90)°.

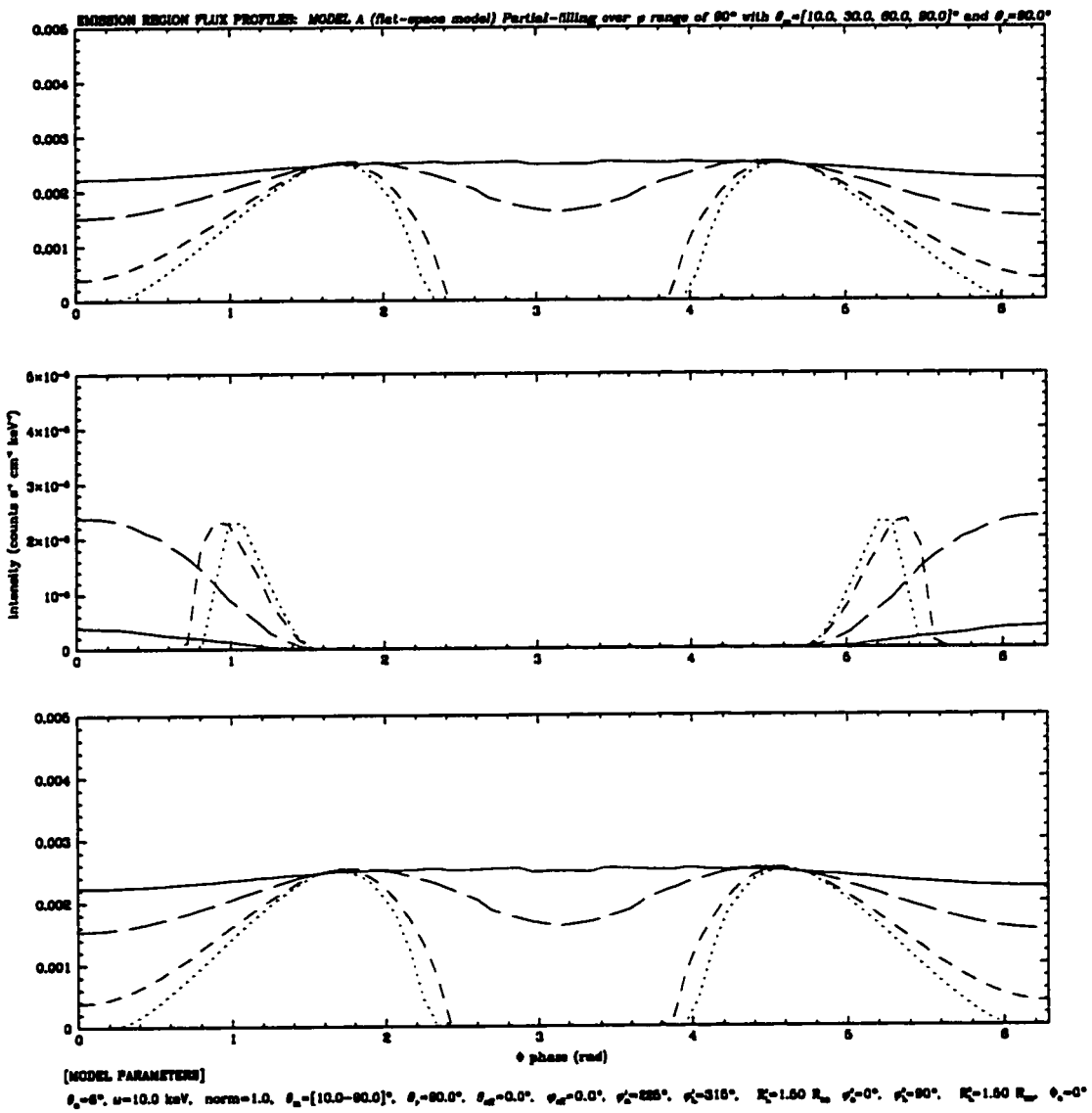

Figure 3.18: Partial-filling over a φ range of 90° with $\theta_r = 90°$, for θ_m=(10, 30, 60, 90)°

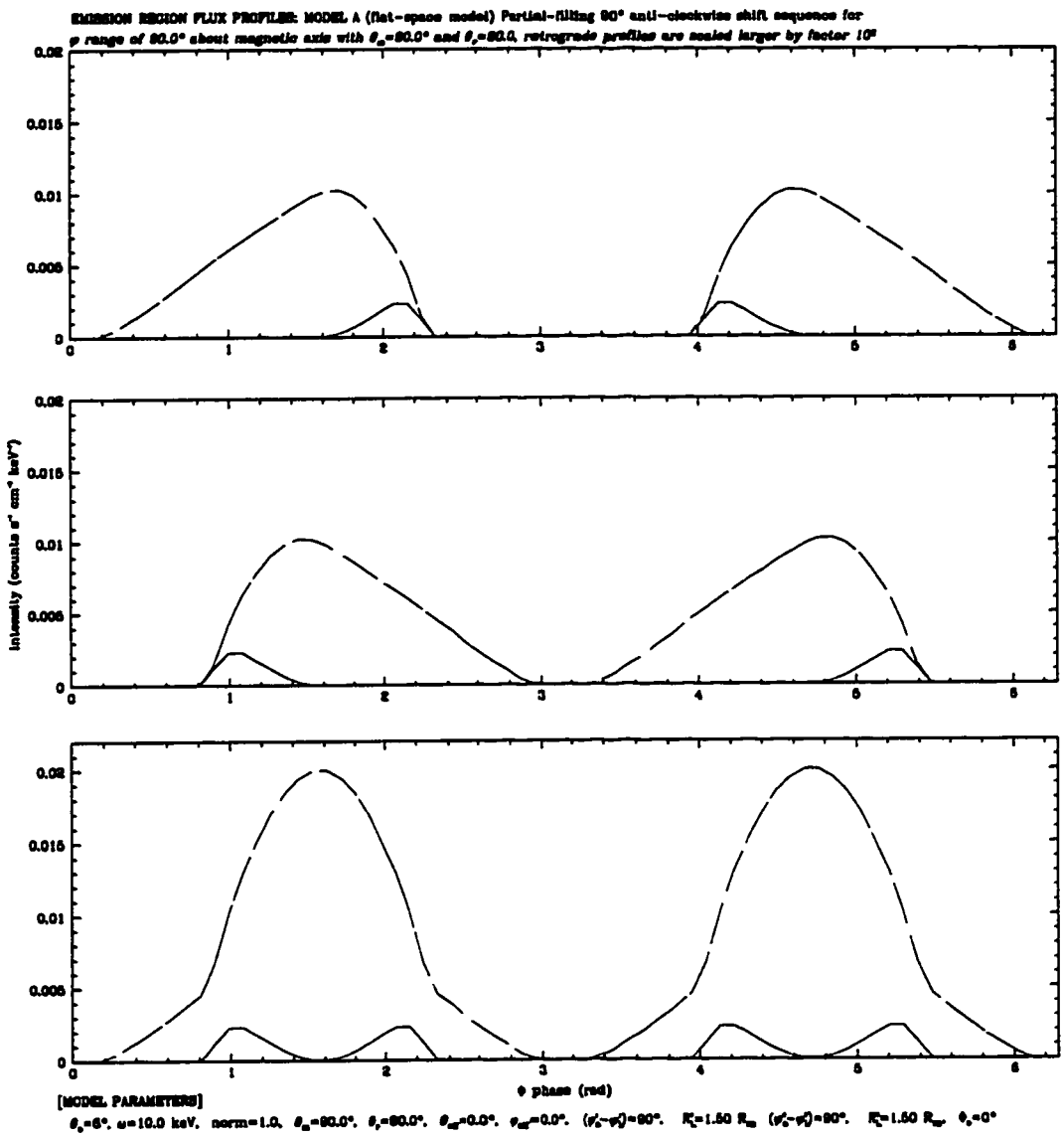

Figure 3.19: Partial-filling with φ range of 90° about the magnetic axis, with $\theta_m = 90°$ and $\theta_r = 90°$. Emission from these regions is initially directed away from the observer (retrograde profile). By shifting the emission regions in the anti-clockwise direction about the magnetic axis, emission is directed toward the observer. Retrograde profiles are scaled larger by a factor of 10^2.

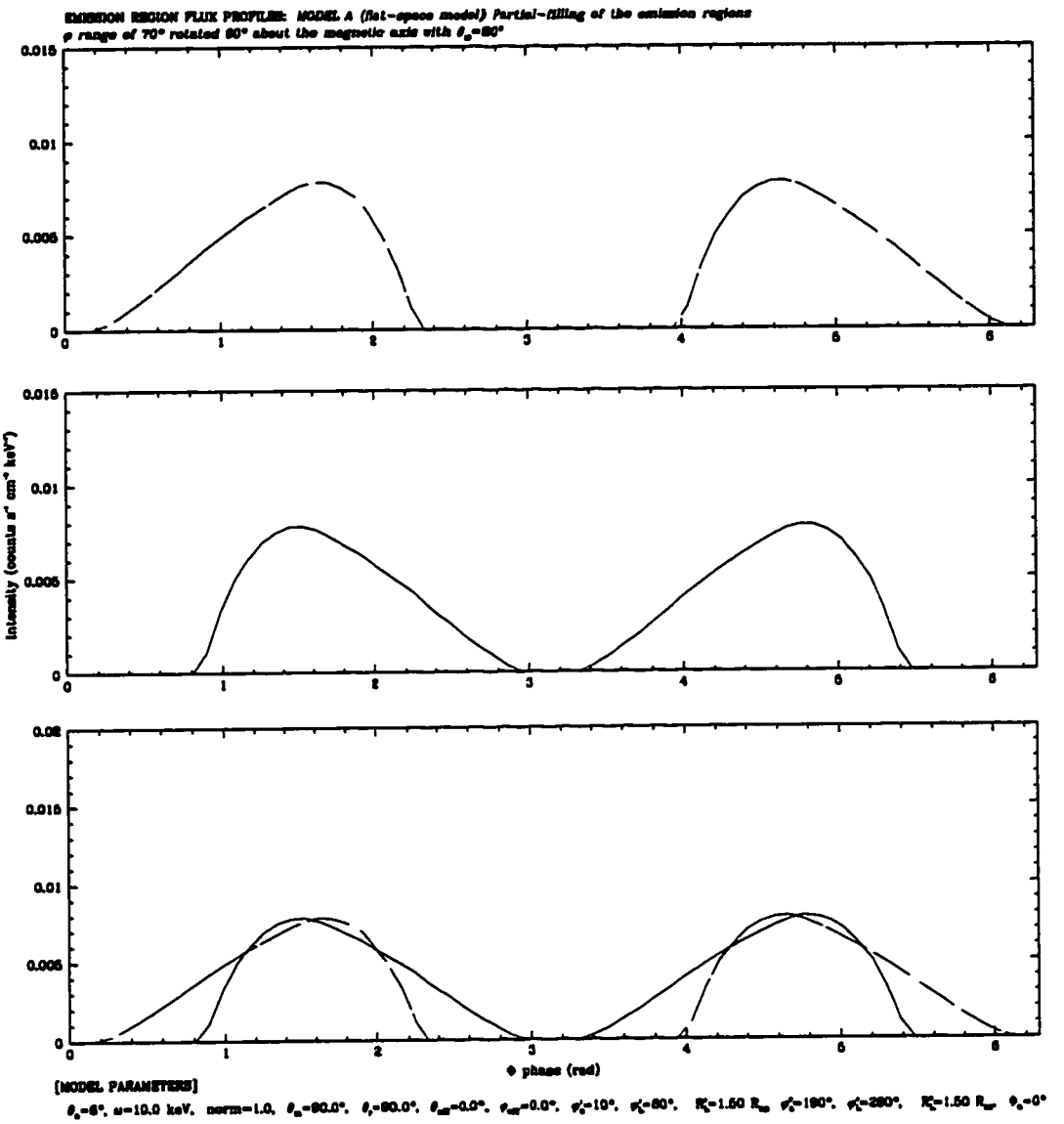

Figure 3.20: Partial-filling of the emission regions for a φ range of 70°, with $\theta_m = 90°$, $\varphi_o^1 = 10°$, $\varphi_L^1 = 80°$, $\varphi_o^2 = 190°$, $\varphi_L^2 = 280°$. Emission from region 1 and 2 is directed away and toward the observer respectively. These regions are then rotated 90° anti-clockwise about the magnetic axis, and emission from region 1 is then directed toward the observer.

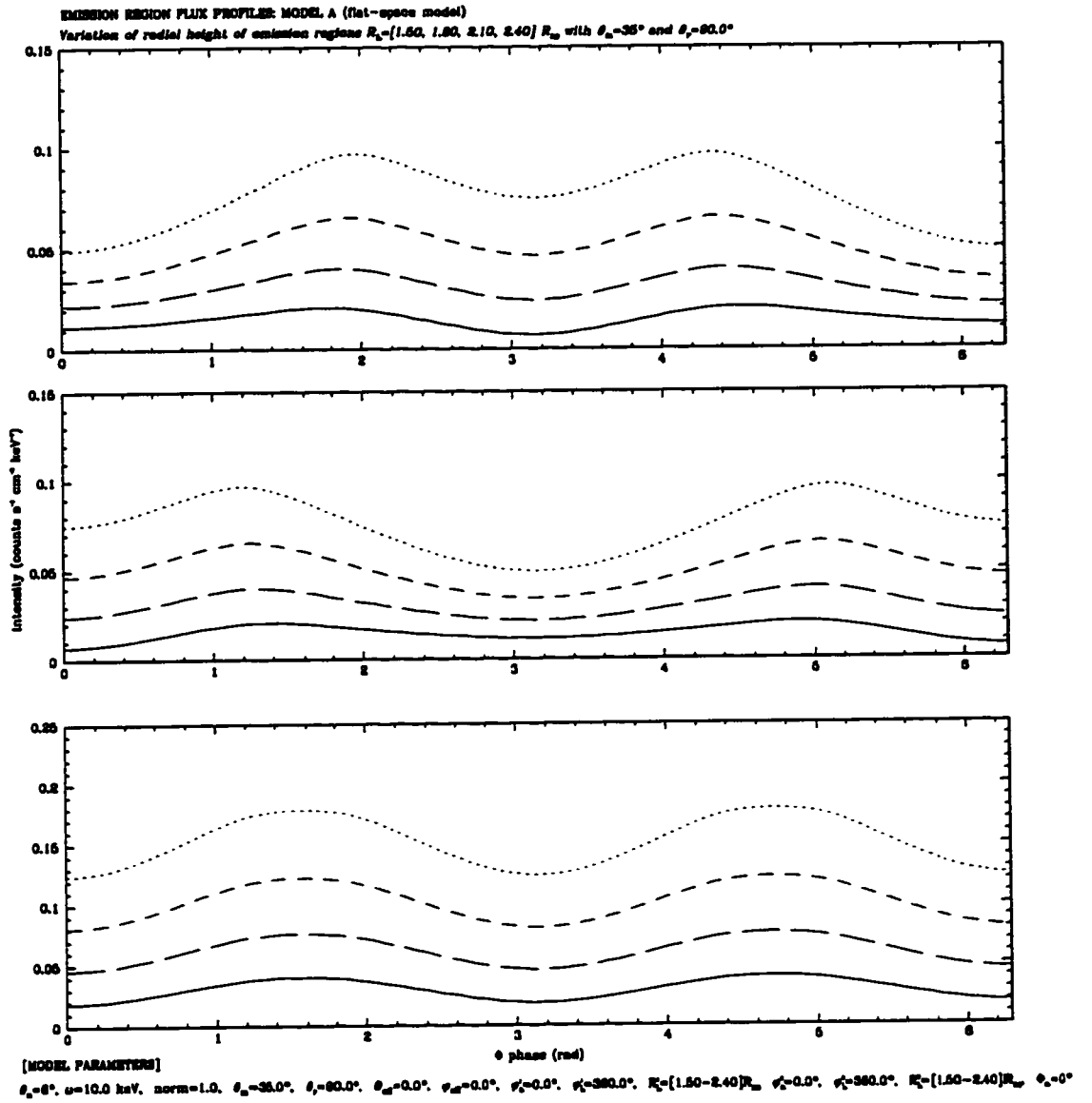

Figure 3.21: Variation of radial height of emission regions, R_L=(1.5, 1.8, 2.1, 2.4)·R_{ns}, with θ_m=35° and θ_r=90°.

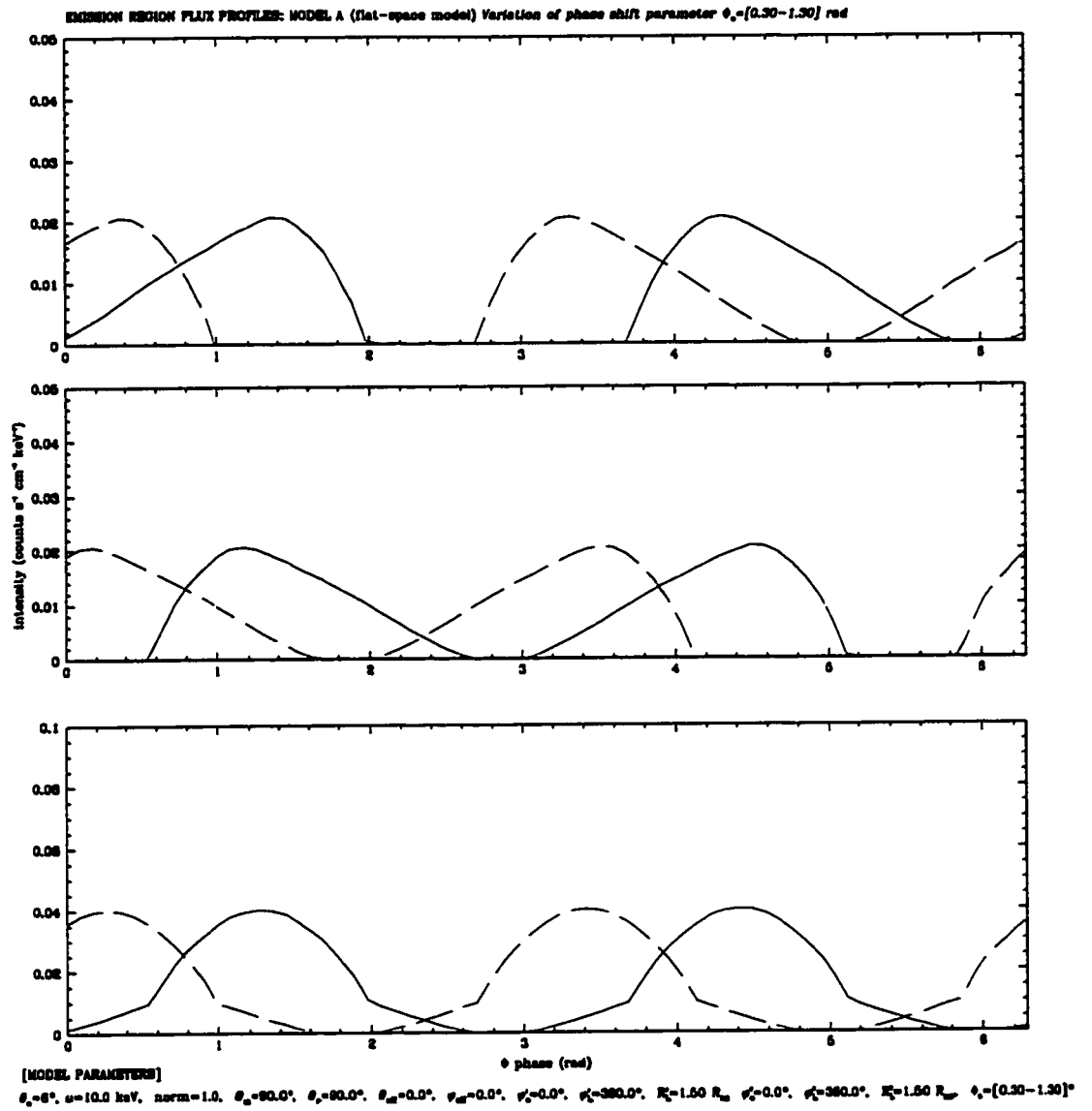

Figure 3.22: Variation of the phase shift parameter, Φ_o=(0.3, 1.3).

Chapter 4

Fitting Observed Pulse Profiles

The observed pulse profiles of x-ray pulsars are determined primarily by scattering and absorption processes within the neutron star's magnetosphere, and act as important probes for the structure of the magnetosphere and its interaction with accreting plasma. Detailed fits to the pulse profile observations of accreting neutron stars are essential to establishing their preferred beaming direction (fan or pencil beam) and viewing geometry. Previous work by Wang *et al.*, (1981)[54] and more recent work by Leahy, (1990),(1991)[7][8] has shown that polar caps of emission lying on the neutron star surface are able to reproduce the observed pulse profiles of many x-ray pulsars. Pulse profile modelling of EXO 2030+375 using analytic pencil-beam emission models suggests that radiation from its emission regions may switch between pencil and fan-beam emission (Parmar *et al.*, 1989)[4](Li and Leahy, 1995)[9].

4.1 The Nonlinear Fitting Method

4.1.1 General algorithm for fitting the pulse profiles

The IMSL routine DBCLSF was implemented for the fitting of the model parameters to observed pulse profiles. This procedure uses a modified Levenberg-Marquardt method algorithm to solve a nonlinear least-squares (NLSQ) problem subject to

bounds on the variables.

$$min_{x \in R^n} \frac{1}{2} F(x)^T F(x) \quad = \quad \frac{1}{2} \sum_{i=1}^{m} f_i(x)^2, \quad l \leq x \leq u \tag{4.1}$$

where the number of observation data points $m \geq n$, the number of parameters. The number of observation points was 70 and 21 for the EXOSAT and BATSE data respectively. F(x) is the difference function given by,

$$F(x) = (f_{observation} - f_{theoretical}) \tag{4.2}$$

By specifying a given initial parameter vector, an active set containing the indicies of the variables at their bounds is built. Free variables which can be changed are those that are not in the active set. When a free variable hits its bounds during an iteration, the active variable set is updated. For the free variables, the routine computes a search direction according to,

$$d = -(J^T J + \mu I)^{-1} J^T F. \tag{4.3}$$

μ is the Levenberg-Marquardt parameter, $F = F(x)$. J is the Jacobian matrix with respect to the free variables. and is computed using a finite-difference method. A new point is found by a trust region approach until the desired optimality is acheived.[1]. The routine outputs the fitted parameter and function vectors. The computation time of the fitting program depends greatly on the choice of the initial parameter vector, varying from 3-14 hrs, running on an IBM RISC system RS/6000-950. Fitting of the profiles for specific energies, whereby integration of the flux over energy is not performed reduces the computation time substantially.

[1]see IMSL routine DBCLSF

4.2 Pulse Profiles of EXO 2030+375

4.2.1 BATSE observations

Figure (4.1) shows the recent observations of EXO 2030+375 by BATSE. For a complete description of these observations see Stollberg *et al.*, (1994)[31]. The observed pulse profiles cover a range of luminosity from ($4.79 \cdot 10^{33}$ - $1.75 \cdot 10^{36}$) ergs s^{-1} (for a distance of 5 kpc) within the energy range (20-50 keV). The profiles seen in Figure (4.1) labelled range (1-7) each refer to a flux interval chosen to evenly span the entire range of flux of (20-50 keV). Each of these profiles is formed from 21 measurements. As luminosity increases, the peaks of the pulse profiles become more distinct.

4.3 Results of Fitting the BATSE profiles

Best-Fit Parameters

The parameters of the theoretical model were varied so as to closely approximate each profile, and an initial parameter set was then obtained. All seven of the BATSE pulse profiles of EXO 2030+375 were fitted to the asymmetric emission model with an observed energy of E_{obs} = 10 keV and cyclotron energy of E_{cyc}=57 keV (see Figure (4.48)). The observer was initially placed at an angle of 90° from the rotation axis, but the angle was allowed to vary as a free parameter in the fitting procedure. The polar cap cyclotron frequency for the EXOSAT observations of EXO 2030+375 was determined to be 57 keV (Parmar *et al.*, 1985)[5], corresponding to the observed pulse profile of August, 13, which has the lowest luminosity. This value was used for fitting the observed pulse profiles. The first three profiles (ranges 1-3) were

Table 4.1: Best-fit parameters for the BATSE pulse profiles of EXO 2030+375 with $E_{obs} = 10keV$.

L (ergs/s)	θ_o	θ_m	θ_r	θ_{off}	ϕ_{off}	$\varphi_o^{(1)}$	$\varphi_o^{(2)}$	$\varphi_L^{(1)}$	$\varphi_L^{(2)}$	$\mathbf{R}_L^{(1)}$	$\mathbf{R}_L^{(2)}$	$\mathbf{\Phi}_o$
$4.79{\cdot}10^{33}$	6.0	18.0	90.0	0.0	0.0	90.0	0.0	179.3	90.0	1.50	1.50	0.0
$5.51{\cdot}10^{35}$	8.3	21.3	90.0	90.0	0.0	70.3	0.0	360.0	108.5	1.52	1.90	0.0
$7.91{\cdot}10^{35}$	8.0	40.0	90.0	30.0	0.0	215.0	10.0	300.1	100.0	2.10	2.30	0.0
$1.03{\cdot}10^{36}$	7.8	40.0	90.0	30.0	0.0	214.3	9.34	300.1	100.2	2.10	2.30	0.0
$1.27{\cdot}10^{36}$	8.0	30.0	90.0	0.0	0.0	225.0	0.0	315.0	90.0	1.54	1.50	5.98
$1.51{\cdot}10^{36}$	9.9	30.0	80.9	0.0	0.0	224.8	0.0	350.3	90.0	1.54	1.50	5.98
$1.75{\cdot}10^{36}$	15.0	26.8	90.0	0.0	0.0	21.3	0.0	337.0	137.4	1.54	1.50	0.0

Table 4.2: Best-fit parameters for the BATSE pulse profiles of EXO 2030+375 with $E_{obs} = 35keV$.

L (ergs/s)	θ_o	θ_m	θ_r	θ_{off}	ϕ_{off}	$\varphi_o^{(1)}$	$\varphi_o^{(2)}$	$\varphi_L^{(1)}$	$\varphi_L^{(2)}$	$\mathbf{R}_L^{(1)}$	$\mathbf{R}_L^{(2)}$	$\mathbf{\Phi}_o$
$4.79{\cdot}10^{33}$	6.0	18.0	84.6	0.0	0.0	90.0	0.0	205.9	90.0	1.50	1.50	0.30
$5.51{\cdot}10^{35}$	6.0	18.0	82.0	0.0	0.0	90.0	0.0	206.5	90.0	1.50	1.50	0.30
$7.91{\cdot}10^{35}$	8.0	30.0	90.0	0.0	0.0	215.0	10.0	300.0	100.0	2.10	2.30	0.0

then fitted for an E_{obs} energy of 35 keV. The theoretical profiles were numerically calculated at these specific energies. Table 4.1 and Table 4.2 shows the best-fit parameters corresponding to each of the BATSE pulse profiles for E_{obs}=10 keV and 35 keV respectively. The values for angles in these two tables are given in degrees, except ϕ_1 which is in radians. $R_L^{(1)}$ and $R_L^{(2)}$ are in units of the neutron star radius. The best-fit parameters were used in constructing a 45° phase rotation sequence using VRML[2] visualization of the emission region geometry for each profile.

[2]Virtual Reality Modelling Language

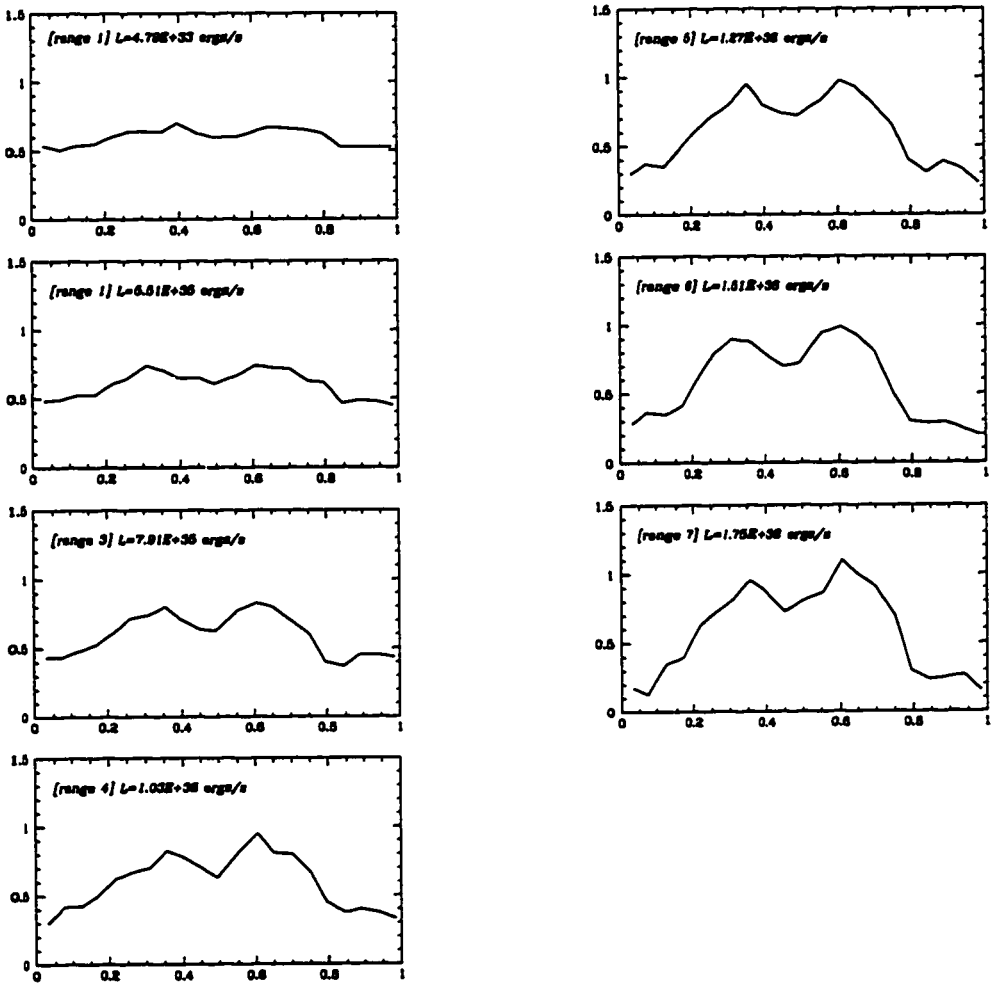

Figure 4.1: Normalized pulse profiles of BATSE observations for EXO $2030+375$ of normalized intensity versus phase for an energy range of $20-50$ keV. Each of these profiles were obtained by averaging the counts for data collected over three days.

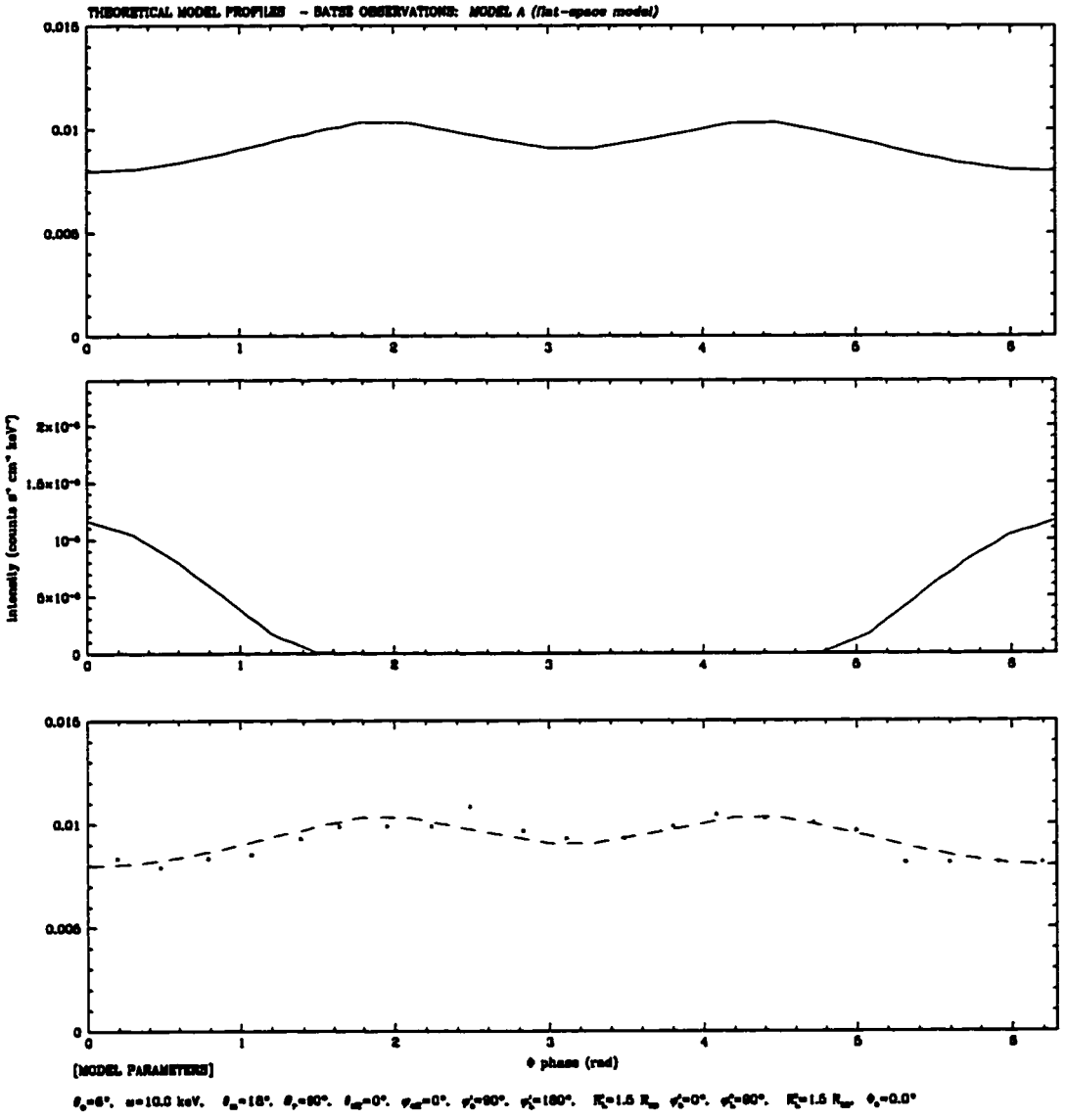

Figure 4.2: Theoretical model curve for BATSE observation [range 1], L=4.79·10^{33} ergs/s pulse profile, before NLSQ fitting, E_{obs}=10 keV.

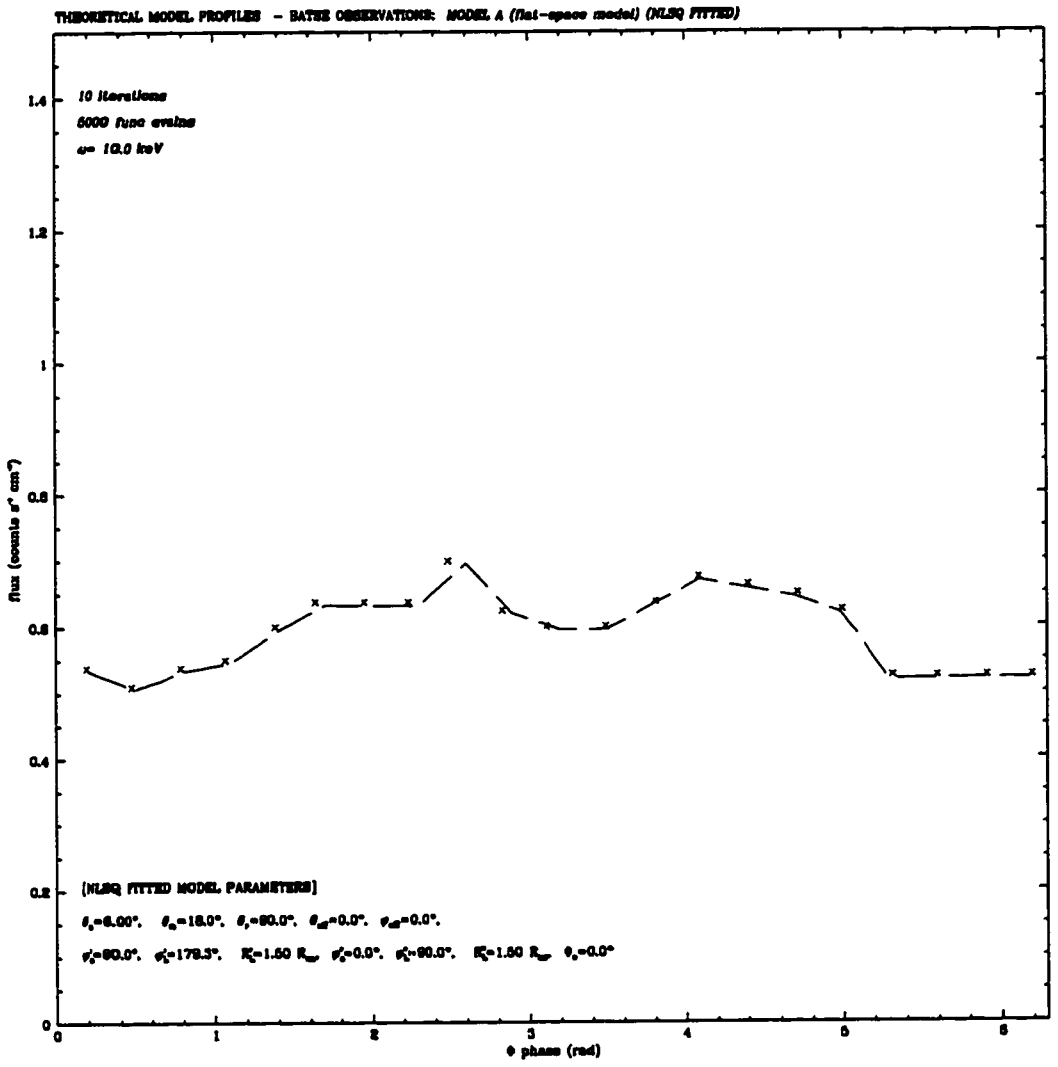

Figure 4.3: Results of NLSQ fitting of BATSE observation [range 1], $L = 4.79 \cdot 10^{33}$ ergs/s pulse profile, for $E_{obs} = 10$ keV.

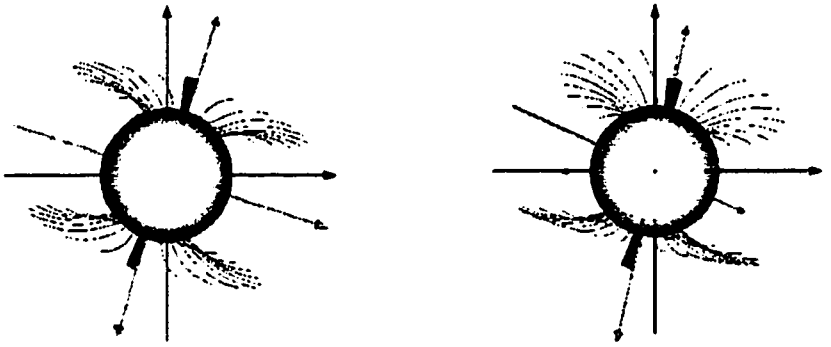

Figure 4.4: VRML visualization for best-fit parameters of BATSE pulse profile for $L = 4.79{\cdot}10^{33}$ ergs/s, for $E_{obs} = 10$ keV, where Φ=(0, 45)

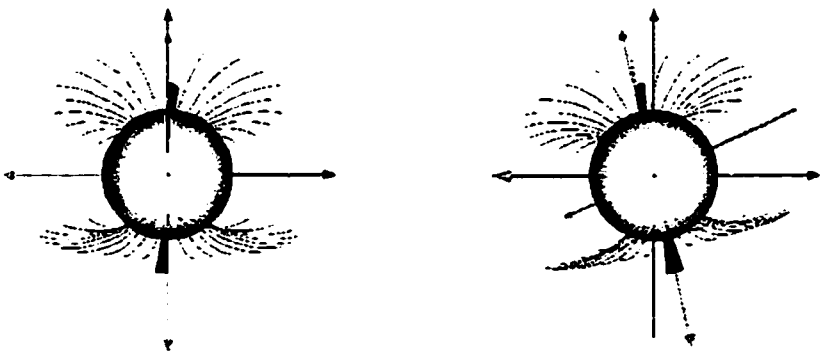

Figure 4.5: Φ=(90, 135)

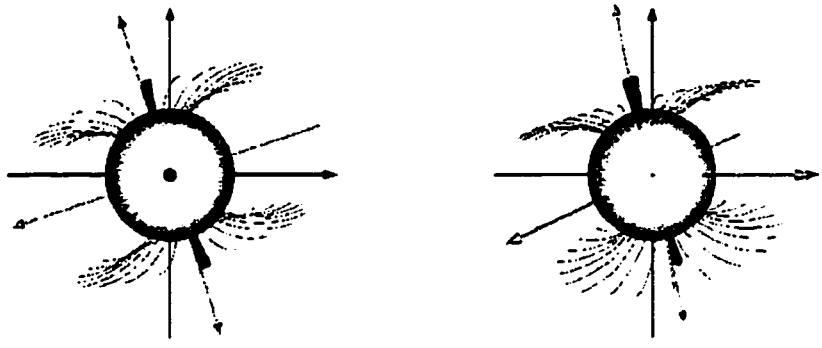

Figure 4.6: Φ=(180, 225)

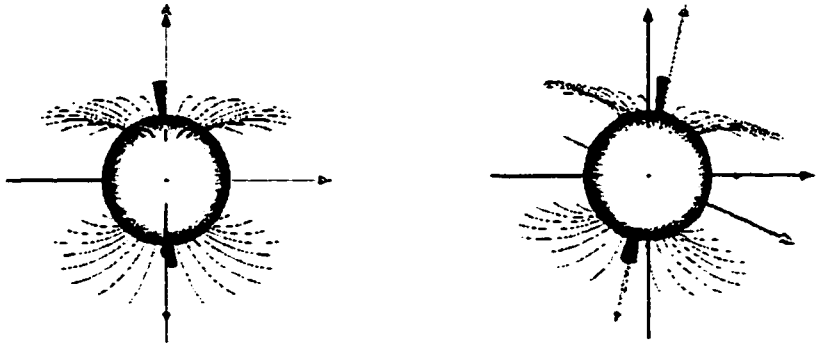

Figure 4.7: Φ=(270, 315)

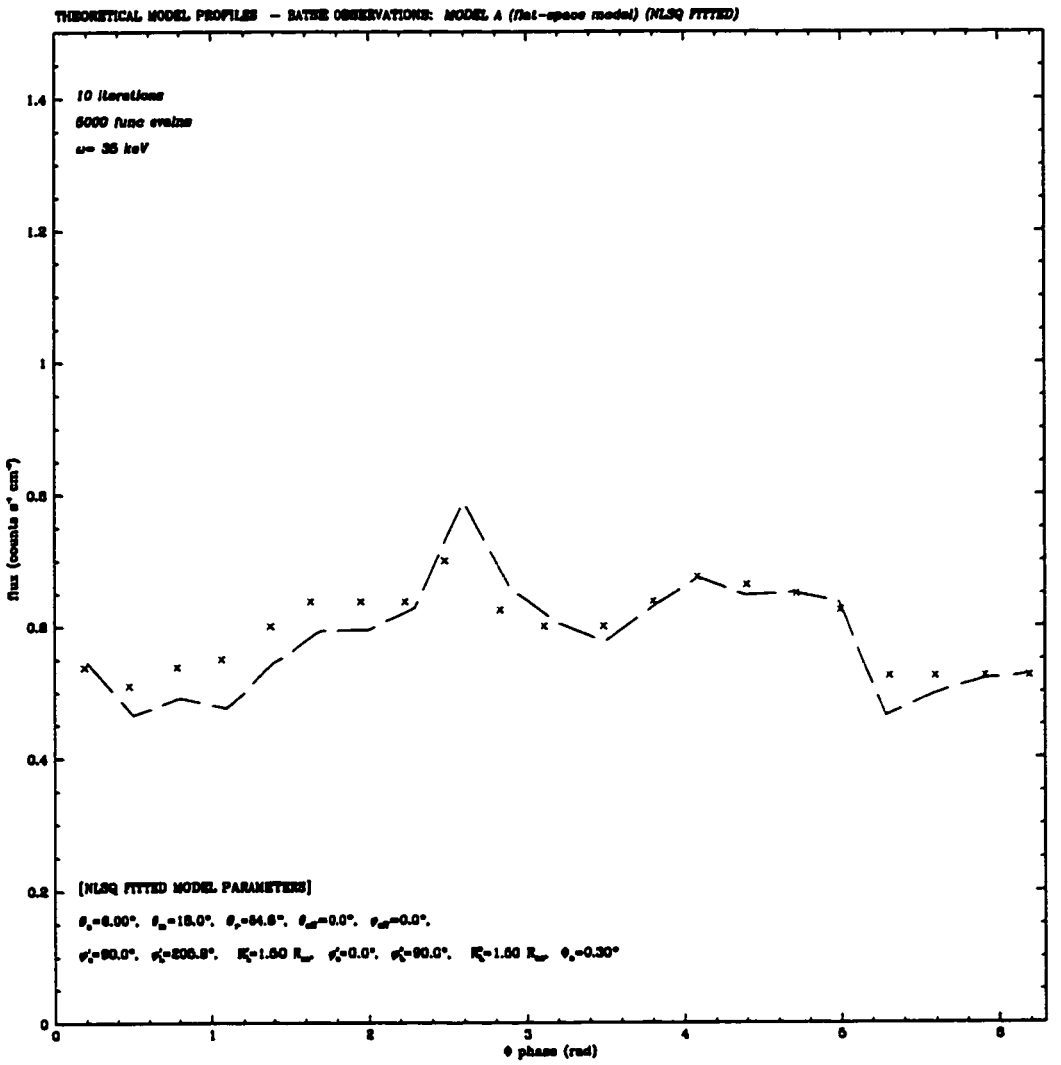

Figure 4.8: Results of NLSQ fitting of BATSE observation [range 1], $L = 4.79{\cdot}10^{33}$ ergs/s pulse profile, for $E_{obs} = 35$ keV.

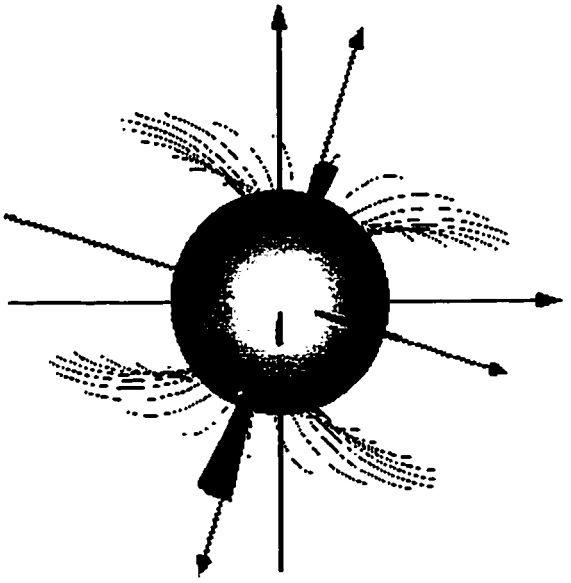

Figure 4.9: VRML visualization for best-fit parameters of BATSE pulse profile for $L = 4.79 \cdot 10^{33}$ ergs/s, for $E_{obs} = 35$ keV.

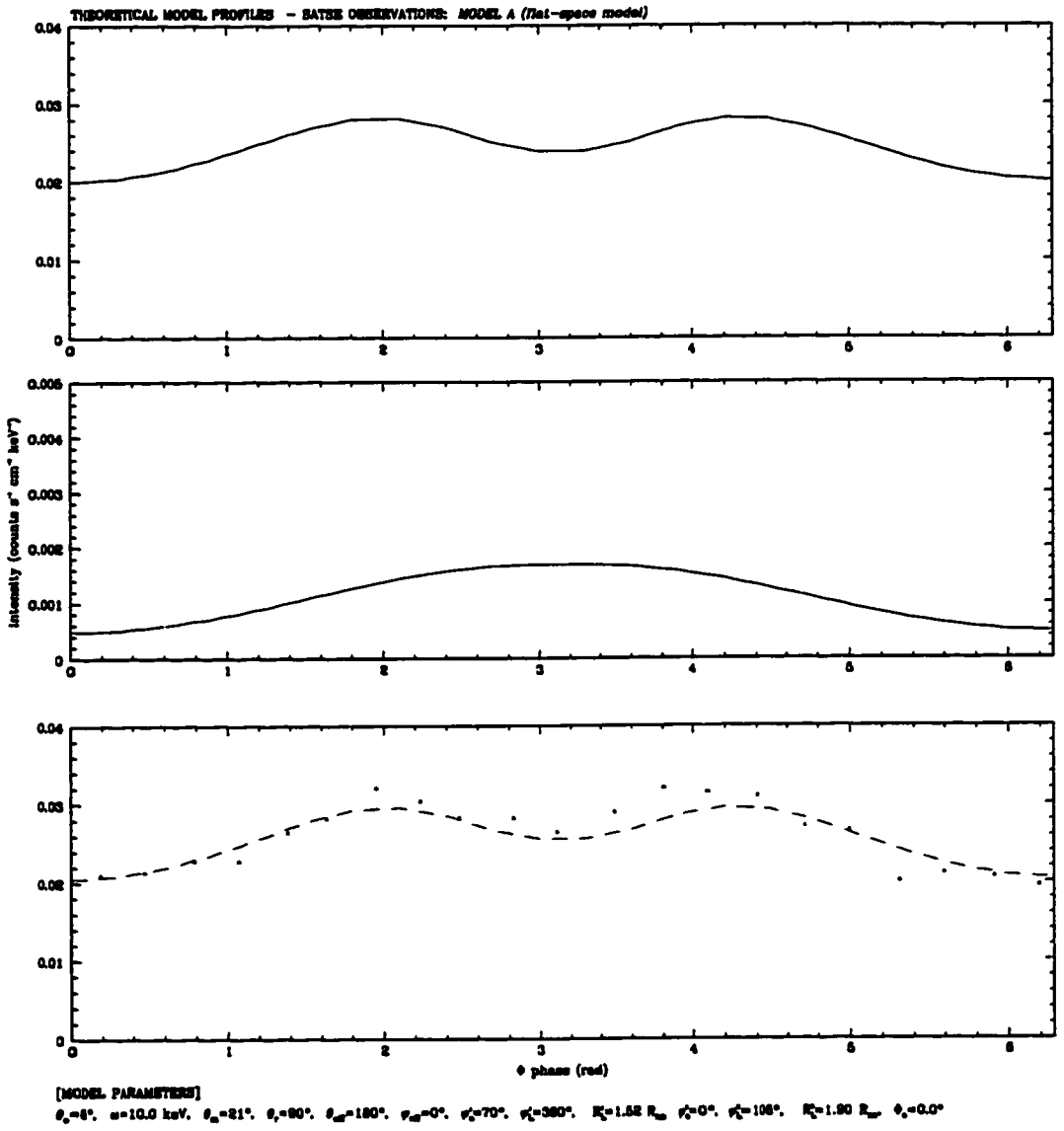

Figure 4.10: Theoretical model curve for BATSE observation [range 2], $L = 5.51 \cdot 10^{35}$ ergs/s pulse profile, before NLSQ fitting, $E_{obs} = 10$ keV.

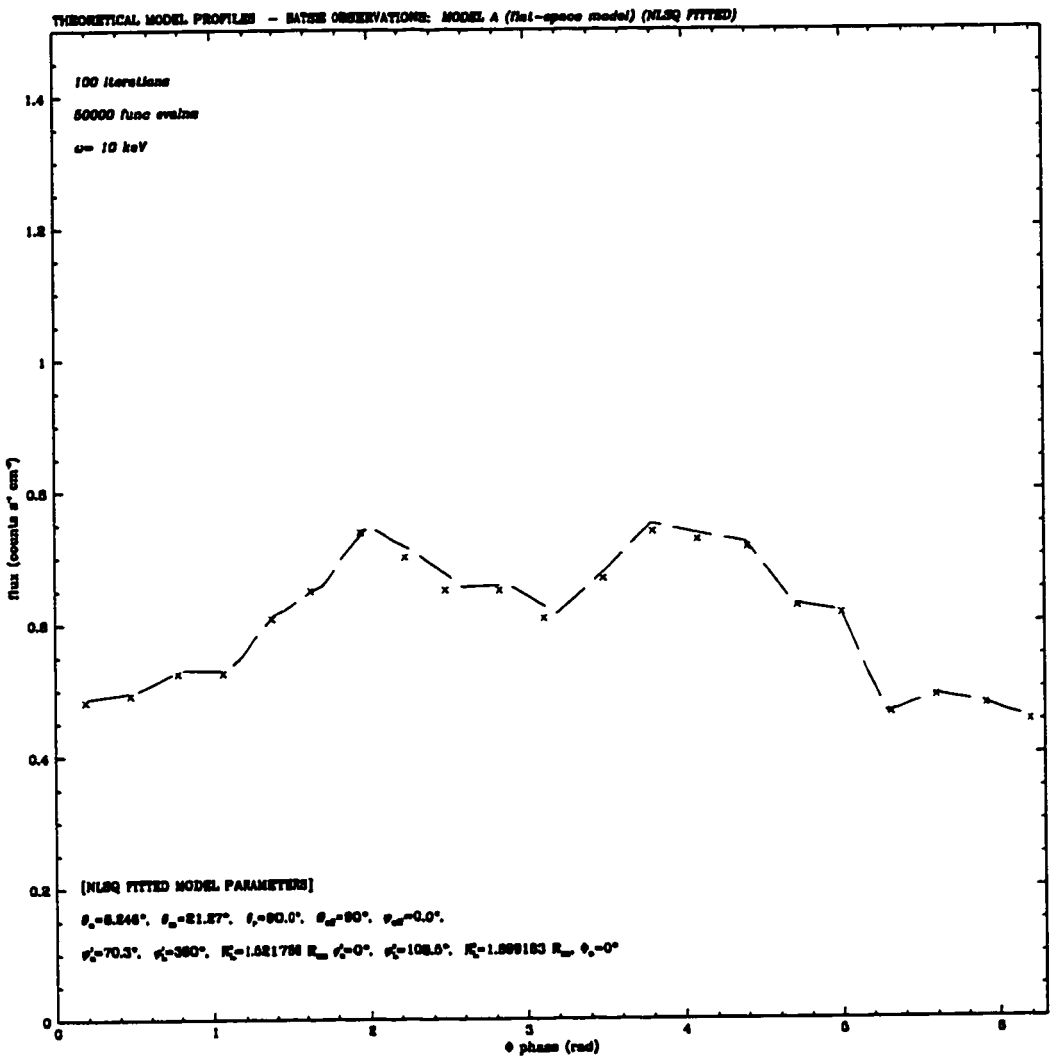

Figure 4.11: Results of NLSQ fitting of BATSE observation [range 2], $L = 5.51 \cdot 10^{35}$ ergs/s pulse profile, for $E_{obs} = 10$ keV.

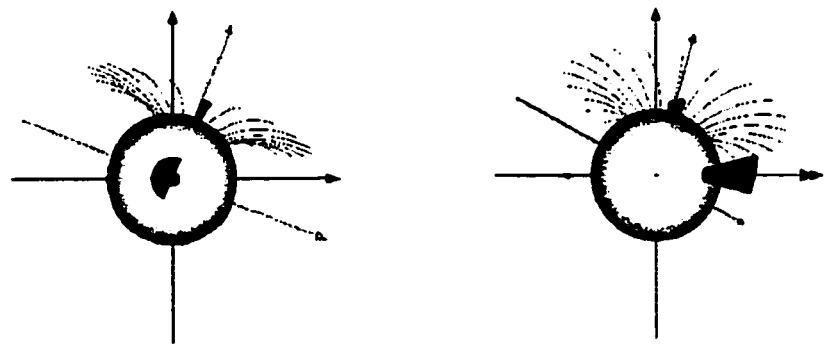

Figure 4.12: VRML visualization for best-fit parameters of BATSE pulse profile for $L = 5.51{\cdot}10^{35}$ ergs/s, for $E_{obs} = 10$ keV, where Φ=(0, 45)

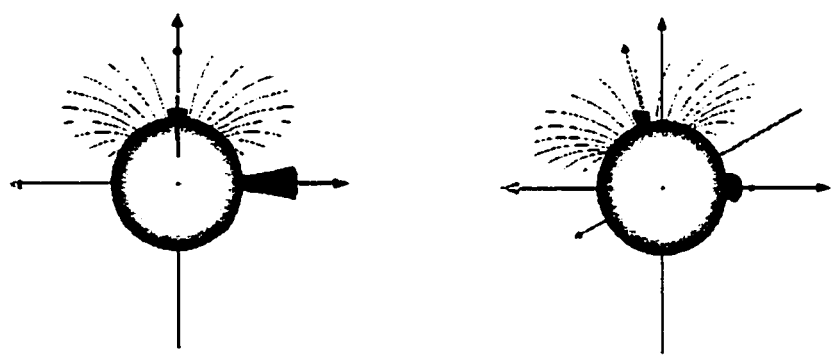

Figure 4.13: Φ=(90, 135)

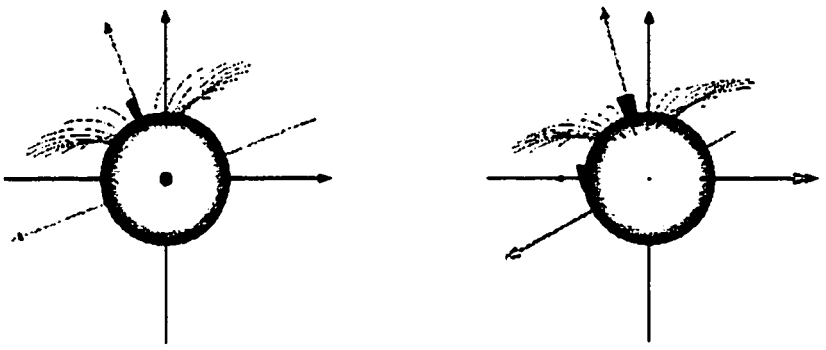

Figure 4.14: Φ=(180, 225)

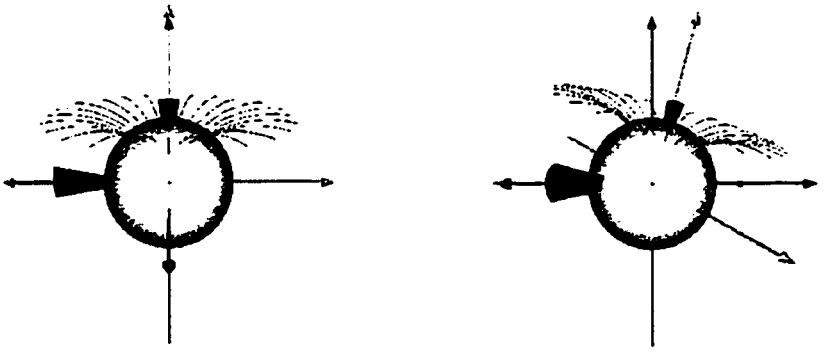

Figure 4.15: Φ=(270, 315)

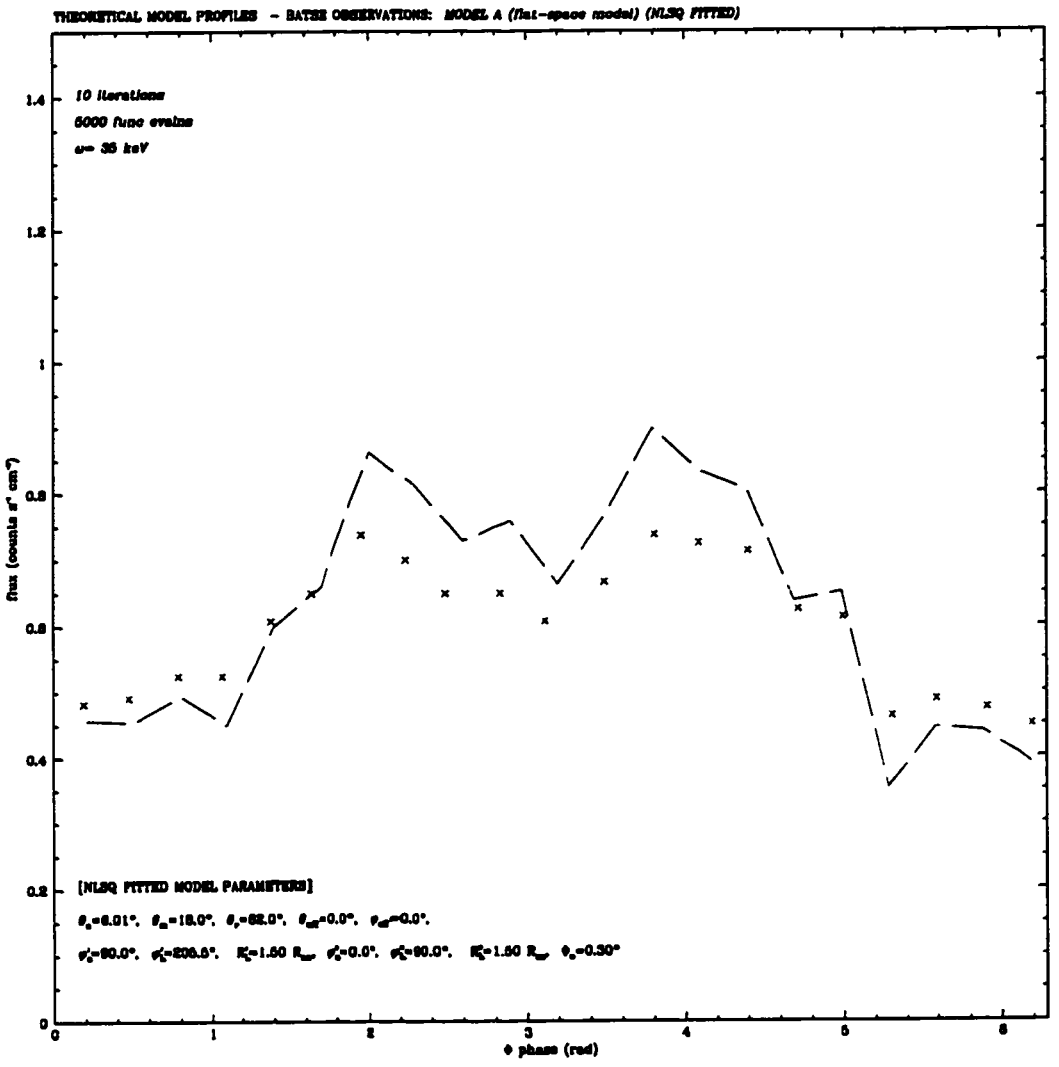

Figure 4.16: Results of NLSQ fitting of BATSE observation [range 2], $L = 5.51 \cdot 10^{35}$ ergs/s pulse profile, for $E_{obs} = 35$ keV.

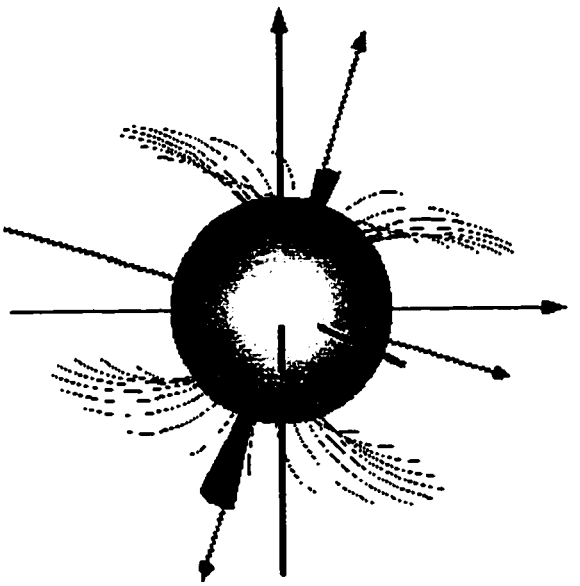

Figure 4.17: VRML visualization for best-fit parameters of BATSE pulse profile for $L = 5.51 \cdot 10^{35}$ ergs/s, for $E_{obs} = 35$ keV.

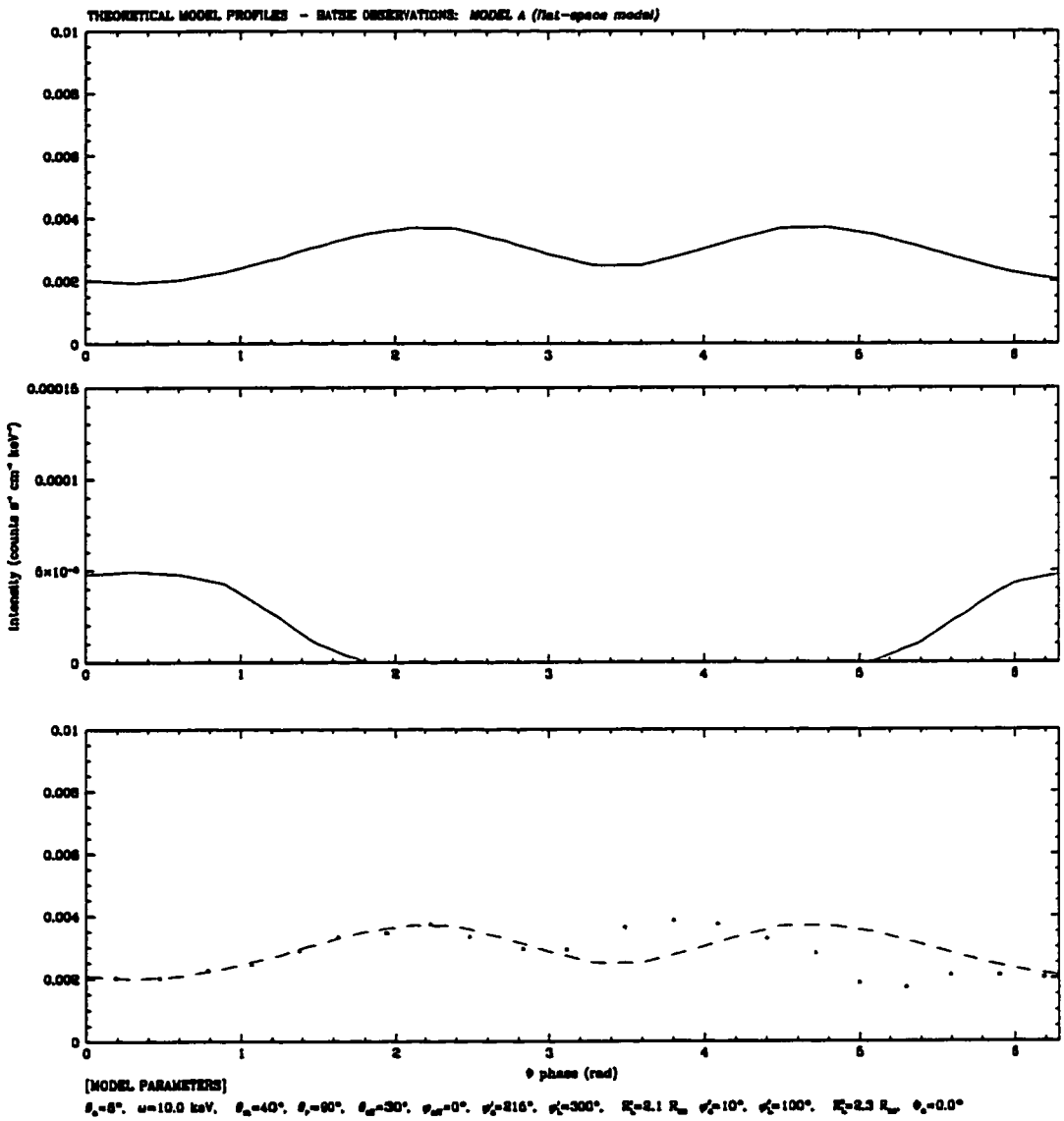

Figure 4.18: Theoretical model curve for BATSE observation [range 3], $L = 7.91 \cdot 10^{35}$ ergs/s pulse profile, before NLSQ fitting, $E_{obs} = 10$ keV.

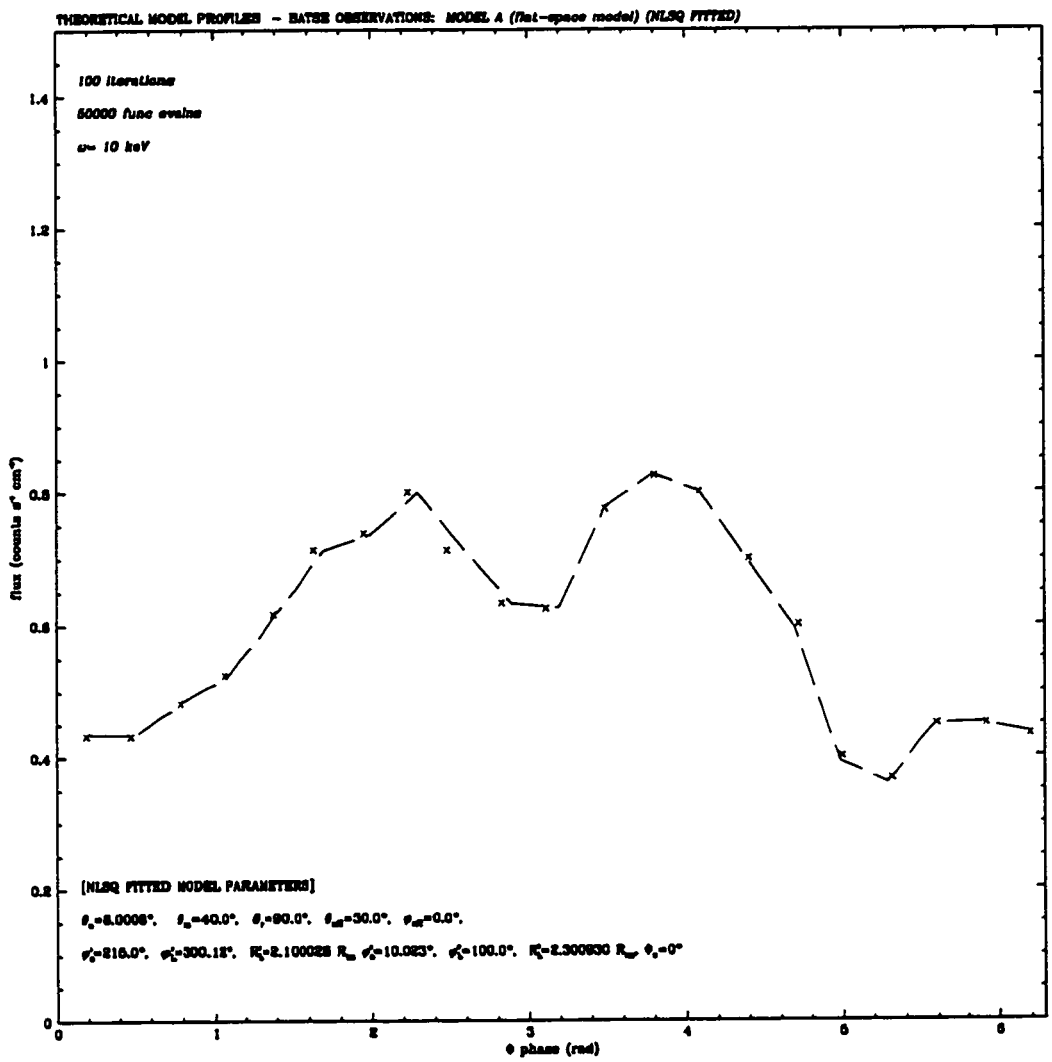

Figure 4.19: Results of NLSQ fitting of BATSE observation [range 3], $L = 7.91{\cdot}10^{35}$ ergs/s pulse profile, for $E_{obs} = 10$ keV.

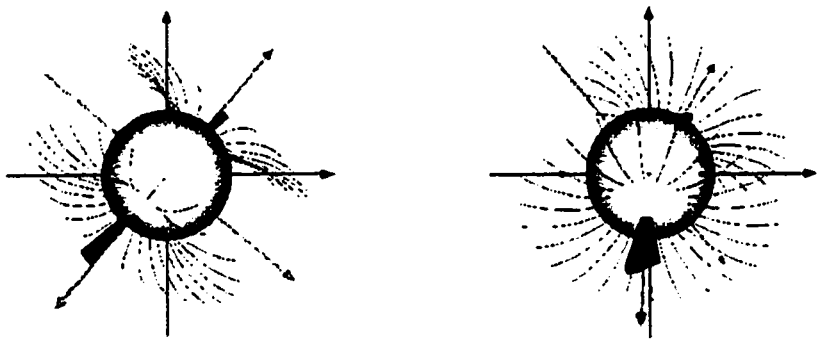

Figure 4.20: VRML visualization for best-fit parameters of BATSE pulse profile for $L = 7.91{\cdot}10^{35}$ ergs/s, for $E_{obs} = 10$ keV, Φ=(0, 45)

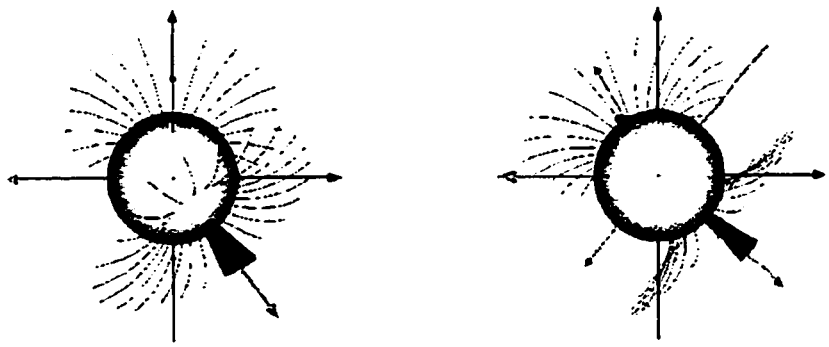

Figure 4.21: Φ=(90, 135)

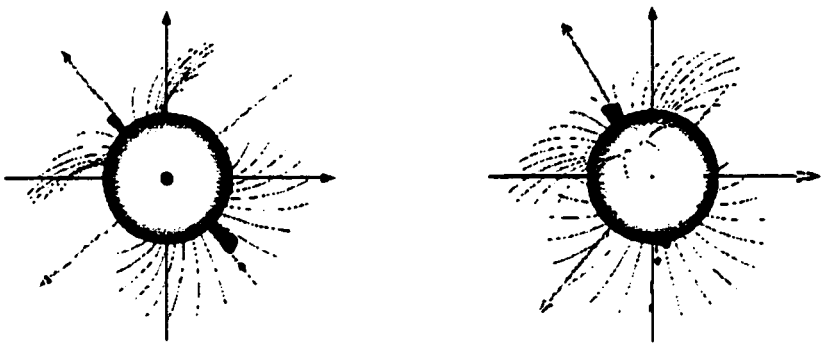

Figure 4.22: Φ=(180, 225)

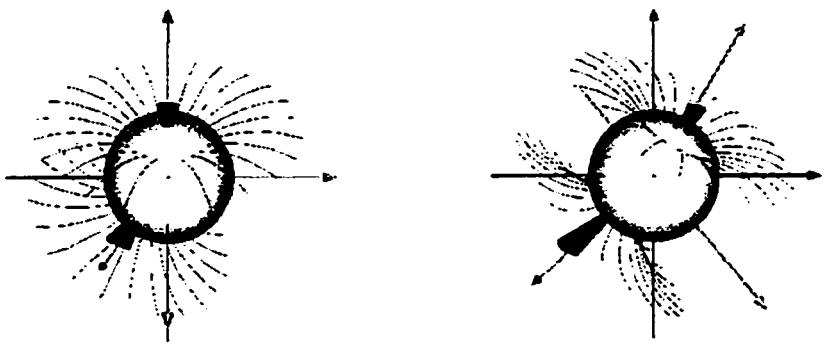

Figure 4.23: Φ=(270, 315)

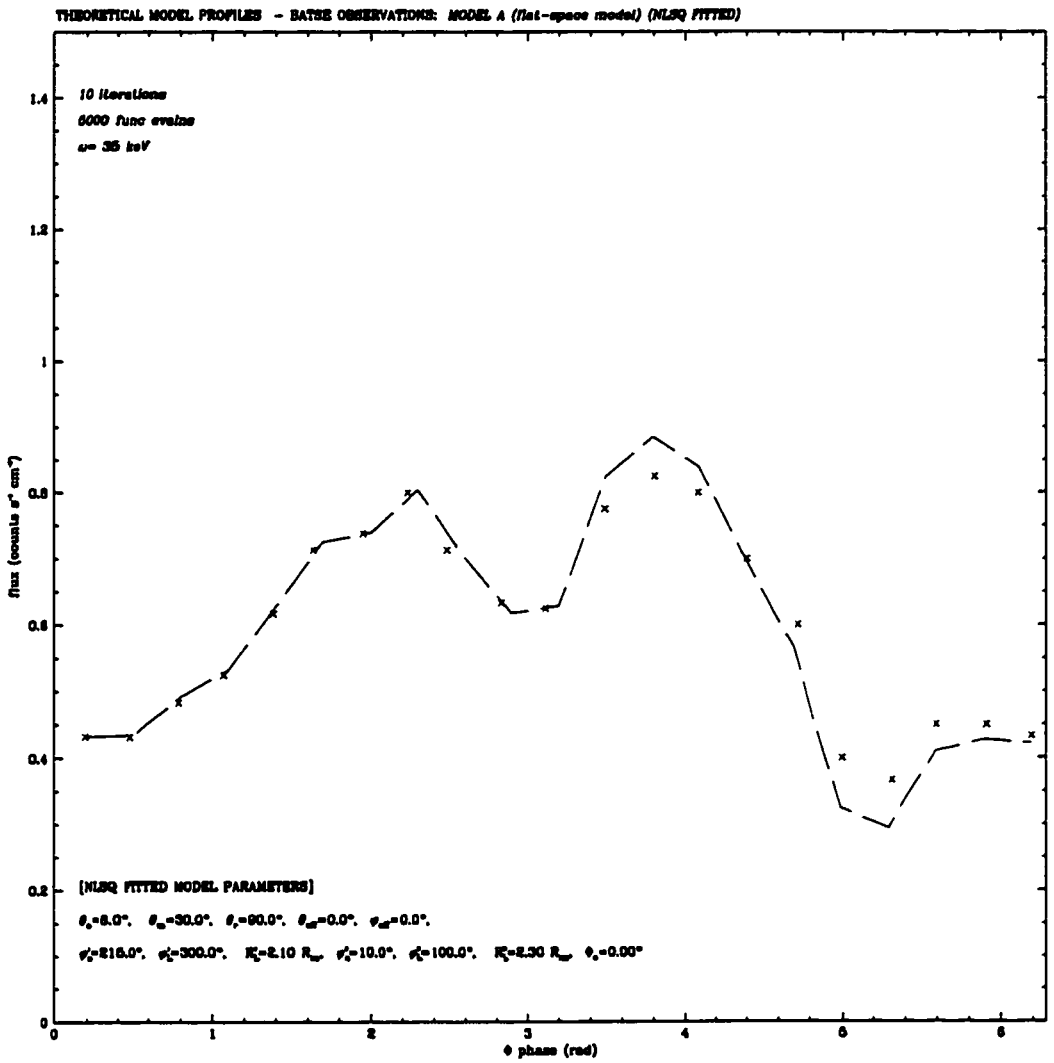

Figure 4.24: Results of NLSQ fitting of BATSE observation [range 3], $L = 7.91 \cdot 10^{35}$ ergs/s pulse profile, for $E_{obs} = 35$ keV.

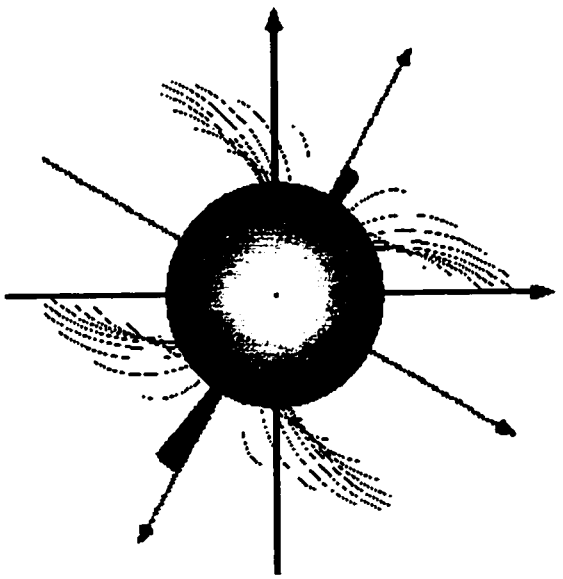

Figure 4.25: VRML visualization for best-fit parameters of BATSE pulse profile for $L = 7.91 \cdot 10^{35}$ ergs/s, for $E_{obs} = 35$ keV.

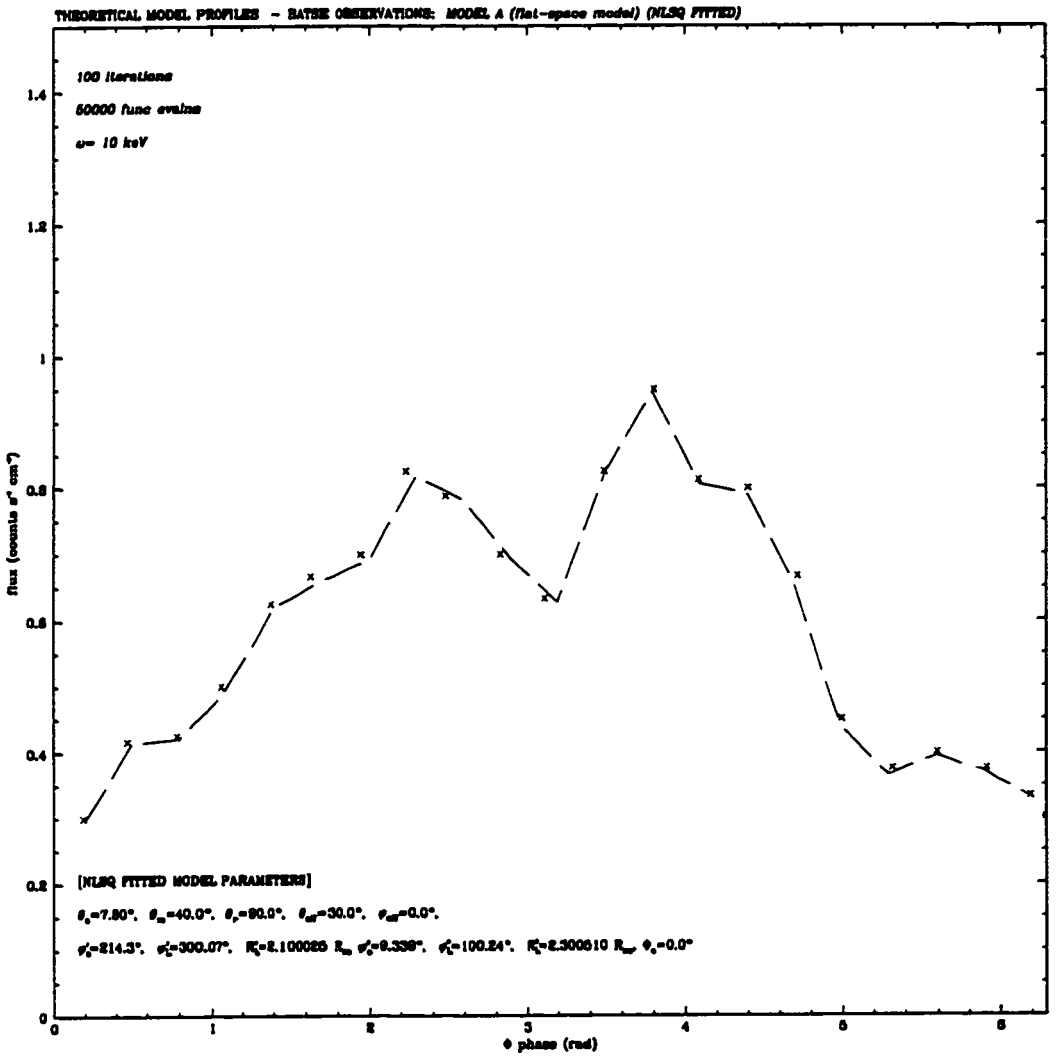

Figure 4.26: Results of NLSQ fitting of BATSE observation [range 4], $L = 1.03 \cdot 10^{36}$ ergs/s pulse profile, for $E_{obs} = 10$ keV.

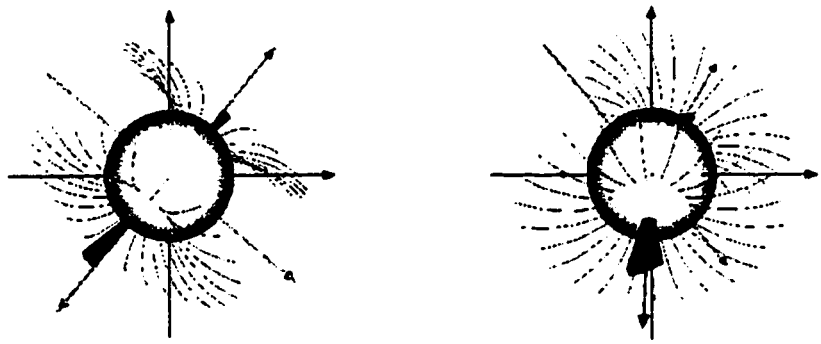

Figure 4.27: VRML visualization for best-fit parameters of BATSE pulse profile for $L = 1.03{\cdot}10^{36}$ ergs/s, for $E_{obs} = 10$ keV, where Φ=(0, 45)

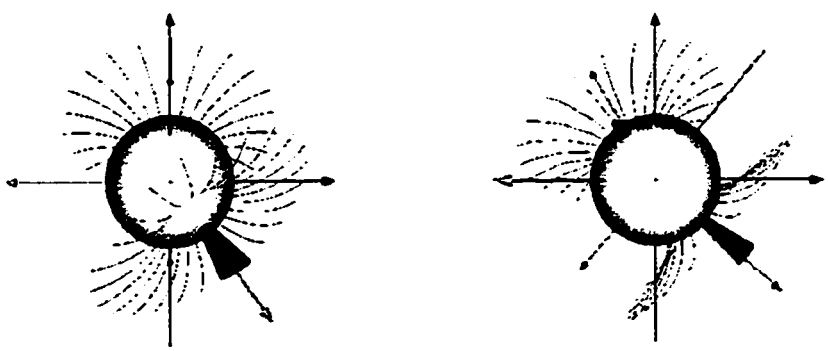

Figure 4.28: Φ=(90, 135)

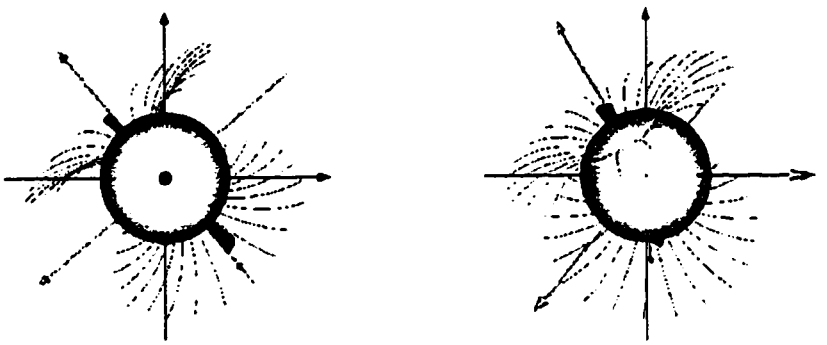

Figure 4.29: Φ=(180, 225)

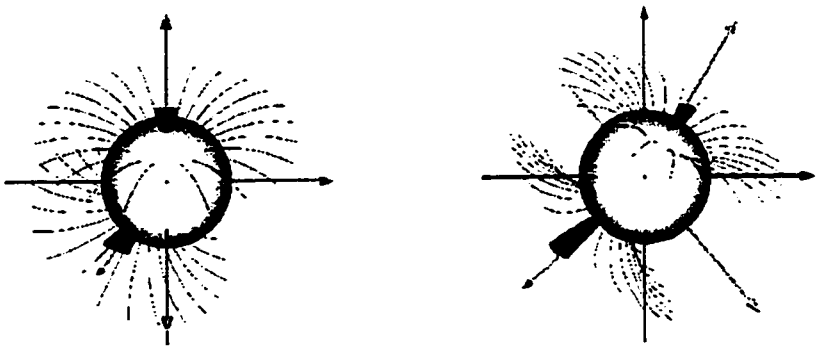

Figure 4.30: Φ=(270, 315)

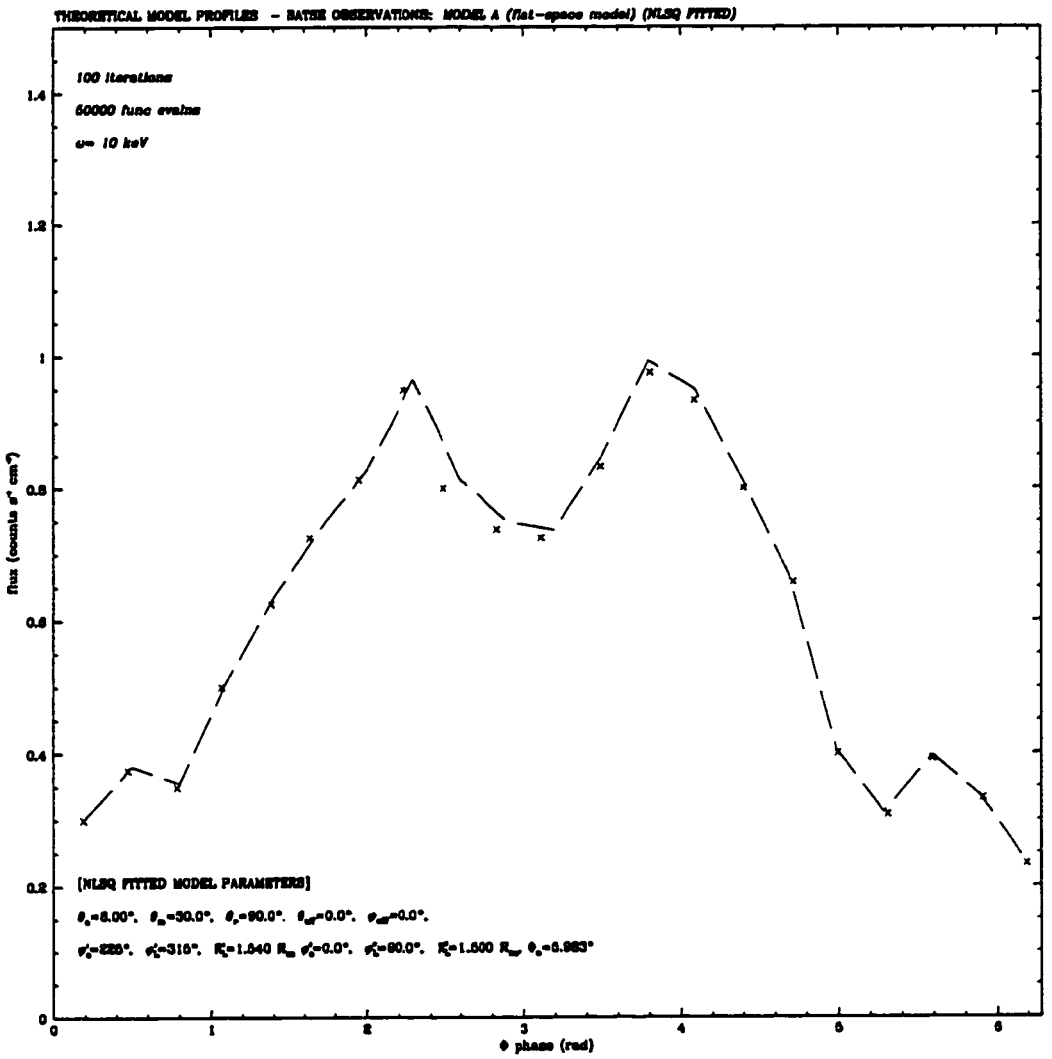

Figure 4.31: Results of NLSQ fitting of BATSE observation [range 5], $L = 1.27{\cdot}10^{36}$ ergs/s pulse profile, for $E_{obs} = 10$ keV.

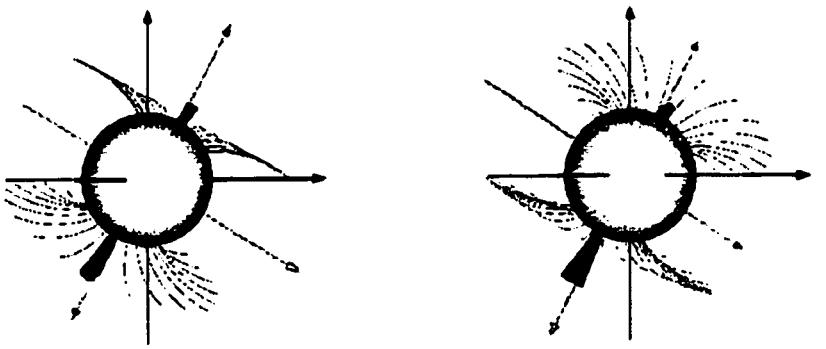

Figure 4.32: VRML visualization for best-fit parameters of BATSE pulse profile for $L = 1.27{\cdot}10^{36}$ ergs/s, for $E_{obs} = 10keV$, where Φ=(0, 45)

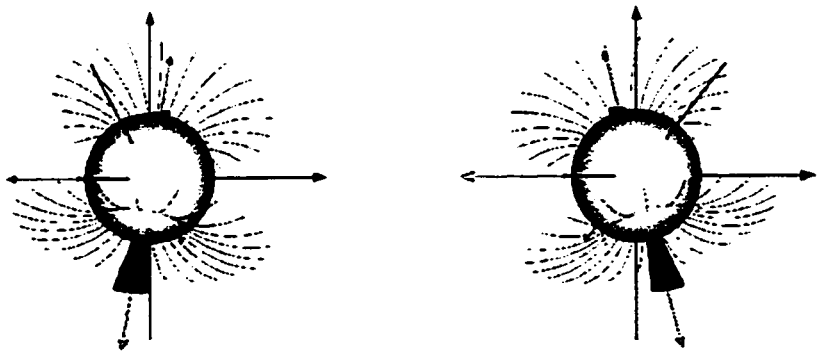

Figure 4.33: Φ=(90, 135)

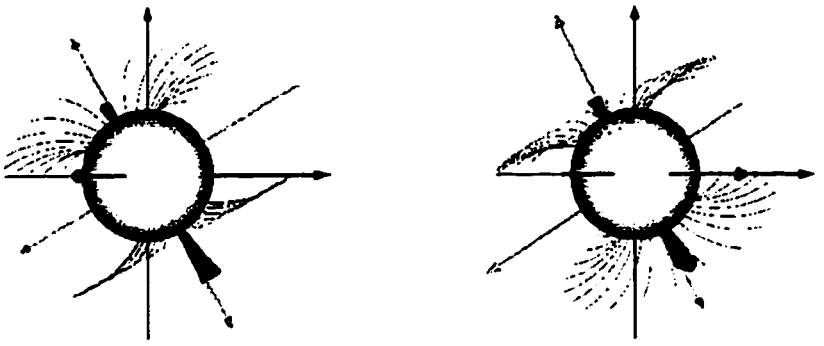

Figure 4.34: Φ=(180, 225)

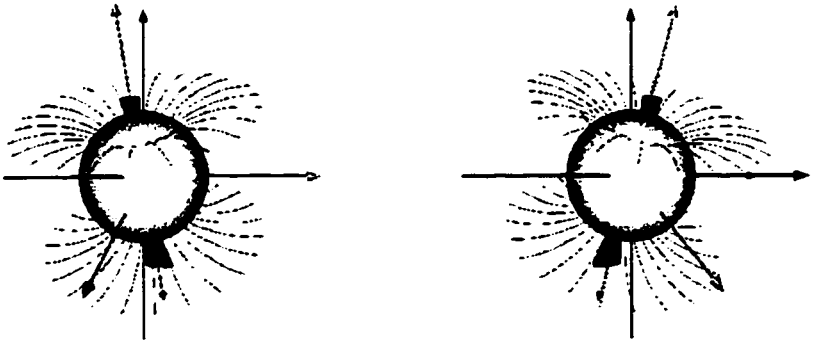

Figure 4.35: Φ=(270, 315)

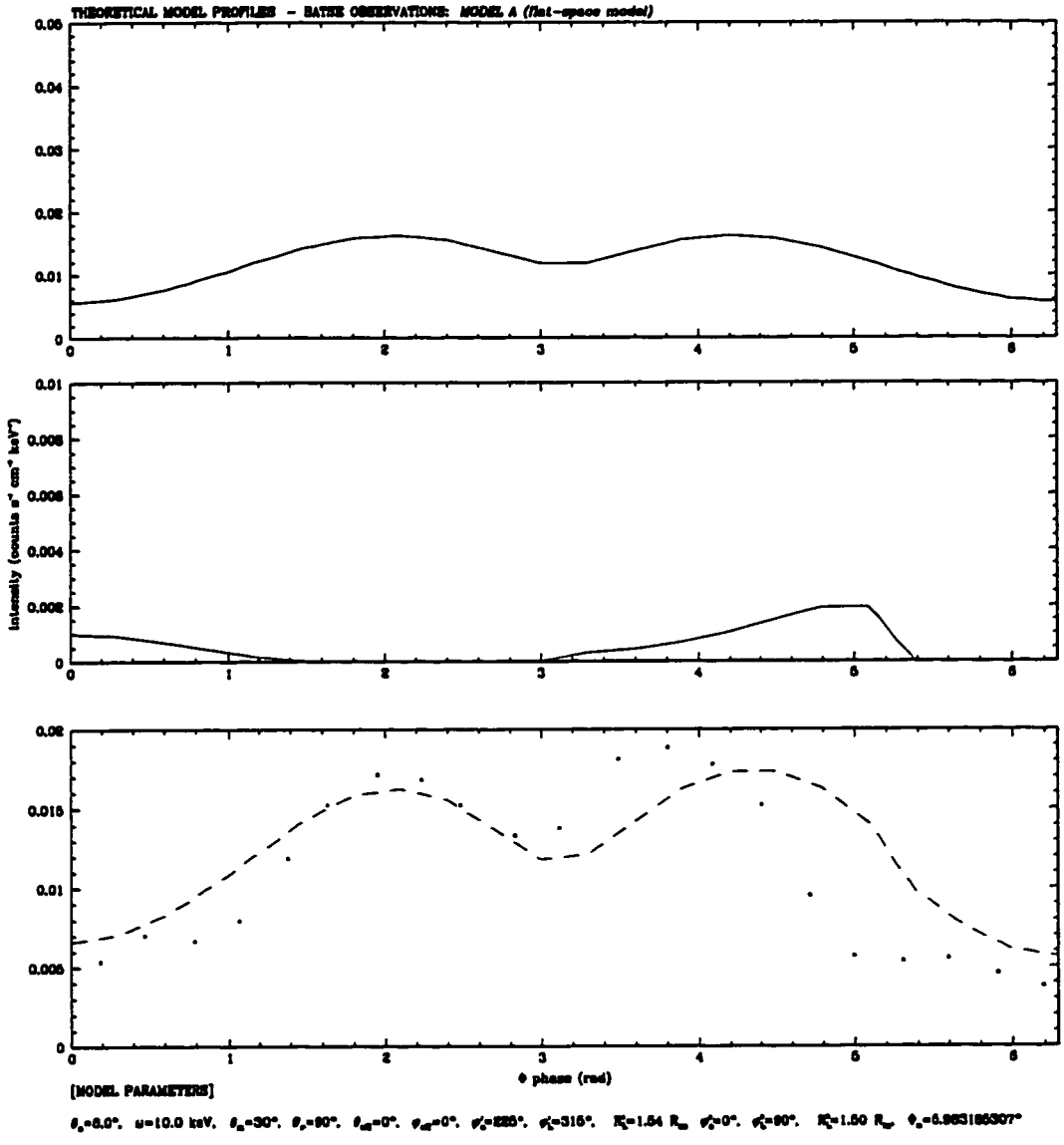

Figure 4.36: Theoretical model curve for BATSE observation [range 6], $L = 1.51 \cdot 10^{36}$ ergs/s pulse profile, before NLSQ fitting, $E_{obs} = 10$ keV.

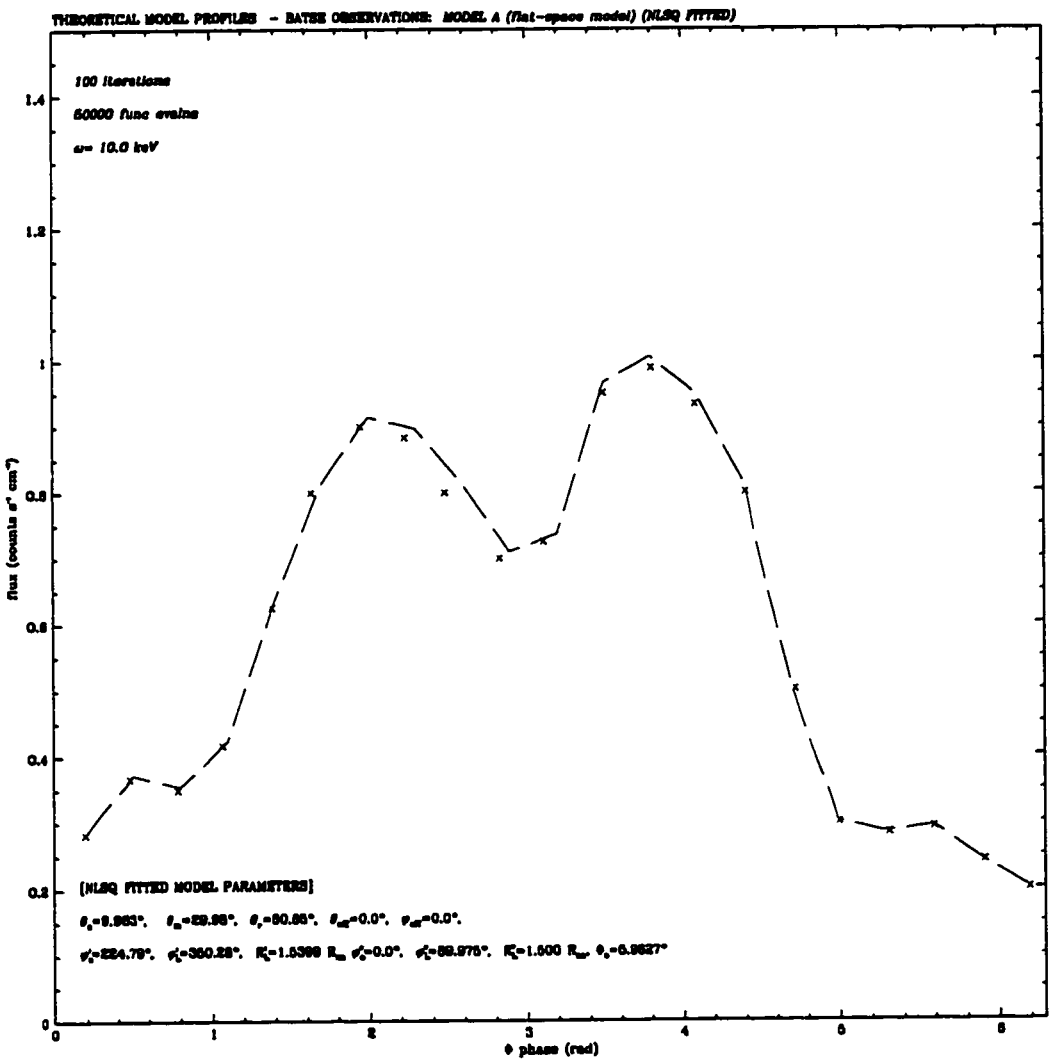

Figure 4.37: Results of NLSQ fitting of BATSE observation [range 6], $L = 1.51 \cdot 10^{36}$ ergs/s pulse profile, for $E_{obs} = 10$ keV.

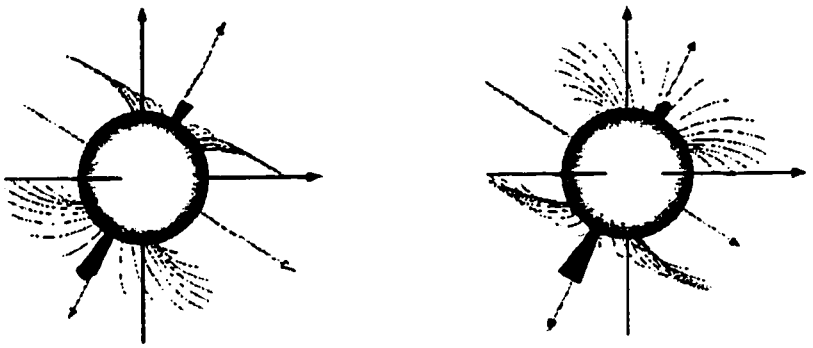

Figure 4.38: VRML visualization for best-fit parameters of BATSE pulse profile for $L = 1.51 \cdot 10^{36}$ ergs/s, for $E_{obs} = 10$ keV, where Φ=(0, 45)

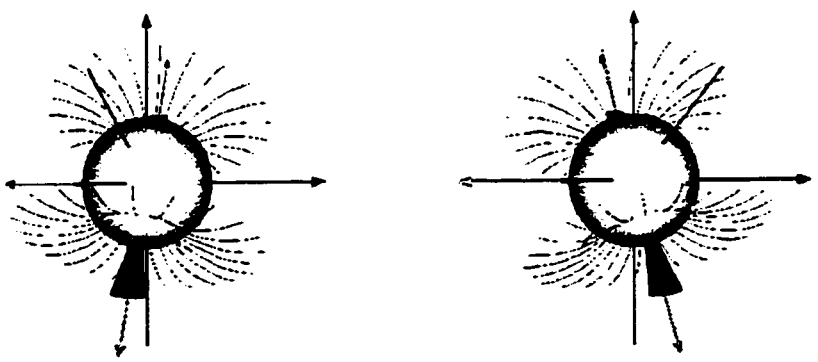

Figure 4.39: Φ=(90, 135)

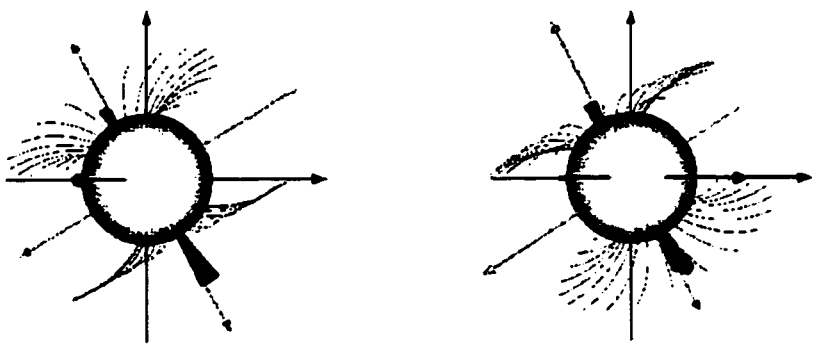

Figure 4.40: Φ=(180, 225)

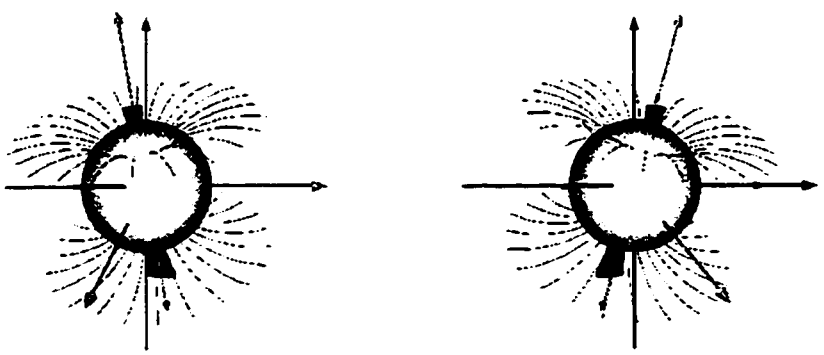

Figure 4.41: Φ=(270, 315)

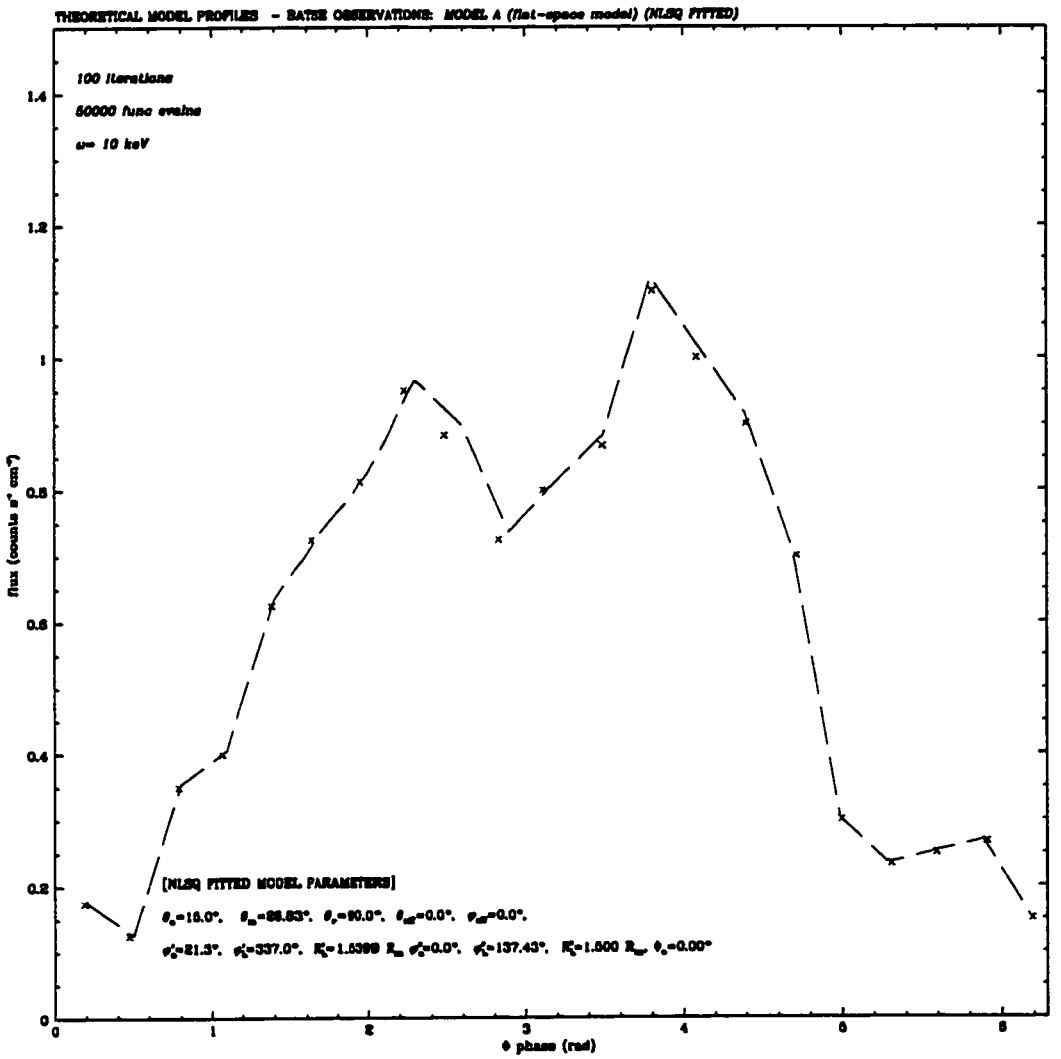

Figure 4.42: Results of NLSQ fitting of BATSE observation [range 6], $L = 1.75{\cdot}10^{36}$ ergs/s pulse profile, for $E_{obs} = 10$ keV.

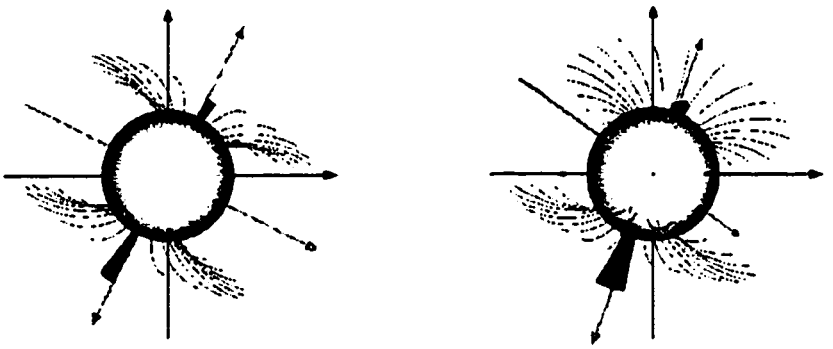

Figure 4.43: VRML visualization for best-fit parameters of BATSE pulse profile for $L = 1.75{\cdot}10^{36}$ ergs/s, for $E_{obs} = 10$ keV,Φ=(0, 45)

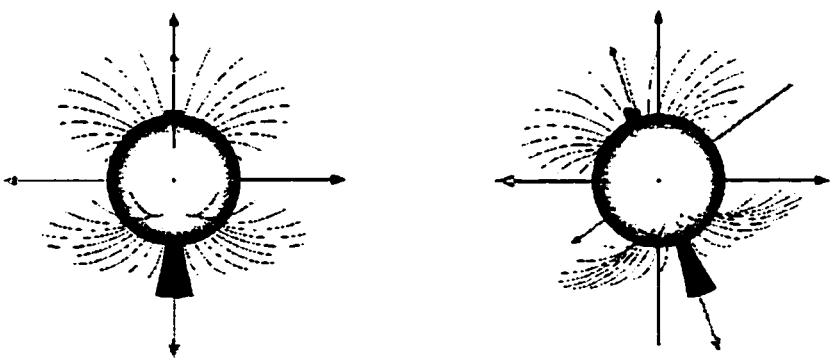

Figure 4.44: Φ=(90, 135)

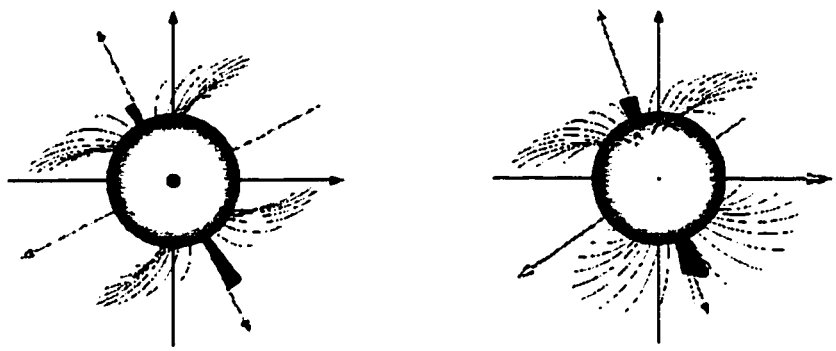

Figure 4.45: Φ=(180, 225)

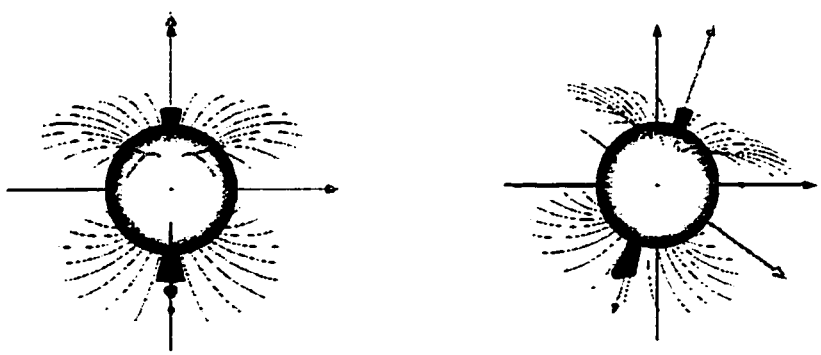

Figure 4.46: Φ=(270, 315)

4.3.1 EXOSAT observations

The EXOSAT observations of EXO 2030+375 are detailed in Parmar *et al.*, (1989)[5][4]. Figures (4.50) - (4.51) show the observed (1-10) keV luminosity-dependent pulse profiles. The variation of the (1-20) keV luminosity with time for the EXOSAT observations is given in Figure (4.47). This figure was produced from luminosity and observation data from Parmar *et al.*, 1989[4], and shows the exponential decrease in the observed luminosities of EXO 2030+375. Phase-averaged cyclotron line energies were obtained by Parmar *et al.*, 1989[5] for each observation and are tabulated in Table 4.48. As the luminosity decreases, the cyclotron line energy increases. This relationship between luminosity and cyclotron line energy may suggest that these cyclotron line energies may be produced by a standoff shock being present in the emission regions of EXO 2030+375, which has a variable height above the neutron star surface. By specifying a surface magnetic field strength, Figure (4.49) shows the radial height for this standoff shock as a function of the observed luminosities. Emission model parameters, tabulated in Table 4.3, were obtained for the May 18, (highest luminosity), and August 13, (lowest luminosity) pulse profiles with E_{obs}=4.5 keV, E_{cyc}=57 keV (see Figures 4.52 and 4.53). Parmar *et al.*, (1989)[4] have previously fit these two profiles using simplified analytic expressions for the local emission intensity in the case of pencil and fan-beam emission. In particular, Parmar *et al.*, have used these analytic equations to fit the May 18 pulse profile, with a component of pencil-beam and fan-beam emission from each emission region. The asymmetric emission model was parameterized in order to reproduce the results of Parmar *et al.* (see Figure 4.54) for the case of two emission regions separated by an angle of 180°.

Table 4.3: Best-fit parameters for the highest and lowest luminosity EXOSAT pulse profiles of EXO 2030+375. $R_L^{(i)}$ values are in units of neutron star radii, and all angles are given in degrees, except Φ_1, which is in radians.

L (ergs/s)	θ_o	θ_m	θ_r	θ_{off}	ϕ_{off}	$\varphi_o^{(1)}$	$\varphi_o^{(2)}$	$\varphi_L^{(1)}$	$\varphi_L^{(2)}$	$\mathbf{R}_L^{(1)}$	$\mathbf{R}_L^{(2)}$	$\mathbf{\Phi}_o$
$1.20 \cdot 10^{36}$	6.0	0.0	90.0	0.0	0.0	180.0	0.0	360.0	180.0	1.30	1.79	1.588
$1.00 \cdot 10^{38}$	13.0	25.0	90.0	0.0	0.0	0.0	30.0	0.0	230.0	0.0	3.00	1.188

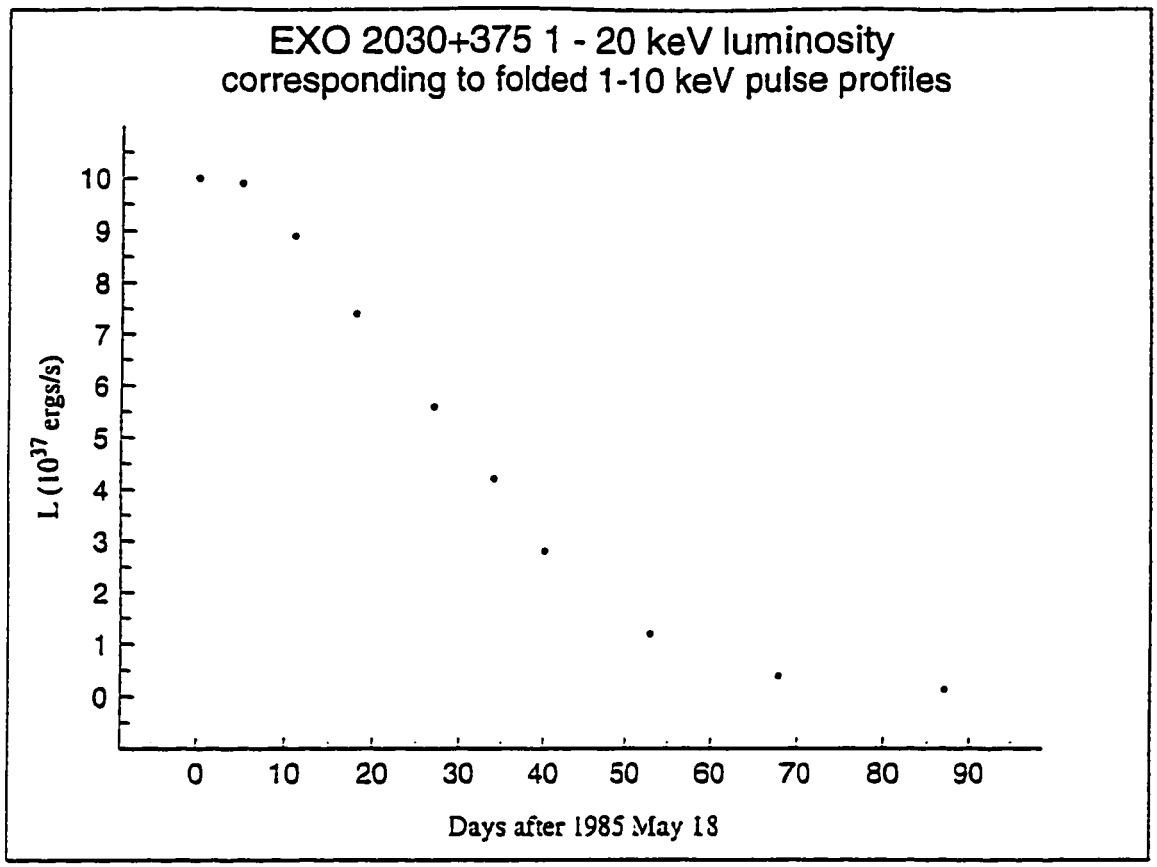

Figure 4.47: Observed luminosity for the sequence of EXOSAT observed pulse profiles, showing an exponential decrease.

PHASE-AVERAGED CYCLOTRON LINE ENERGIES

Luminosity[a] (1-20 keV)	Chi^2 (d.f.=174)	E_0 (keV) (-,+)	E_{cut} (keV) (-,+)	E_0 / E_{cut}
1.0×10^{38}	245	31.9 ± (2.1, 3.1)	19.0 ± 0.6	1.68 ± 0.15
9.9×10^{37}	195	33.0 ± (3.0, 3.0)	19.4 ± 1.1	1.70 ± 0.18
8.9×10^{37}	186	30.7 ± (2.0, 3.7)	18.4 ± 0.6	1.67 ± 0.16
7.4×10^{37}	276	33.5 ± (2.1, 2.5)	19.1 ± 0.4	1.75 ± 0.12
5.6×10^{37}	158	25.0 ± (1.0, 1.0)	13.7 ± (0.3, 0.5)	1.82 ± 0.08
4.2×10^{37}	173	24.5 ± (1.0, 1.0)	12.5 ± 0.6	1.95 ± 0.12
2.3×10^{37}	233	22.0 ± (1.0, 1.0)	11.1 ± (0.5, 0.7)	2.01 ± 0.13
1.2×10^{37}	227	21.0 ± (1.0, 1.0)	9.9 ± 0.4	2.16 ± 0.13
3.9×10^{36}	177	57.0 ± (6.0, 4.0)	9.2 ± (3.5, 1.0)	6.25 ± 1.6

Note - all errors are at the 90% confidence level
[a]For an assumed distance of 5 kpc, in ergs/s

Figure 4.18: Phase-averaged cyclotron-line energies corresponding to the observed pulse profiles.

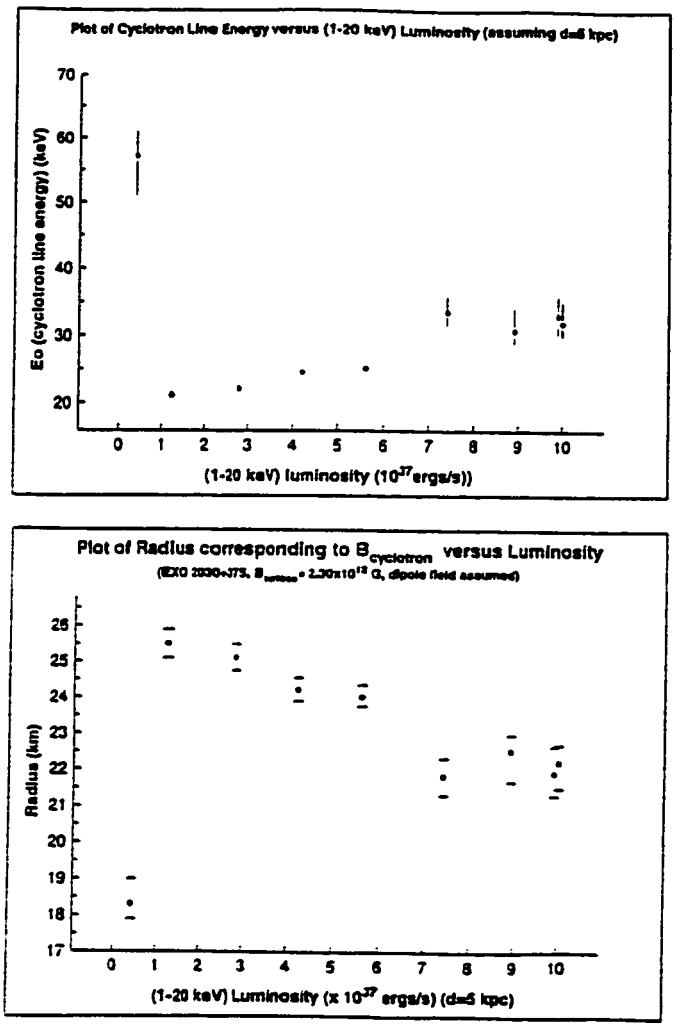

Figure 4.49: The first plot shows the relationship between luminosity and the observed cyclotron-line energy. The second plot shows the radial height at which a shock front is located above the neutron star surface, assuming a surface magnetic field strength of $B_{surface} = 2.30 \cdot 10^{12}$ G, and that the production of the cyclotron-line corresponds to the height of a shock front.

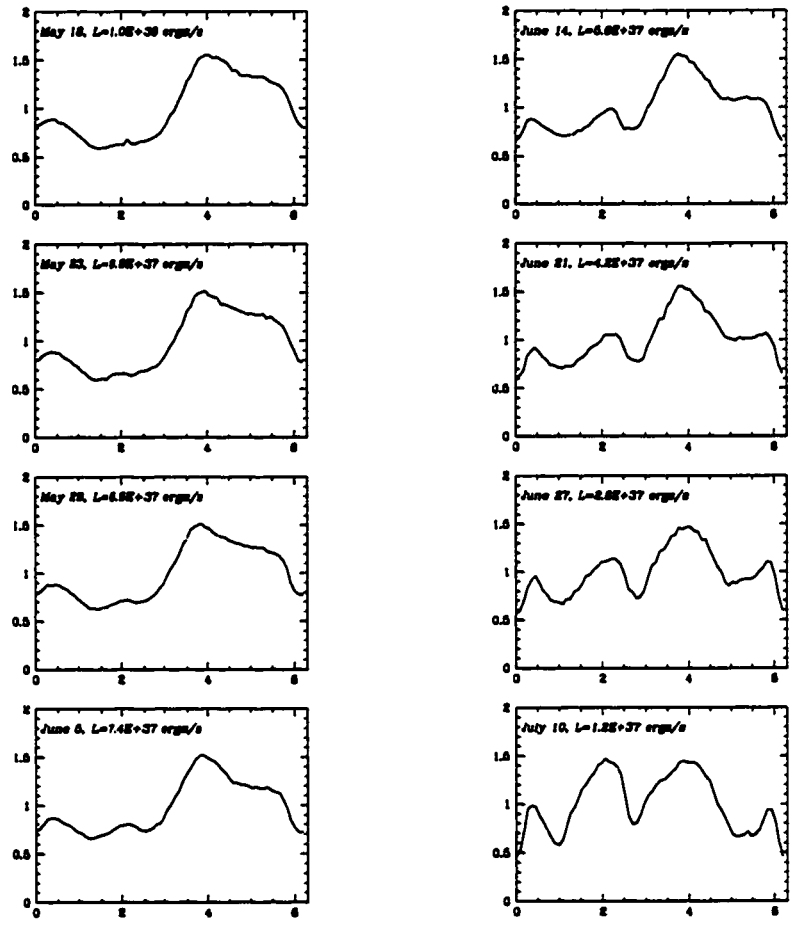

Figure 4.50: $1 - 10$ keV pulse profiles of EX0 $2030 + 375$ with normalized intensity versus phase, for $1 - 20$ keV luminosities (for 5 kpc) given.

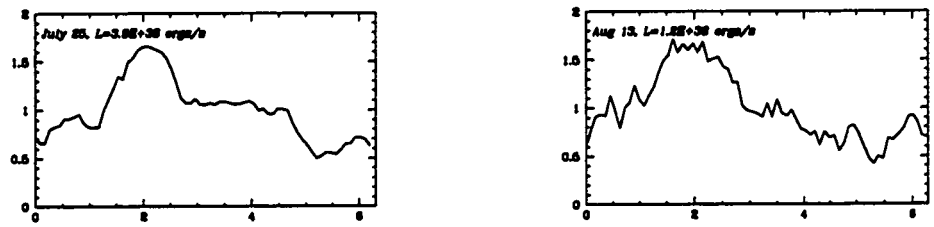

Figure 4.51: $1-10$ keV pulse profiles of EX0 $2030+375$, with normalized intensity versus phase for $1-20$ keV luminosities (for 5 kpc) given.

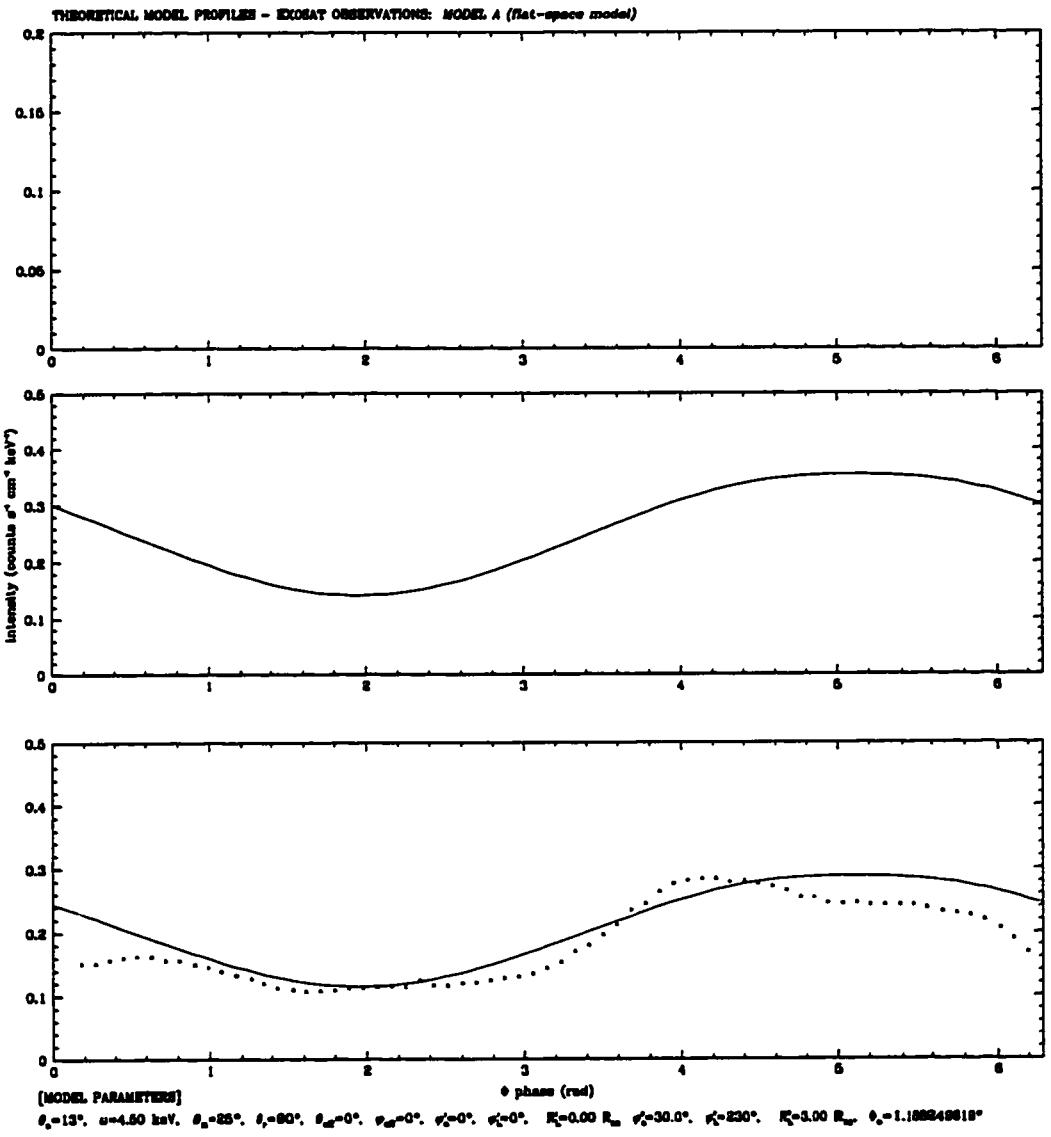

Figure 4.52: Theoretical model curve for highest luminosity EXO 2030 + 375 pulse profile observed on May 18, before NLSQ fitting.

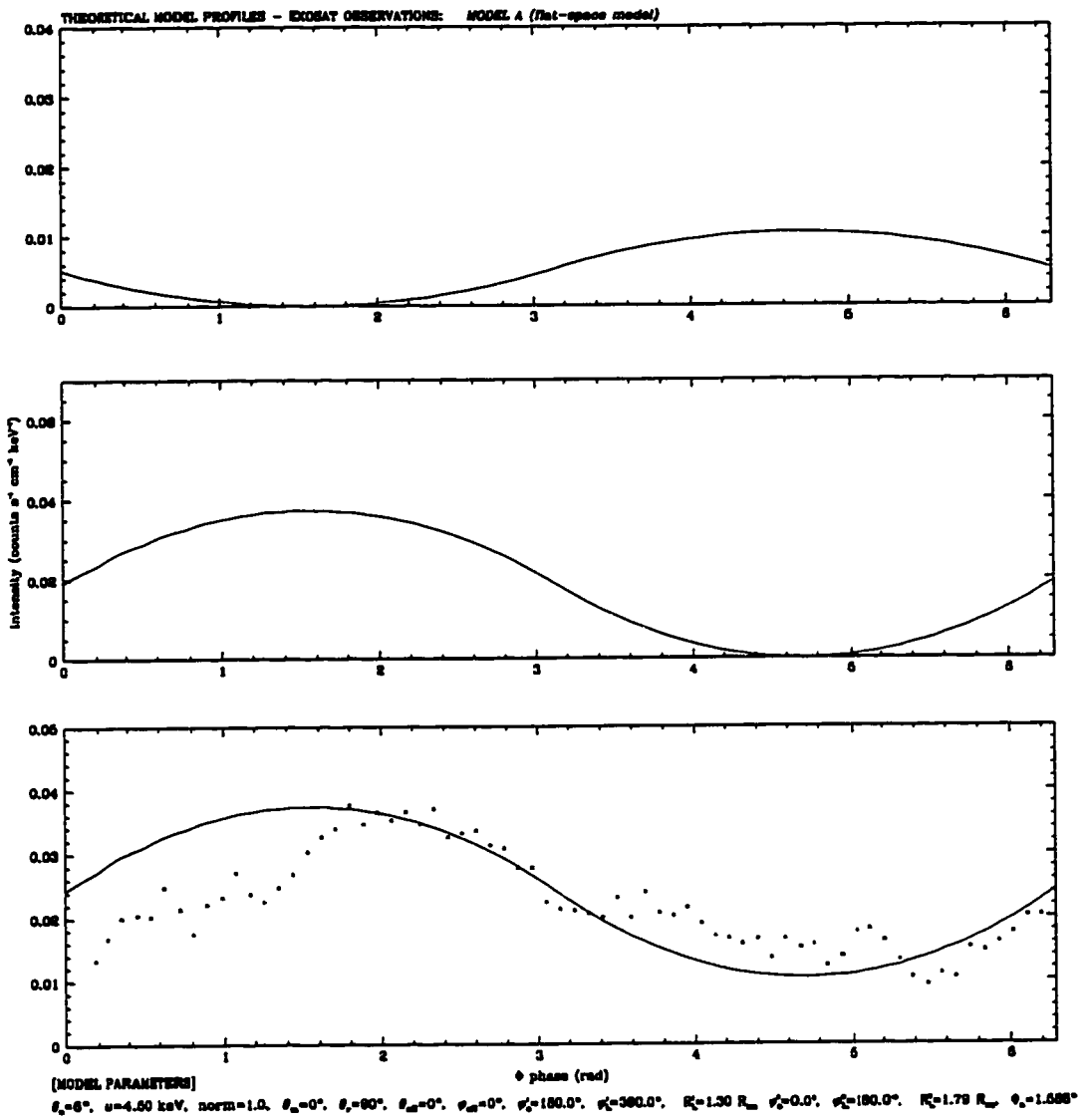

Figure 4.53: Theoretical model curve for lowest luminosity EXO 2030 + 375 pulse profile observed on Aug 13, before NLSQ fitting.

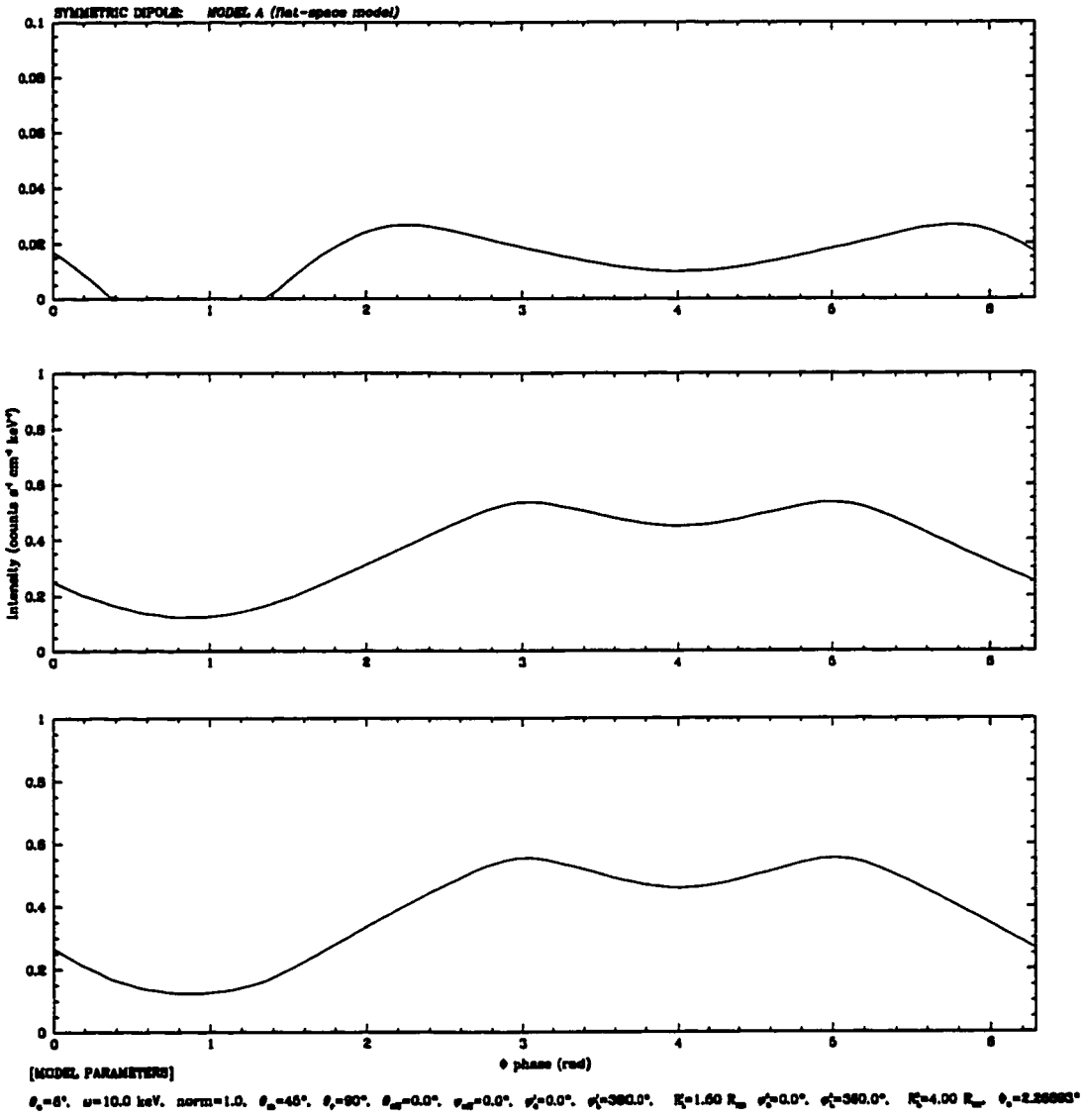

Figure 4.54: Predicted symmetric dipole profile for fan-beam emission for the EXOSAT observation of May 18, 1985. In this figure, the emission model (only fan-beam emission) produces similar intensity profiles to those obtained by Parmar *et al.*, (1989), where both pencil and fan-beam emission is considered.

Figure 4.55: VRML visualization when phase, Φ=(0, 45) for theoretical curve for the EXOSAT pulse profile of May 18. The input parameters of the model (see section 2.2.1) are set to correspond to the geometry of the symmetric dipole model of Parmar *et al.*, (1989).

Figure 4.56: Φ=(90, 135)

Figure 4.57: VRML visualization when phase, Φ=(180, 225) for theoretical curve for the EXOSAT pulse profile of May 18. The input parameters (see section 2.2.1) are set to correspond to the geometry of the symmetric dipole model of Parmar *et al.*, (1989).

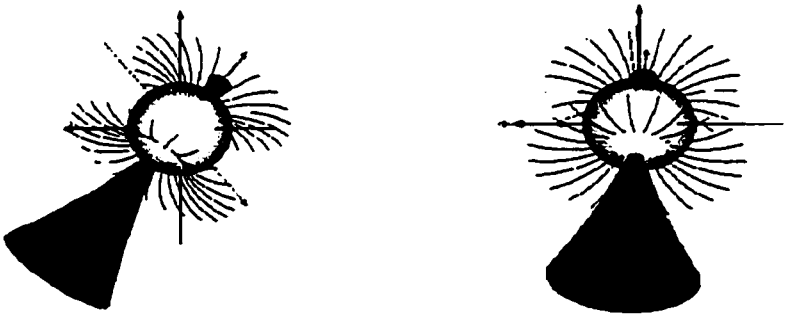

Figure 4.58: Φ=(270, 315)

Chapter 5

Discussion

The best-fit parameters obtained for the BATSE pulse profiles indicate that as the luminosity of EXO 2030+375 increases, the polar-cap angle, θ_o also increases. This same trend is also present in the fitting of the EXOSAT pulse profiles of May 18, and August 13, 1985. This may suggest that in the case of fan-beam emission at high luminosities, matter is accreted onto magnetic field lines which penetrate the accretion disk further within its magnetosphere. The presence of a shock in the emission region of EXO 2030+375 could block photons from travelling upwards, thereby expanding the sides of an emission region, and forcing photons to be emitted parallel to the stellar surface. According to the model of Arons and Lea (1980)[23], based on spherically-symmetric accretion onto a slowly rotating neutron star, the polar-cap angle θ_o is inversely related to luminosity as,

$$\theta_o \sim 0.35 \cdot \left(\frac{10^{37}}{L_x}\right)^{0.28} rad \tag{5.1}$$

For the range of luminosity in the BATSE and EXOSAT observations of EXO 2030+375 of $(4.79 \cdot 10^{33} - 1.0 \cdot 10^{38})$ ergs s^{-1}, equation 5.1 gives $\theta_o = (170.0 - 10.5)°$. The value for $\theta_o = 10.5°$ for a luminosity of $1.0 \cdot 10^{38}$ ergs s^{-1} is close to the value of 13.0° obtained in the asymmetric emission model of this thesis (Table 4.3). In fitting pulse profiles of x-ray pulsars using analytic flux distributions, radiating emission areas corresponding to cones of angular width at least as wide as $\theta_o \sim 20° - 30°$ are needed to raise the background level to the order of the observed flux (Wang

and Welter, 1981)[54]. Fitted values of θ_o calculated from this asymmetric emission model lie within a range $\theta_o \sim 6° - 15°$ (see Tables 4.1- 4.3) giving partial support to the results of Wang and Welter, (1981)[54] having $\theta_o \sim 20° - 30°$

The inverse relationship of luminosity and the value of θ_o in equation 5.1 is in contrast to a direct relationship found by the fan-beam emission model of this thesis. Whether the magnitude of variation in θ_o with luminosity should be expected to be large is an important point of interest. According to this model, the magnitude of the variation of θ_o seems reasonable, when used to estimate the strength of the magnetic field close to the neutron star surface with the equation for the magnetic field lines. As illustrated by Figure (5.1), a neutron star which has an inclination angle, α, with respect to its accretion disk could lead to θ_o values which are larger than non-inclined models due to the pulling of the magnetic field lines by the disk. The polar-cap angle θ_o is labelled in this diagram as β. An estimate of the accretion radii for θ_o opening angles between $6° - 15°$ is calculated as $r_a = R_x/sin^2\theta_o \sim (100R_x - 15R_x)$ (Arons and Lea (1980)[23]), respectively. R_x is the radius of the neutron star. Comparison of this radial estimate with the accretion radius of $(6 - 20)\cdot 10^4 km$ for a disk calculated in equation 1.16 shows that this estimate exceeds the accretion radius for a stellar wind of $7\cdot 10^4 km$ from equation 1.15, thereby supporting a model of an accretion disk surrounding the neutron star in EXO 2030+375.

The angle to the observer, θ_r remained fixed at 90° from the rotation axis for all of the pulse profile fits, excluding the BATSE profile at $L = 1.51\cdot 10^{36}$ ergs s^{-1}, which required θ_r to vary by 10°. The magnetic axis angle, θ_m, determined for EXO 2030+375 averages to 29.4°. The existence of this inclination angle is supported by the pulse profile fitting of Wang and Welter, (1981) who show that in 8 out of a total

of 14 x-ray binaries considered, the dipole axis appeared to be tilted with respect to the rotation axis with values on the order of $\theta_m \sim 30°$. The value of $\theta_m \sim 30°$ in the pulse profile fitting therefore seems reasonable, and is fairly consistent between profiles varying within a range of $\sim 10°$.

The radial height of the emission regions between the BATSE and EXOSAT profiles were shown to increase with luminosity. At low luminosities the height of each emission region was approximately constant and showed slight deviations with changing luminosity. Vasyliunas, (1979)[47] provides an estimate of the height of a neutron star emission region as,

$$r = R_x \sqrt{\left(\frac{R_x}{R_{cf}}\right)} \tag{5.2}$$

where R_x and R_{cf} are the radius of the neutron star, and Chapman-Ferraro radius. For neutron stars, $R_{cf} \sim 300R_x$ (Vasyliunas, 1979)[47], and this leads to a radial height estimate of $0.058R_x$ km or 1.058 R_x if defined from the neutron star's centre of mass. The fitted values of the radial heights in Tables 4.1 - 4.3 for the observed pulse profiles are consistent with this estimate. Figure (5.2) shows a curve for shock height, measured above the stellar surface, as a function of the accretion rate at fixed values of the surface magnetic field strength (units of 10^{12} G)(Langer and Rappaport, 1982)[44]. For a magnetic field strength of $3.3{\cdot}10^{13}G$ the height of a standoff shock in the emission region of a neutron star varies up to a value close to $1.5R_{ns}$, where R_{ns} is the radius of the neutron star. A comparison of these calculations with the results of the emission model of this thesis suggests that a shock is present in the atmosphere of the neutron star in EXO 2030+375, and that it may define the height of the emission regions.

For low luminosities, the emission regions are shown in this thesis to be partially-filled. As luminosity increases, best-fit values for the azimuthal angles $\varphi_o^{(i)}$, $\varphi_L^{(i)}$ indicate that the emission regions are filled with matter. The EXOSAT pulse profile observed on August 13 was modelled with ~equal, partially-filled emission sections close to φ =180° apart. The predicted symmetric profile for May 18 was fit using pencil-beam and fan-beam emission from two poles by Parmar *et al.*, (1985). The parameters of the asymmetric emission model of this thesis were chosen so as to form similar emission region geometry as the symmetric dipole model of Parmar *et al.*, (1985). Figure (4.54) shows that the emission model can reproduce the profile of Parmar without pencil-beam emission. In addition, this may indicate that fan-beam emission is dominant in the May 18 observed profile.

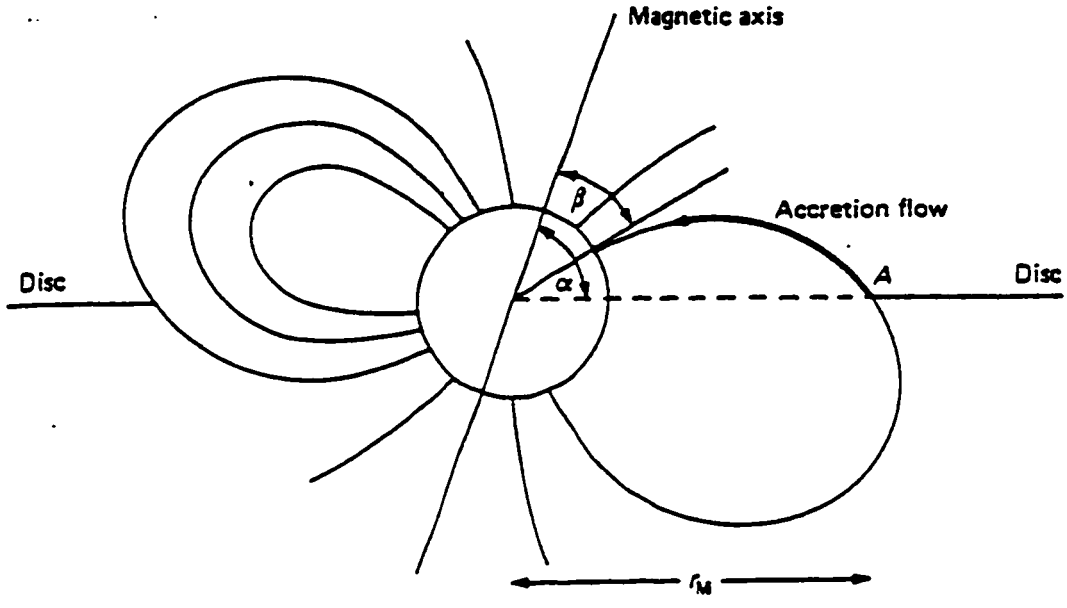

Figure 5.1: The standard model of a magnetized neutron star. with an inclined magnetic axis. taken from Henrichs, (1983).

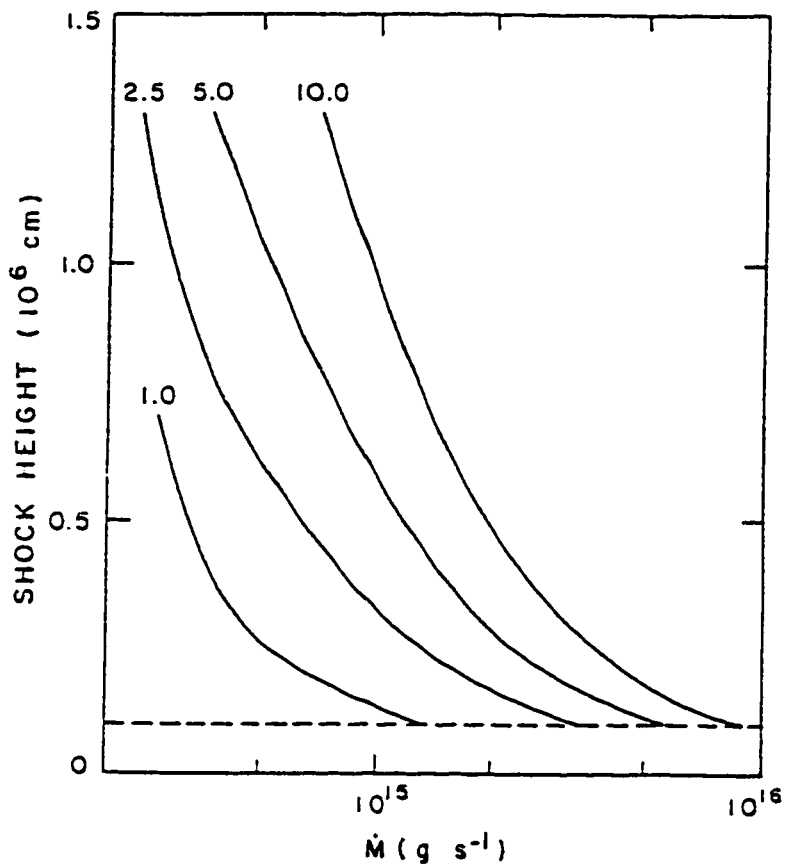

Figure 5.2: Shock height versus accretion rate at fixed values of the surface magnetic field in factors of 10^{12} Gauss. The polar cap area is 10^{10} cm^2. Accretion rates that force the shock below the dashed line result in pressure effects that lead to unrealistic flow solutions as calculated by Langer and Rappaport, (1982).

Chapter 6

Conclusions

The theoretical pulse profiles produced by variation of the parameters in this asymmetric emission model are able to reproduce the major features of the observed pulse profiles of EXO 2030+375. The pulse profile fitting indicates that for varying luminosity, the emission regions of the neutron star in this binary system are asymmetric or partially-filled. Since this model defines the sides of the emission regions to follow the magnetic field geometry near the poles, the asymmetric filling of matter may be the result of a difference of angular velocity between the neutron star and the surrounding plasma. This would cause matter to channel along magnetic field lines which lead towards the leading or trailing side of the magnetic poles. The best-fit model parameters obtained for the BATSE and EXOSAT observations imply two emission regions of ~equal height lying along a magnetic axis that is tilted by $(20 - 40)^\circ$ from the rotation axis of the neutron star. The results of this model also suggest the presence of a stand-off shock lying above the neutron star surface, with a height that varies with the luminosity.

This model provides a new description of emission geometry in accreting neutron stars. By incorporating the recent results of magnetic radiative-transfer calculations, this model establishes a vital connection between observations of neutron stars (pulse profiles) and the understanding of the interaction processes taking place within their atmospheres. Results of the theoretical model for *flat* space are consistent with other simple analytic fan-beam emission models considered in the literature.

Chapter 7

Future Research

Future research goals are summarized as follows,

- A primary extension to the *flat* space model is the requirement of an accretion disk surrounding the neutron star. A simple thin disk model can be used to add the consideration of shadowing effects of the emission regions by a disk in the neutron star's equatorial plane.

- Implementation of the model for *curved* space with the effect of gravitational-light bending. It is expected that this model will sharpen the peaks of the fan-beam emission. Fitting of this model to the full sequence of the EXOSAT observations of EXO 2030+375 can then be performed.

- In order to reproduce unequal peaks or double-peak structures in the pulse profiles of many accreting x-ray pulsars, the asymmetry of this model can be extended to the case of unequal radial heights on either side of the magnetic axis in each emission region.

- The full theoretical *curved* space model can be applied to a study of the luminosity dependence in pulse profiles of other High-mass x-ray binaries. This would establish whether this model presents a unified description of the emission regions of accreting x-ray pulsars. Such a study may indicate the requirement of pencil-beam emission from the top of the emission regions.

Bibliography

[1] Illarionov A.F., Sunyaev, R.A. *Astron. Ap.*, 39:185–, 1975.

[2] Norton A.J., Chakrabarty D., Coe M.J., Everall C., Finger M.H., Prince T.A., Roche P., Stollberg M.T., Wilson R.B. *Mon. Not. R. Astron. Soc.*, 271:981–992, 1994.

[3] Harding A.K., Meszaros P., Kirk J.G., Galloway D.J. *ApJ.*, 278:369–381, 1984.

[4] Parmar A.N., White N.E., Stella L. *ApJ.*, 338:373–380, 1989.

[5] Parmar A.N., White N.E., Stella L., Izzo C., Ferri P. *ApJ.*, 338:359–372, 1989.

[6] G. Borner. *X-rays From Neutron Stars.* North-Holland Publishing Company, 1980.

[7] Leahy D.A. *Mon. Not. R. Astron. Soc.*, 242:188–193, 1990.

[8] Leahy D.A. *Mon. Not. R. Astron. Soc.*, 251:203–212, 1991.

[9] Leahy D.A., Li L. *Mon. Not. R. Astron. Soc.*, 277:1177–1184, 1995.

[10] Janot-Pacheco E., Motch C., Pakull M.W. *Astron. Astrophys.*, 202:81–82, 1988.

[11] Lamb F.K., Fabian, A.C., Pringle, J.E. *ApJ.*, 217:197–212, 1977.

[12] Fritz G., Henry, R. Meekins, J. Chubb, T. Friedman, H. *Science*, 164:709–712, 1969.

[13] Morfill G.E., Trümper, J. Bodenheimer, P. Tenorio-Tagle, G. *Astron. Astrophys.*, 139:7–14, 1984.

[14] Pavlov G.G., Shibanov Y.A., Silant'ev N.A., Nagel W. *ApJ.*, 291:170–177, 1985.

[15] Chen H., Marlborough, J.M. Waters, L.B.F.M. *ApJ.*, 384:605–612, 1992.

[16] Friedman H., Lichtman, S. Bryam, E. *Phys. Rev.*, 83:1025–1030, 1951.

[17] Riffert H. *ApJ.*, 310:728–732, 1986.

[18] Riffert H., Meszaros P. *ApJ.*, 325:207–217, 1988.

[19] Henrichs H.F. *Accretion Driven Stellar X-ray Sources.* Cambridge University Press, Cambridge, 1983.

[20] Bradt H.V.D., Ohashi T., Pounds K.A. *Ann. Rev. Astron. Astrophys.*, 30:391–427, 1992.

[21] Iben I., Tutukov A.V., Yungelson L.R. *Astron. Astrophys. Suppl. Ser.*, 100:217–231, 1995.

[22] Wassermann I., Shapiro S.L. *ApJ.*, 265:1036–1046, 1983.

[23] Arons J., Lea S.M. *ApJ.*, 235:1016–, 1980.

[24] Trümper J., Lewin W.H.G., Brinkmann W., editor. *The Evolution of Galactic X-Ray Binaries.* D. Reidel Publ. Co., Holland, 1986.

[25] Ventura J., Pines D. *Neutron Stars: Theory and Observation.* Kluwer Academic Publ., 1991.

[26] Petterson J.A. *Phys. Rev. D.*, 10:3166–3170, 1974.

[27] Davidson K., Ostriker J.P. *ApJ.*, 179:585–598, 1973.

[28] Waters L.B.F.M., Taylor A.R., van den Heuvel E.P.J., Habets G.M.H.J., Persi P. *Astron. Astrophys.*, 198:200–210, 1988.

[29] L. Li. Modeling observed x-ray pulsar profiles. Master's thesis, University of Calgary, 1995.

[30] Brainerd M.M., Meszaros P. *ApJ.*, 369:179–190, 1991.

[31] Stollberg M.T., Paciesas, W.S., Finger, M.H., Scott, D.M., Wilson, R.B., Fishman, G.J., Wilson, C.A. *Bull. American Astron. Soc.*, 185:102–109, 1994.

[32] Ghosh P., Lamb F.K. *ApJ.*, 232:259–279, 1979.

[33] Ghosh P., Lamb F.K. *ApJ.*, 234:296–316, 1979.

[34] Meszaros P. *Space. Sci. Rev.*, 38:325–351, 1984.

[35] Meszaros P. *High-Energy Radiation from Magnetized Neutron Stars.* University of Chicago Press, Chicago, 1992.

[36] Meszaros P., Nagel W. *ApJ.*, 298:147–160, 1985.

[37] Meszaros P., Nagel W. *ApJ.*, 299:138–153, 1985.

[38] Giacconi R., Gursky, H. Paolini, F. Rossi, B. *Phys. Rev. Lett.*, 9:439–443, 1962.

[39] Giacconi R., Kellogg, E. Gorenstein, P. Gursky, H. Tananbaum, H. *Ap. J. Lett.*, 165:L27–35, 1971.

[40] Elsner R.F., Lamb F.K. *ApJ.*, 215:897–913, 1977.

[41] Wald R.M. *General Relativity.* University of Chicago Press, Chicago, 1984.

[42] Bowyer S., Byram, E. Chubb, T. Friedman, H. *Science*, 146:912–917, 1964.

[43] Rappaport S., Joss P.C. *X-ray Astronomy with the Einstein Satellite.* Reidel, Dordrecht, 1981.

[44] Langer S.H., Rappaport S. *ApJ.*, 257:733–751, 1982.

[45] Shapiro S.L., Teukolosky S.A. *Black Holes, White Dwarfs and Neutron Stars: The Physics of Compact Objects.* John Wiley and Sons, Inc., 1983.

[46] Ohashi T., Inoue H., Kawai N., Koyama K., Matsuoka M., Mitani K., Tanaka Y. *Publ. Astron. Soc. Japan.*, 36:719–729, 1984.

[47] V.M. Vasyliunas. *Space. Sci. Rev.*, 24:609–634, 1979.

[48] Forman W., Jones, C. Cominsky, L. Julien, P. Murray, S. *Ap. J. Suppl.*, 38:357–412, 1978.

[49] Nagel W. *ApJ.*, 251:278–287, 1981.

[50] Nagel W. *ApJ.*, 251:288–296, 1981.

[51] Li X., Wang Z. *Astrophys. Space. Sci.*, 234:39–48, 1995.

[52] Zel'dovich Y.B., Shakura N.I. *Sov. Astron.*, 13:175–183, 1969.

[53] Wang Y.M., Frank M.H. *Astron. Astrophys.*, 93:255–268, 1981.

[54] Wang Y.M., Welter G.L. *Astron. Astrophys.*, pages 97–109, 1981.

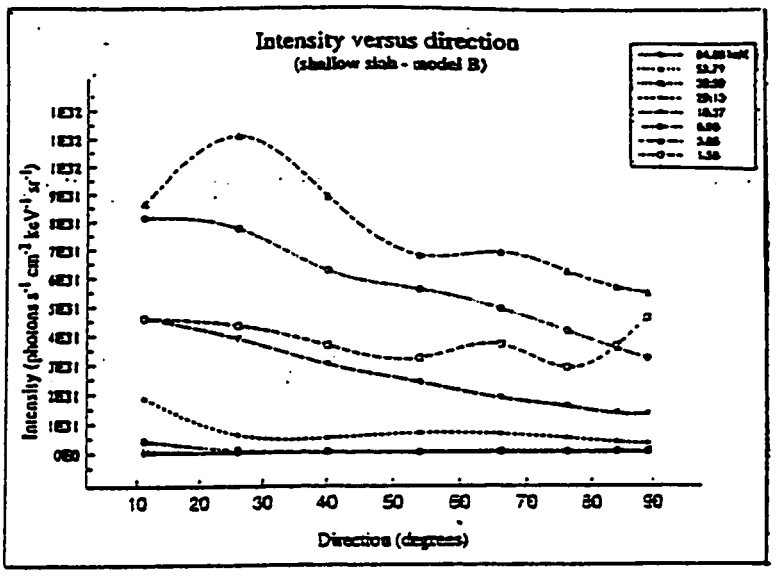

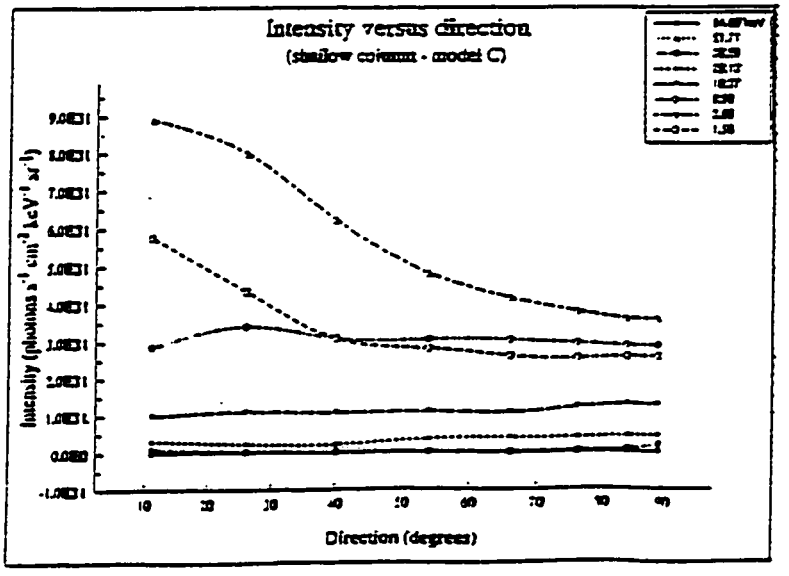

Figure .1: Plots of intensity versus direction of emission from slab (model B) and column (model C), optically-thin emission elements from the numerical calculations of Meszaros.

Values of Icos(Θ) for Shallow Slab - Model B

Energy (keV)	Direction Angle (degrees)							
	11.0	26.0	40.0	54.0	66.0	76.0	84.0	89.0
84.66	8.5×10^{28}	6.5×10^{28}	5.8×10^{28}	2.5×10^{28}	2.5×10^{28}	1.3×10^{28}	3.9×10^{27}	6.0×10^{26}
51.71	1.0×10^{29}	2.6×10^{29}	1.9×10^{29}	2.9×10^{29}	3.9×10^{29}	1.9×10^{29}	6.0×10^{28}	8.0×10^{27}
28.59	4.0×10^{29}	8.0×10^{29}	3.8×10^{29}	2.0×10^{29}	1.4×10^{29}	9.0×10^{28}	6.9×10^{28}	1.2×10^{28}
29.13	1.8×10^{31}	5.5×10^{30}	3.9×10^{30}	4.0×10^{30}	2.6×10^{30}	1.2×10^{30}	3.8×10^{29}	5.3×10^{28}
18.37	4.5×10^{31}	3.5×10^{31}	2.3×10^{31}	1.4×10^{31}	7.5×10^{30}	3.8×10^{30}	1.4×10^{30}	2.3×10^{29}
8.98	8.0×10^{31}	7.0×10^{31}	4.8×10^{31}	3.3×10^{31}	2.0×10^{31}	1.0×10^{31}	3.7×10^{30}	5.5×10^{29}
3.85	8.5×10^{31}	1.0×10^{32}	6.8×10^{31}	4.0×10^{31}	2.3×10^{31}	1.5×10^{31}	5.9×10^{30}	9.5×10^{29}
1.58	4.5×10^{31}	3.9×10^{31}	2.8×10^{31}	1.9×10^{31}	1.5×10^{31}	7.0×10^{30}	3.8×10^{30}	8.0×10^{29}

Table .1: Values of Icos(θ) for the shallow-slab, model B.

Values of Isin(Θ) for Shallow Column - Model C

Energy (keV)	Direction Angle (degrees)							
	11.0	26.0	40.0	54.0	66.0	76.0	84.0	89.0
84.66	3.9×10^{27}	1.2×10^{28}	2.0×10^{28}	3.0×10^{28}	3.8×10^{28}	4.0×10^{28}	4.4×10^{28}	4.4×10^{28}
51.71	4.4×10^{28}	4.9×10^{28}	8.8×10^{28}	2.3×10^{29}	6.0×10^{29}	7.4×10^{29}	8.0×10^{29}	8.3×10^{29}
38.59	1.8×10^{29}	1.5×10^{29}	1.5×10^{29}	1.7×10^{29}	2.0×10^{29}	3.4×10^{29}	8.0×10^{29}	1.9×10^{30}
29.13	6.0×10^{29}	9.8×10^{29}	1.5×10^{30}	3.0×10^{30}	3.8×10^{30}	4.0×10^{30}	4.4×10^{30}	4.5×10^{30}
18.37	1.9×10^{30}	4.8×10^{30}	7.0×10^{30}	9.0×10^{30}	1.0×10^{31}	1.2×10^{31}	1.3×10^{31}	1.3×10^{31}
8.98	5.5×10^{30}	1.5×10^{31}	2.0×10^{31}	2.5×10^{31}	2.8×10^{31}	2.9×10^{31}	2.9×10^{31}	2.9×10^{31}
3.85	1.7×10^{31}	3.5×10^{31}	4.0×10^{31}	3.9×10^{31}	3.8×10^{31}	3.7×10^{31}	3.6×10^{31}	3.6×10^{31}
1.58	1.1×10^{31}	1.9×10^{31}	2.0×10^{31}	2.3×10^{31}	2.4×10^{31}	2.5×10^{31}	2.6×10^{31}	2.5×10^{31}

Table .2: Values of Isin(θ) for the shallow-column, model C.

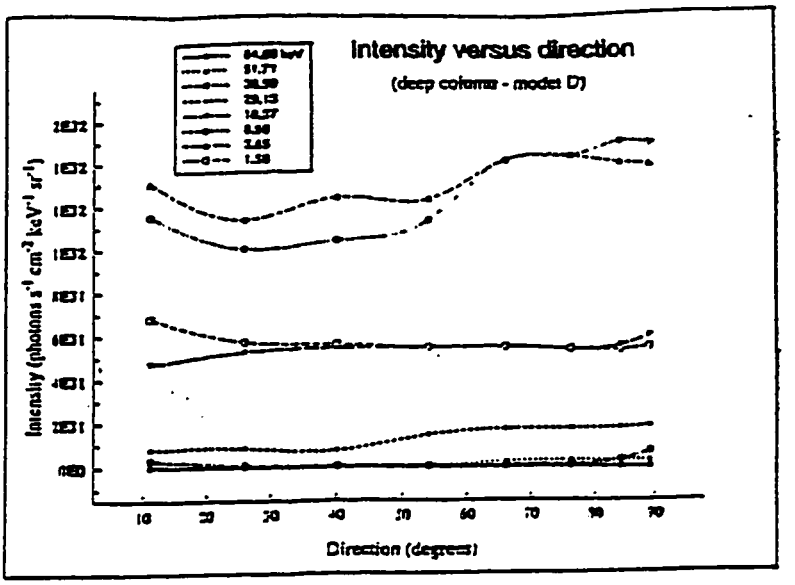

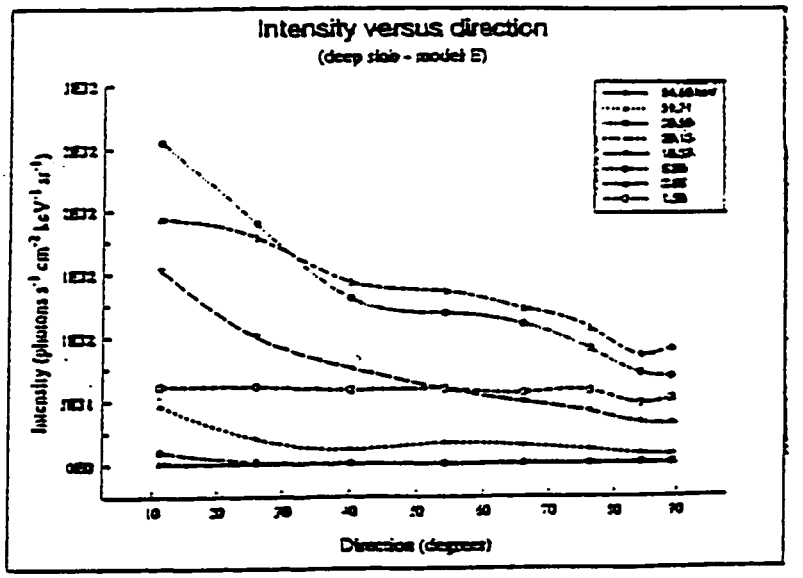

Figure .2: Plots of intensity versus direction of emission from slab (model E) and column (model D), optically-thick emission elements from the numerical calculations of Meszaros.

Values of Icos(Θ) for Deep Slap - Model E

Energy (keV)	Direction Angle (degrees)							
	11.0	26.0	40.0	54.0	66.0	76.0	84.0	89.0
84.66	2.3×10^{-20}	1.8×10^{-20}	1.5×10^{-20}	9.5×10^{-21}	5.0×10^{-21}	2.8×10^{-21}	9.0×10^{-22}	1.6×10^{-22}
51.71	2.3×10^{-20}	5.9×10^{-20}	4.3×10^{-20}	6.0×10^{-20}	8.5×10^{-20}	4.5×10^{-20}	1.6×10^{-20}	1.8×10^{-21}
38.59	9.5×10^{-20}	1.8×10^{-20}	7.8×10^{-20}	4.5×10^{-20}	3.0×10^{-20}	2.0×10^{-20}	1.6×10^{-20}	2.5×10^{-20}
29.13	4.5×10^{-21}	1.8×10^{-21}	9.0×10^{-20}	1.0×10^{-21}	6.0×10^{-20}	2.8×10^{-20}	8.5×10^{-20}	1.3×10^{-20}
18.37	1.5×10^{-22}	9.0×10^{-21}	5.8×10^{-21}	3.5×10^{-21}	2.0×10^{-21}	1.0×10^{-21}	3.4×10^{-20}	5.5×10^{-20}
8.98	2.5×10^{-22}	1.7×10^{-22}	1.0×10^{-22}	7.0×10^{-21}	4.5×10^{-21}	2.2×10^{-21}	7.5×10^{-20}	1.2×10^{-20}
3.85	1.9×10^{-22}	1.6×10^{-22}	1.1×10^{-22}	8.0×10^{-21}	5.0×10^{-21}	2.5×10^{-21}	9.0×10^{-20}	1.5×10^{-20}
1.58	6.0×10^{-21}	5.5×10^{-21}	4.5×10^{-21}	3.5×10^{-21}	2.3×10^{-21}	1.4×10^{-21}	5.0×10^{-20}	9.0×10^{-20}

Table .3: Values of Icos(θ) for the deep-slab, model E.

Values of Isin(Θ) for Deep Column - Model D

Energy (keV)	Direction Angle (degrees)							
	11.0	26.0	40.0	54.0	66.0	76.0	84.0	89.0
84.66	1.8×10^{28}	4.4×10^{28}	8.0×10^{28}	1.3×10^{29}	1.6×10^{29}	1.8×10^{29}	1.9×10^{29}	1.9×10^{29}
51.71	1.8×10^{29}	1.8×10^{29}	2.8×10^{29}	7.9×10^{29}	2.3×10^{30}	2.9×10^{30}	3.2×10^{30}	3.4×10^{30}
38.59	5.8×10^{29}	4.9×10^{29}	4.8×10^{29}	5.3×10^{29}	6.5×10^{29}	1.2×10^{30}	3.2×10^{30}	7.0×10^{30}
29.13	1.5×10^{30}	3.8×10^{30}	5.0×10^{30}	1.2×10^{31}	1.6×10^{31}	1.7×10^{31}	1.8×10^{31}	1.9×10^{31}
18.37	9.0×10^{30}	2.3×10^{31}	3.5×10^{31}	4.4×10^{31}	5.0×10^{31}	5.2×10^{31}	5.5×10^{31}	5.0×10^{31}
8.98	2.2×10^{31}	4.4×10^{31}	6.7×10^{31}	9.2×10^{31}	1.3×10^{32}	1.4×10^{32}	1.5×10^{32}	1.5×10^{32}
3.85	2.5×10^{31}	5.0×10^{31}	8.0×10^{31}	1.0×10^{32}	1.3×10^{32}	1.4×10^{32}	1.4×10^{32}	1.4×10^{32}
1.58	1.3×10^{31}	2.5×10^{31}	3.6×10^{31}	4.4×10^{31}	5.0×10^{31}	5.2×10^{31}	5.3×10^{31}	5.5×10^{31}

Table .4: Values of Isin(θ) for the deep-column, model D.

IMAGE EVALUATION
TEST TARGET (QA-3)

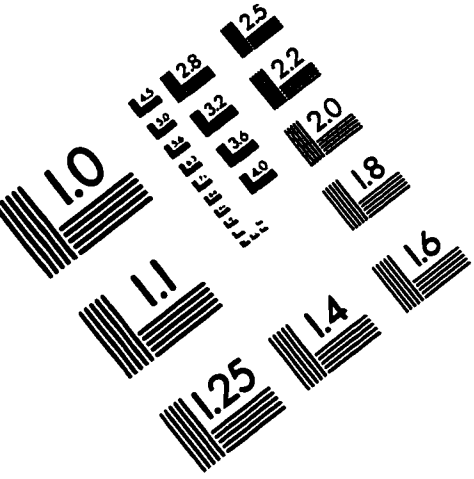

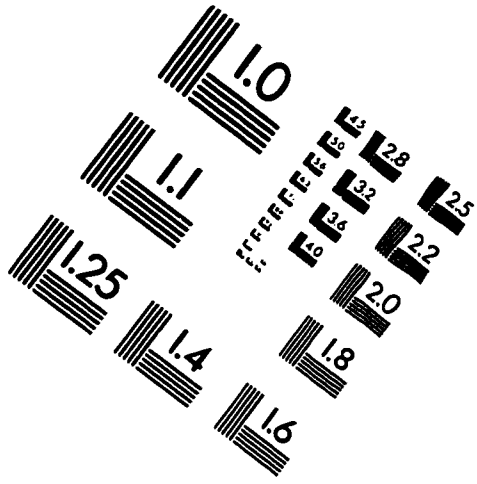

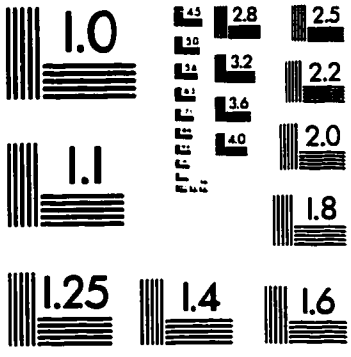

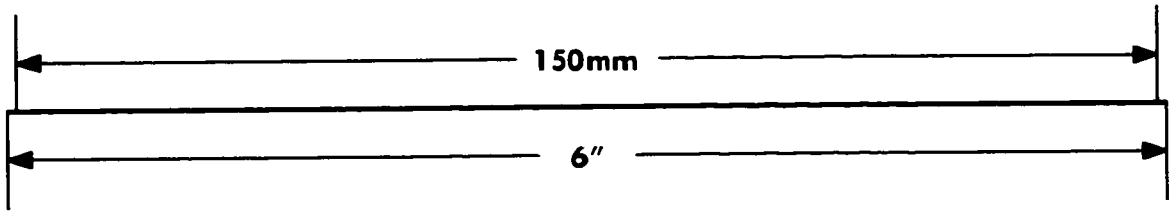

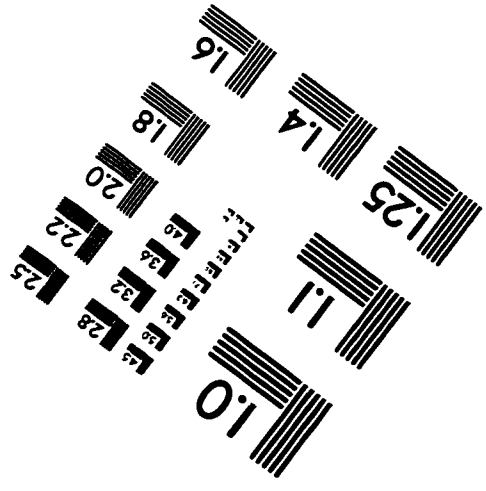

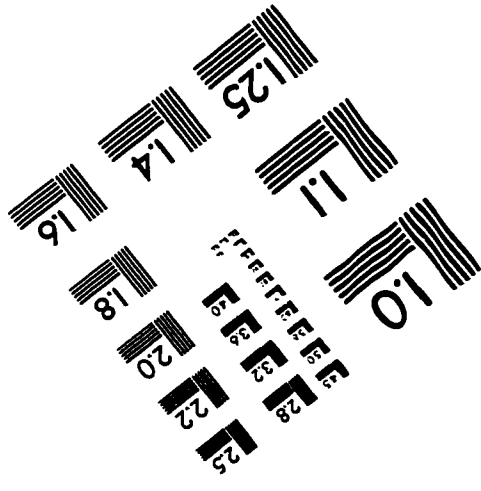

APPLIED IMAGE, Inc
1653 East Main Street
Rochester, NY 14609 USA
Phone: 716/482-0300
Fax: 716/288-5989